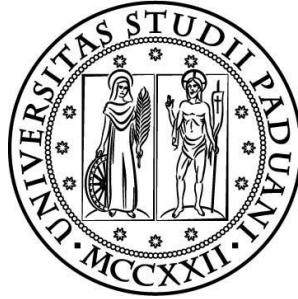Università degli Studi di Padova

Faculty of Physics

Propagation of electromagnetic waves in "Fishnet" metamaterials

Doctoral Thesis

Dr. Giuseppe Parisi

Padua, 2012

Coordinator: Ch.mo Prof. Andrea Vitturi
Supervisor: Ch.mo Prof. Filippo Romanato

To my father

Summary

Abstract

Propagation of electromagnetic waves in "Fishnet" metamaterials

Recently, the fabrication and optimization of nano-hole arrays in noble metal layers have attracted much attention both because of the interesting new physics associated with them and for their potential applications in nano-optics and biosensing. In particular nano-hole arrays in metal-dielectric-metal stacks, also known as "fish-net" type structures, are nowadays the best candidates to accomplish some suggestive physical phenomena like negative refractive index. The doctoral thesis summarizes the study of the propagation of electromagnetic waves in periodic structures, namely in *Fishnet* metamaterials. The EM propagation enables an uncommon property: the negative refraction index. The general aim of the thesis is to study the origin of the negative refraction index and its dependence on the geometric parameters, initially dealing with the basic three-layers fishnet until studying more evolved structures such as a multilayered fishnet structure. Some methods and effective models for the extraction of the complex parameters will be initially considered in the preliminary study. However for a more rigorous investigation, a recent modal method for the analysis of bulk strongly coupled structures (i.e. multilayered fishnet) ,in which also the evanescent modes linked to the metal losses can play a crucial role , will be presented. The *FEM* method is based on the Elmholts's equation in weak form and it represents a powerful method for the investigation of complex modes, responsible for the negative refraction index, from a more fundamental point of view.

Sommario

***Propagazione delle onde elettromagnetiche attraverso i metamateriali
"Fishnet"***

Recentemente la fabbricazione e l'ottimizzazione di nano aperture periodiche attraverso strati di metalli nobili ha riscosso molta attenzione sia per l'interesse verso fenomeni fisici non comuni sia per le potenziali applicazioni alla nano-ottica e alla biosensoristica. In particolare i metamateriali composti da strati metallo-dielettrici sovrapposti e perforati da aperture periodiche, conosciuti come strutture a forma di spina di pesce, sono oggi tra i migliori candidati per studiare alcuni fenomeni fisici non comuni, come la rifrazione ad angolo negativo. La tesi di dottorato riassume lo studio della propagazione delle onde elettromagnetiche in strutture periodiche, in particolare nelle "*Fishnet*". La propagazione di onde elettromangetiche nelle *Fishent* genera una proprieta' non comune: l'indice di rifrazione negativo. L'obbiettivo principale della tesi e' quello di studiare l'origine dell'indice di rifrazione negativo e la sua dipendenza dai parametri geometrici a partire da strutture di base come la Fishnet a tre strati fino a strutture piu' evolute come la Fishnet a multi strato. Dei metodi e modelli effettivi per l'estrazione dei parametri complessi saranno inizialmente considerati per lo studio preliminare. Tuttavia per un'indagine piu' rigorosa verra' presentato un recente metodo modale adatto all'analisi di strutture omogenee fortemente accoppiate come le Fishnet a multistrato in cui anche i modi evanescenti, legati alla dissipazione del metallo, possono giocare un ruolo cruciale. Il metodo *FEM* di analisi modale e' basato sull'equazioni di Elmholtz in forma debole e rappresenta un potente metodo di indagine per studiare l'evoluzione dei modi complessi, alla base dell'indice effettivo di rifrazione negativo (parte reale e complessa), da un punto di vista piu' fondamentale.

Acknowledgement

I would like to express thanks to my supervisor, Prof. Filippo Romanato from the University of Padua, for his many suggestions and constant support during this research. I also would like to thank all the young and graduated researchers of the *LaNN* group of research in Padua, under the supervision of Prof. Filippo Romanato. I also wish to thank PhD. Denis Garoli and PhD Marco Natali for their cooperation with gaining the experimental results presented in Chapter 5 of this thesis. A very special thanks to PhD Pierfrancesco Zilio for many fruitful discussions which have helped to improve this thesis. I also wish to thank my friend Francesco P. for his constant humane support during these last three years in Padua.

1 Introduction

In the last few years, the term *metamaterials* can be found frequently in the literature. The prefix *meta* comes from Greek and means *beyond* and also *of a higher kind*. One can find various definitions of metamaterials and they are still being refined as new phenomena appear. According to a general definition, metamaterials are artificial structures which can be characterized by some unique properties that cannot be found in nature. These new properties emerge due to specific interactions with electromagnetic fields or due to external electrical control. The specific interactions are caused by inclusions (usually metallic), which are periodically (rarely randomly or irregularly) inserted into the hosting material. The existence of homogeneous substances with negative permittivity ε and/or permeability μ in nature was first discussed in 1967 by Veselago in (1). Theoretically, four kinds of substances according to the values of ε and μ were considered (see Figure 1-1).
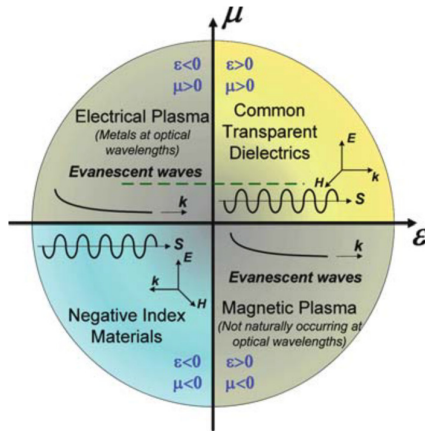
Figure 1-1. The parameter space for ε and μ. The two axes correspond to the real parts of permittivity and permeability, respectively. The dashed green line represents non-magnetic materials with μ=1

As shown in Figure 1-1, the real part of permittivity ε is plotted to the horizontal axis of the parameter space, while the vertical axis corresponds to the real part of permeability μ. Therefore materials with all possible combinations of ε and μ can be

placed in the parameter space. Conventional materials known to be transparent are found in the first quadrant, where both ε and μ have positive values. A negative value of $\varepsilon(\mu)$ indicates that the direction of the electric (magnetic) field induced inside the material is in the opposite direction to the incident field. Noble metals at optical frequencies are good examples for materials with negative ε, and negative μ can be found in ferromagnetic media near a resonance (2). No propagating waves can be supported in materials represented by the second and fourth quadrants, where one of the two parameters is negative and the index of refraction becomes purely imaginary. In the domain of optics, all conventional materials are confined to an extremely narrow zone around a horizontal line at $\mu=1$ in the space, as represented by the dashed line in Figure 1-1. Moreover in an anisotropic medium, the field vectors $\boldsymbol{E}$ and $\boldsymbol{D}$ are not necessarily parallel to each other; hence the permittivity must be in the form of a tensor rather than a scalar value. Anisotropic and strongly dispersive features generally occur in most of metamaterials studied thus far; for this reason, we should always specify the frequency and direction under consideration when we address any effective parameters in a metamaterial. Various kinds of passive artificial media are under consideration, and these media can be divided into two large classes. In one of the classes, the spatial period of the inclusions in the hosting material is small compared to the wavelength. This means that the spatial dispersion effects are weak. In the other case we have structures in which those characteristic sizes are comparable with the wavelength known as *photonic crystal* (3). This is a situation of strong spatial dispersion, and the usual material description in terms of its permittivity and permeability loses its sense.

In (1) Veselago introduced the term *left-handed materials* for metamaterials. This term is widely used today, but can have different meanings from different points of view (4) (5). Several other names for these materials are also in use: mentioning that the term metamaterial should be used for three-dimensional volumetric or bulk structures.

- Veselago media

- Media with simultaneously negative permittivity and permeability

- Double-negative(DNG) media

- Negative index of refraction (NIR or NRI) media

- Negative phase-velocity media

- Backward-wave (BW) media

- Left-handed (LH) media

Media with only one negative parameter are sometimes called single-negative (SNG), specifically either ε-negative (*ENG*) or μ-negative (*MNG*) media. Many authors use the term left-handed media. It should be noted that when we say something is left- or right-handed, this term can have three different denotations in electromagnetism:

- Right- or left-handed in structure of materials
- Right- or left-handed in polarization of the propagating media
- Right- or left-handed basis of the three vectors characterizing the wave

The first meaning comes from the basic sense: for example, the left hand cannot be superimposed on the right hand by only making rotations and translations. They are mirror images of each other. The Greek word gives us the term chiral for objects that are right- or left-handed (e.g., screws). Chiral materials can be formed from chiral objects: when one mixes left-handed objects into a neutral host medium the result is a left-handed material. The well-known effect of chirality on wave propagation through such a medium is that the polarization plane rotates along the propagation path (6). Another meaning of right- or left-handed orientation is related to the polarization of the electromagnetic wave, which is determined by the behaviour of the electric field

vector. Because there are two possibilities in the direction of the rotation, we come to two choices of polarization: left-handed and right-handed. The orientation of the polarization is dependent on the direction of observation. The third use of right- or left-handed orientation is more abstract and is connected with the vector system associated with wave propagation. In an "ordinary" medium with $\mu > 0$ and $\varepsilon > 0$, the system (E, H, k) forms a right-handed triplet, whereas if ε and μ are negative, the triplet is left-handed. For such media, the propagation constant k is opposite to the power flow. From these examples it is obvious that the widely used term left-handed is not very suitable for metamaterials. The term gives the impression that the right- or left-handed orientation is a characteristic of the material itself, which generally is not true. Moreover (see Figure 1-2), it is only the triplet (E, H, k) that is left-handed; taking instead (E, B, k) or (D, H, k) we can derive that these are both right-handed, independently of the signs of ε and μ. The right- or left-handed orientation of the field and the wave vector only makes sense for linearly polarized waves. The terms left-handed (LH) media and right-handed (RH, i.e., conventional) media, however, are widely used, particularly in metamaterials based on transmission line theory.

RHM   **LHM**
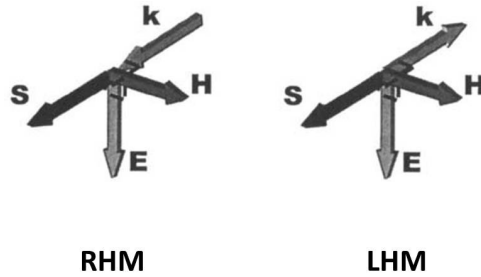
Figure 1-2. Orientation of the field quantities E,H, Poynting vector S, and wave-vector k in right-handed media (RHM) and left-handed media (LHM)

1.1   Historical overview

In general, structures in which the backward wave can propagate may be found in many fields of physics. Backward waves were observed in mechanical systems by Lamb (7) in 1904. Seemingly, the first person who discussed backward waves in

electromagnetism was Schuster (8). He briefly noted Lamb's work and gave a speculative discussion of its implications for optical refraction, when a material with such properties were to be found. Around the same time, Pocklington (9) showed that in a specific backward-wave medium a suddenly activated source produces a wave whose group velocity is directed away from the source, while its phase velocity moves toward the source. In electromagnetism, metamaterials are characterized by negative permittivity and permeability. One of the first references to substances with negative material parameters comes from Mandelshtam (10), who proposed the idea of the reversed Snell's law. The possibility of negative phase velocity of an electromagnetic wave was predicted by Sivukhin (11). He observed that media with negative parameters are backward-wave media, but had to state that "media with $\varepsilon < 0$ and $\mu < 0$ were not known. The question of the possibility of their existence was not clarified." The first more extensive paper on hypothetical materials with negative permittivity and permeability was introduced by Veselago (1). For centuries people had believed that the refraction index can only be positive, but in this paper it was suggested that it could also be negative. The term left-handed material was used for the first time there. In the case of $\mu > 0$ and, $\varepsilon > 0$ the vectors $\boldsymbol{E}$, $\boldsymbol{H}$ and $\boldsymbol{k}$ form a right-handed triplet, and if $\mu < 0$ and $\varepsilon < 0$, they form a left-handed set as just pointed above. Since vector $\boldsymbol{k}$ is in the direction of the phase velocity, it is clear that left-handed substances are substances with negative group velocity, which occurs in particular in anisotropic substances or when there is spatial dispersion. In (1), several examples are discussed, including the reversed Doppler effect, the reversed Vavilov-Cerenkov effect, and the refraction of a ray at the boundary between left-handed and conventional media. Veselago introduced the term *rightness*, which can be positive or negative, to divide materials into two categories: right-handed and left-handed. The question of the proper use of the term left-handed was discussed above.
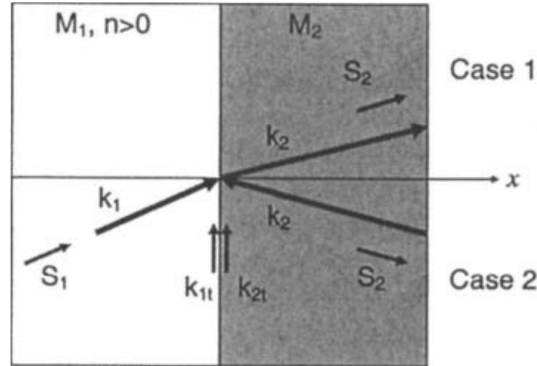
Figure 1-3. Refraction at two-medium interface as determined by phase matching.

One way to understand negative refraction is through the idea of phase matching. To illustrate, consider the two-medium interface of Figure 1-3, where medium 1 (M_1) is an RHM and medium 2 (M_2) is unspecified for the moment. A plane wave originating in M_1 is incident on the interface with wave-vector k_1, and it establishes a refracted wave in M_2 with wave-vector k_2 such that their tangential components k_{1t} and k_{2t} are equal, according to the conservation of the wave momentum. Having specified the tangential components, we immediately recognize that there are two possibilities for the normal component of k_2: the first case, in which k_2 is directed away from the interface, and the second case, usually describing reflected waves, in which k_2 is directed towards the interface. These two cases are represented as *Case 1* and *Case 2* in Figure 1-3. By the conservation of energy, the normal components of the Poynting vectors $\boldsymbol{S_1}$ and $\boldsymbol{S_2}$ must remain in the positive z-direction through both media. Thus, *Case 1* depicts the usual situation in which M_2 is a conventional positive-index medium; however, if M_2 is a medium supporting propagating backward waves (*LHM*), then the wave-vector k_z must be directed oppositely to the Poynting Vector $\boldsymbol{S_2}$ (i.e., with a normal component in the negative z-direction). Therefore, refraction in media that support backward waves must be described by the second case, in which power is propagated along the direction of phase advance, and so is directed through a negative angle of refraction. Thus, M_2 can be seen to possess an effectively negative refractive index.

9

1.2 The recent interest in metamaterial.

The paper published by Veselago in 1967 provoked considerable interest at the time. Surprisingly, however, real metamaterial research did not start until about three decades later, when several seminal papers were published. The idea of having negative effective material parameters and thus a negative refractive index was stunning, but it lacked practical applications. In 1999, Pendry et al. (12) showed that microstructures built from nonmagnetic conducting sheets exhibit an effective magnetic permeability μ_{eff}, which can be tuned to values not accessible in naturally occurring materials, including large imaginary components of μ_{eff}. The microstructure is on a scale much smaller than the wavelength of radiation, and is not resolved by incident microwave radiation. An example of such a structure is an array of non-magnetic thin sheets of metal, planar metallic split-rings or so called Swiss rolls (12). Using Swiss rolls, a very strong magnetic response can be achieved. The idea of a material with a negative refractive index was worked out by Smith in 2000 in the paper (13). There he drew inspiration from Veselago's paper and proposed an artificial material which can produce both negative effective permittivity and negative effective permeability. Veselago had been looking for such a material for many years, and had expended huge amounts of time and resources, but unfortunately he did not find the proper way. He had intended to build the metamaterial as a mixture of natural materials with electric and/or magnetic anisotropy. The problem was always with high losses and the resonance of magnetically and electrically anisotropic materials at different frequencies . The idea of Smith et al. was different, since it utilized a composite material, not a homogeneous one. One of the revolutionary metamaterial applications was proposed in 2000 by Pendry in (14). It is well known that with a conventional optical lens the sharpness of the image is always limited by the wavelength of light used for illuminating the object. An unconventional alternative to a lens, a slab of negative refractive index material, has the power to focus all Fourier components of a two-dimensional image, even those that do not propagate (evanescent waves). The waves decay in amplitude, not in phase,

10

as the distance from the object plane grows. Therefore to focus them we need to amplify them rather than to correct their phase. Pendry showed that such "superlenses" can be implemented in the microwave band with current technology. With this new lens both propagating and evanescent waves contribute to the resolution of the image (14). Therefore there is no physical obstacle to perfect reconstruction of the image beyond the practical limitations of apertures and perfection of the lens surface. In 2000 Smith et al. (13) demonstrated a composite medium, based on a periodic array of interspaced conducting nonmagnetic split-ring resonators (*SRRs*) and straight wires, which exhibits a frequency region in the microwave regime with simultaneously negative values of effective permeability μ_{eff} and permittivity ε_{eff}. This array forms an anisotropic medium. Several works with theoretical derivation of the negative refraction index in metamaterials composed of *SRRs* and thin wires have been presented (15) (16). One of the first fabricated and measured structures was introduced by Shelby in 2001 (17). The material consists of a two-dimensional array of repeated unit cells of copper strips and *SRRs* on interlocking strips of a standard circuit board material. This structure can be referred to as a bulk form, and was later studied by many authors in various modifications. By measuring the scattering angle of the transmitted beam through a prism fabricated from this material, the negative effective refractive index *n* was observed.

1.3   Main research directions in metamaterials

After publication of the seminal papers (13),(14),(15), a great number of research groups started to work in this novel and promising direction. Many different approaches and areas of particular interest appeared, but only the main approaches will be listed below.

1.3.1 Negative permittivity

It is well known that plasmas are described by a permittivity function that becomes negative below a plasma frequency ω_p , causing the propagation constant in the plasma to become imaginary. In this frequency region, electromagnetic waves incident on the plasma suffer reactive attenuation and are reflected. Thus, the plasma frequency bears a resemblance to the modal cutoff frequencies of particular electromagnetic waveguides, below which the waveguide environment can be perceived as an inductively loaded free space, as observed in 1954 by R. N. Bracewell (18). The idea of modeling plasmas using artificial dielectrics was examined as early as 1962 by Walter Rotman (19). His analysis, however, could not explicitly consider the permittivity of the media and, instead, was limited to the consideration of their index of refraction. Rotman noted that an isotropic electrical plasma could be modeled by a medium with an index of refraction below unity, provided that its permeability was near that of free space. Consequently, the sphere and disk-type media were excluded, since the finite dimensions of these conducting inclusions transverse to the applied electric field give the effective medium a diamagnetic response. What remained was the "rodded" dielectric medium, or conducting strip medium, consisting of thin wire rods oriented along the incident electric field. The dispersion characteristics of this medium showed that it does, indeed, behave like a plasma. The idea of a negative permittivity was implicit in many such works, but it was not until nearly a quarter-century later, when Rotman's rodded dielectric was rediscovered, that it was made clear exactly how a wire medium resembled a plasma. It is evident that in the construction of electromagnetic structures of any sort in the microwave range, we rely on the properties of metals. Essentially, metals are plasmas, since they consist of an ionized "gas" of free electrons. Below their plasma frequency, the real component of the permittivity of bulk metals can be said to be negative. However, the natural plasma frequencies of metals normally occur in the ultraviolet region of the electromagnetic spectrum, in which wavelengths are extremely short. This condition certainly precludes the use of realizable artificial

dielectrics in the microwave range, which, moreover, must operate in the long wavelength regime. Although the permittivity is negative at frequencies below the plasma frequency, the approach toward absorptive resonances at lower frequencies increases the dissipation, hence the complex nature of ε. Thus, to observe a negative permittivity with low absorption at microwave frequencies, it would be necessary to somehow depress the plasma frequency of the metal. This problem was addressed by Pendry et al. (20) (and simultaneously by Sievenpiper et al. (21)), who proposed the familiar structure of Rotman consisting of a mesh of very thin conducting wires arranged in a periodic lattice, but approached the problem from a novel standpoint. Due to the spatial confinement of the electrons to thin wires, the effective electron concentration in the volume of the structure is decreased, which also decreases the plasma frequency. More significant, however, is that the self-inductance of the wire array manifests itself as a greatly enhanced effective mass of the electrons confined to the wires. This enhancement reduces the effective plasma frequency of the structure by many orders of magnitude, placing it well into the gigahertz range. Thus, an array of thin metallic wires, by virtue of its macroscopic plasma-like behavior, produces an effectively negative permittivity at microwave frequencies.

1.3.2 Negative permeability

Before dismissing the possibility of achieving $\mu < 0$ using natural isotropic substances, Veselago momentarily contemplated the nature of such a substance. He imagined a gas of magnetic "charges" exhibiting a magnetic plasma frequency, below which the permeability would assume negative values. The obstacle, of course, was the constitutive particle itself, the hypothetical magnetic charge. It is important to note that in the effort to synthesize a negative effective permittivity, Rotman and Pendry relied on the analogies their structures shared with the simplified electrodynamics of natural substances. Indeed, as acknowledged by Veselago himself (1), it is a much more

difficult task to synthesize an isotropic negative permeability, for which there exists no known electrodynamics precedent.
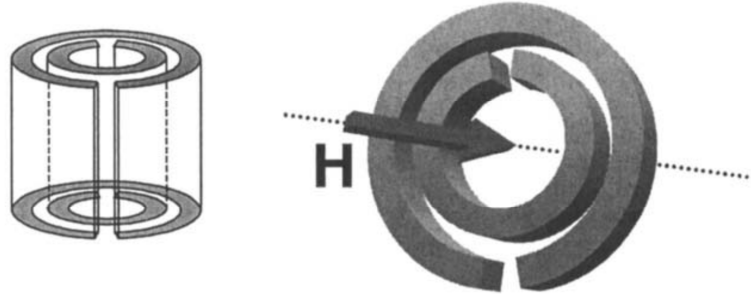
Figure 1-4. The split-ring resonator (SRR) of Pendry et al. [14] in cylindrical and planar form, activated by a magnetic field normal to the plane of the rings.

In 1999, Pendry et al. (22) claimed to have developed micro-structured artificial materials exhibiting strange magnetic properties. The work first developed expressions for the magnetic properties of materials resembling the wire mesh, in which the fields and currents are oriented along the wire axis. Ultimately, the work concluded that such materials are strictly diamagnetic and that the permeability approaches the free-space value as the radius of the wires is decreased, a response which may be expected of simple artificial dielectrics (23). However, by giving the cylinders an internal electromagnetic structure resembling a parallel-plate capacitor wrapped around a central axis, Pendry et al. noticed a very different behavior. The resulting split-ring resonator (SRR), depicted in Figure 1-4, exhibits strong electric fields, supported by a very large capacitance, between the rings. Furthermore, although currents cannot traverse the gaps, the application of magnetic fields oriented normal to the plane of the rings induces simultaneous currents in both rings. This synthesized capacitance, along with the natural inductance of the cylindrical structure, results in a resonant response characterized by an effective relative permeability of the form

$$\mu_{eff} = 1 - \frac{\pi r^2 \,/\, a^2}{1 - \dfrac{i2l\rho}{\omega\tau\mu_0} - \dfrac{3l}{\pi^2\mu_0\omega^2 Cr^3}} \qquad (1.1)$$

which has been appropriately modified from the original to refer to a $\exp(i\omega t)$ time variation. Here, r represents the radius of the *SRR*, a is the lattice spacing of *SRRs* lying in the same plane, l is the spacing between planes, ρ represents the resistive losses of the metal sheets, and C is the sheet capacitance between the two sheets. It is clear from the resonant form of μ_{eff} that an artificial medium composed of *SRR* arrays would exhibit an effective permeability that attains large values near the resonance, limited only by the amount of resistive loss. This resonance frequency is given by

$$\omega_0 = \sqrt{\frac{3l}{\pi^2\mu_0 Cr^3}} \qquad (1.2)$$

However, μ_{eff} seems to possess another, more familiar trait: When $\rho \to 0$, the permeability expression can become negative if the second term of (1.1) is greater than one. This occurs at an effective magnetic plasma frequency ω_{mp}, given by

$$\omega_{mp} = \sqrt{\frac{3l}{\pi^2\mu_0 Cr^3(1 - \dfrac{\pi r^2}{a^2})}} \qquad (1.3)$$

The quantity $\pi r^2 \,/\, a^2$ which we shall denote F, is the fractional area occupied by the rings, or filling factor. When embedded in air, arrays of SRRs appear to exhibit a stop-band in the frequency region enclosed by ω_0 and ω_{mp}, suggesting that the permeability is negative in this region. Although the phenomenon is evidently narrowband, the magnetic plasma frequency can be happily placed in the gigahertz range. Thus, comprising purely nonmagnetic materials, the *SRR* array of Pendry et al. had successfully simulated an artificial magnetic plasma, the substance hypothetically

envisioned by Veselago, for which the effective permeability assumes negative values at microwave frequencies. The role of the magneto-electric coupling in *SRRs* can be minimized by the proper choice of geometrical dimensions or by applying symmetries in the design, but some residual coupling still remains. A method for calculation and measurement of the magneto-electric coupling (bianisotropy) of *SRRs* is proposed in (24) (25). The possibility of designing isotropic 3D magnetic resonators by properly arranging modified *SRRs* was studied in .

1.3.3 Perfect lens

From optics it is well known that no lens can focus light on an area smaller than the square wavelength, thus it is not able to provide an image of objects smaller than the wavelength of the light illuminating the object. The hypothetical perfect lens overcomes this rule. Unlike conventional optical components, it will focus both the propagating spectra and the evanescent waves, and thus be capable of achieving diffraction-free imaging. In 2000, Pendry (14) predicted an intriguing property of such a LH lens (later refined in (26), (27), a solution of a spherical perfect lens was given in (28)). Such a lens is formed by a planar slab of double-negative material. Currently, samples of double-negative materials are created mainly in the microwave region (29), (30), (31), (32) due to the difficulty of achieving a strong magnetic response at higher frequencies. Planar lenses, however, can operate only when the source is close to the lens (the distance is related with the slab thickness). For practical applications, such as telescopes and microwave communications, distant radiation needs to be focused. In order to focus far field radiation, the negative refractive index (*NRI*) lens with a concave surface is generally used. The monochromatic imaging quality of a conventional optical lens can be characterized by the five Seidel aberrations: spherical, coma, astigmatism, field curvature, and distortion. In (33), aberrations in a general *NRI* concave lens have been studied by Smith and Schurig. They found that this lens allows reduction or elimination of more aberrations than can be achieved with only

positive refractive index media. The 3D superresolution in metamaterial slabs was experimentally shown in (34), and the theory was later generalized to an arbitrary subdiffraction imaging system (35). The sensitivity of *NRI* lens resolution to the material imperfection is studied in (36). The creation of left-handed materials at *THz* frequencies and in the optical range meets with problems in getting the required magnetic properties (37) (38), which have to be created artificially. In the absence of magnetic properties, the lenses formed by materials with negative permittivity only (for example, silver at optical frequencies (14), (39) or an array of metallic nanorods (40)) are still able to create images with subwavelength resolution, but the operation is restricted to p-polarization only and the lens has to be thin as compared to the wavelength. This idea was confirmed by experimental results (41), which demonstrated the reality of subwavelength imaging using silver slabs in the optical frequency range. The resolution of such lenses is restricted by losses in the silver. At the present time there is no recipe for increasing the thickness of such lenses other than the introduction of artificial magnetism.

1.3.4 Metamaterials cloaks

Another interesting practical application of metamaterials is a cloaking device. Let us imagine an object covered by a hypothetical material which is able to bend the electromagnetic waves passing through so that they go around the object and then return undisturbed to their original trajectories. Then for an observer outside it seems that the object is "invisible". The idea was first suggested by Pendry et al. in (42) and then elaborated in (43) where spherical and cylindrical cloaks were worked out. The authors described a method in which the transformation properties of Maxwell equations and the constitutive relations can yield material descriptions that allow such manipulations with the beam trajectory. Leonhardt described a similar method, where the two-dimensional Helmholtz equation is transformed to produce similar effects in the geometric limit (44). Probably the first practical realization of a two-dimensional cloaking device was demonstrated under certain approximations in (45). A copper

cylinder was "hidden" inside a cloak constructed with the use of artificially structured metamaterials, designed for operation over a band of microwave frequencies. The cloak decreases the scattering from the hidden object while at the same time reduces its shadow, so that the cloak and object combined begin to resemble empty space. No real three-dimensional cloaking device has been fabricated so far.

1.3.5 Chiral and bi-anisotropic materials

Chiral media provide another example of metamaterials with promising properties (6). In chiral media, the spatial geometrical character of the internal structure (anti-symmetry or non-symmetry with respect to the mirror reflection) rotates the polarization of the propagating plane wave. This rotation is due to the magneto-electric coupling caused by chiral elements. The bianisotropy of *SRRs* was studied in (46). A way to obtain negative refraction with chiral materials was proposed by Pendry in (47) and later extended by several research groups, see, e.g., (48), (49), (50), (51), (52). The advantage of these structures is that they can provide both negative effective permittivity and negative effective permeability with just one particle instead of the two (e.g., *SRRs* and wires) needed in conventional metamaterials.

1.3.6 Tunable metamaterials

Most of the practical metamaterial implementations so far have been narrow-band resonant structures. No wonder that researchers would like to achieve more broadband and tunable devices. Metamaterial applications can be divided into two big groups: the first one usually uses active devices to tune the capacitance or inductance in order to achieve left-handed behavior in various frequency bands (varactor-loaded split-ring resonators (53) coupled to micro-strip lines can lead to metamaterial transmission lines with tuning capability (54), a tunable impedance surface etc.. whereas the other group utilizes generally anisotropic natural materials with properties that are dependent on

external electric or magnetic field intensity. Such examples are nonlinear dielectric substrates (55), tunable phase shifters based on ferroelectric films (56) which have properties dependent on external fields. Utilization of micro-electro-mechanical structures (*MEMS*) as tunable capacitors is shown in (57). Another extensive class of tunable metamaterials is formed by liquid crystals. The properties of liquid crystals can be changed easily by applying an external electric field. Hence, they are adaptable for tuning. Bush and John (58) predicted the tunability of the band structure in photonic crystals utilizing liquid crystals. Takeda and Yoshino (59) showed tunable refraction effects in photonic crystal structures infiltrated by liquid crystals. Recently (60) was analyzed numerically the optical response and effective macroscopic parameters of Fishnet metamaterials infiltrated with a nematic liquid crystal which enables switchable optical metamaterials, where the refractive index can be switched from positive to negative by an external field.

1.3.7   Optic metamaterials.

The idea of metamaterials has been quickly adopted even to *THz* and optical frequencies, since nanofabrication and sub-wavelength imaging have developed rapidly in recent years. When the light interacts with a conventional material, then from the electric and magnetic component of the light only the electric component probes the atoms of a material effectively whereas the interaction with the magnetic component is usually weak. However, metamaterials allow both components of the light to be coupled, when they are designed properly. This can lead to fascinating applications such as super-lenses, optical nanolithography, "invisibility cloaks" etc. The metamaterials known from microwave frequencies, however, are difficult to fabricate at optical frequencies. For materials at optical frequencies, the dielectric permittivity ε is very different from that in a vacuum, whereas the magnetic permeability μ (for natural materials) is close to that in a vacuum. This is because of the weak interaction with the magnetic component of the light, mentioned above (61). Conventional SRRs operating at GHz frequencies were scaled down up to 1 *THz* frequencies (62), and

19

modified SRRs up to tens of *THz* (63), (64) (see Figure 1-5). The first experimental demonstrations of a negative refractive index in the optical range were accomplished, nearly at the same time, for pairs of metal rods (65). This redesign process (see Figure 1-5) leads to the development of the double-Fishnet negative index structure (64), which has been used in experiments by various groups(64), (66), (67), (68), (69), (70), (71), (72). In essence, a single functional layer of this structure comprises a perforated metal–dielectric–metal sandwich. The uniaxial double-Fishnet structure exhibits an effective negative index of refraction for light propagating normal to the layers.
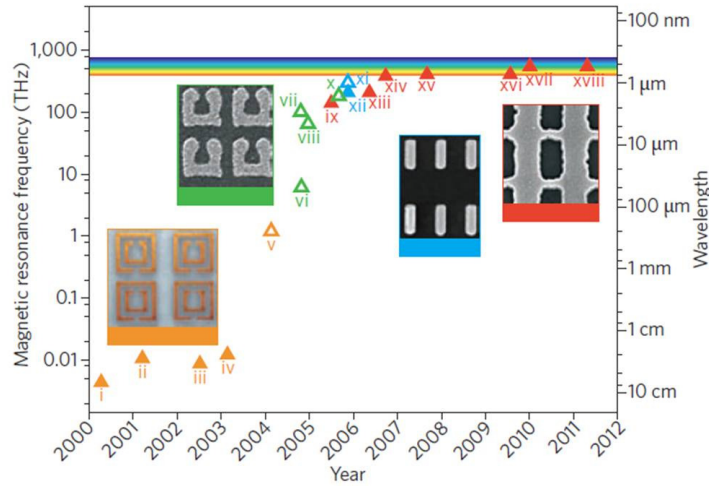
Figure 1-5. Progress in metamaterial operating frequency over the past decade. The operating frequency of metamaterials with negative magnetic permeability *μ* (empty triangles) and negative index of refraction *n* (solid triangles) is shown on a logarithmic scale ranging from microwave to visible wavelengths. Orange: structures based on double SRRs; green: U-shaped SRRs; blue: metallic cut-wire pairs; red: negative-index double Fishnet structures. The four insets show optical or electron micrographs of the four types of structure. Figure from Ref. (73).

From 2007 the research direction oriented towards the realization of 3D optical metamaterials. Figure 1-6 resumes the recent progress toward the 3D metamaterial realization. The evolution for the Fishnet metamaterials is depicted in Figure 1-6a. It consists of stacking N>1 functional layers of the double-Fishnet structure (forming *2N+1* layers in total).

Figure 1-6.Fig 3D photonic-metamaterial structures. (a) Double-Fishnet negative-index metamaterial with several layers. (b) 'Stereo' or chiral metamaterial fabricated through stacked electron-beam lithography. (c) Chiral metamaterial made using direct-laser writing and electroplating . (d) Hyperbolic (or 'indefinite') metamaterial made by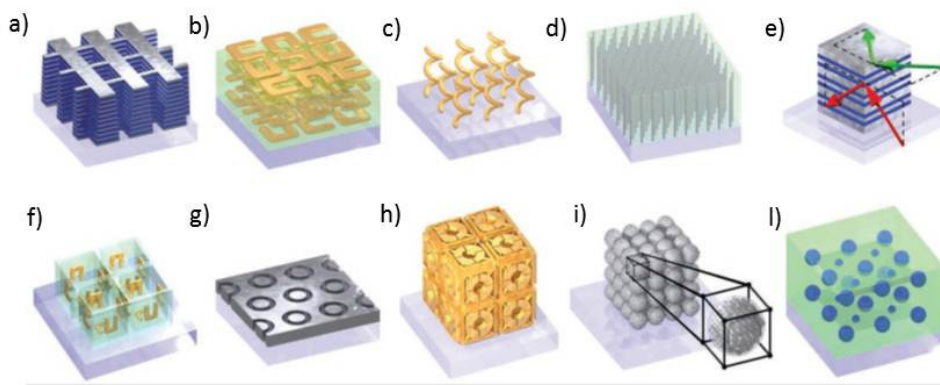 electroplating hexagonal-hole-array templates . (e) Metal–dielectric layered metamaterial composed of coupled plasmonic waveguides, enabling angle-independent negative n for particular frequencies. (f) SRRs oriented in all three dimensions, fabricated using membrane projection lithography . (g) Wide-angle visible negative-index metamaterial based on a coaxial design . (h) Connected cubic-symmetry negative-index metamaterial structure amenable to direct laser writing. (i) Metal cluster-of-clusters visible-frequency magnetic metamaterial made using large-area self-assembly . (l) All-dielectric negative-index metamaterial composed of two sets of high-refractive-index dielectric spheres arranged on a simple-cubic lattice. Figure taken from Ref.(73)

1.4   The aim of the thesis

The general aim of this work is to study the propagation of electromagnetic waves in periodic structures, namely in "fish-net" like metamaterial structures (see structure depicted in Figure 1-6a). It is well known that, when wavelengths much larger than the periodicity cross these artificial systems, they can enable uncommon properties such as the negative refraction index and the negative phase advance respect to the power flow direction. The purpose of this thesis is to study the origin of the negative refraction and its dependence on the geometric parameters of the structures. An average method for the extraction of the effective parameters and the introduction of a simple LC circuit formalism is commonly adopted for the investigation and some clarification about the refractive index behavior under a parametric variation of the fishnet. However this effective approaches to metamaterials are sometime insufficient to

explain the intrinsic nature of such structures being strictly related to their complex dispersions. For this reason a robust approach toward the microscopic investigation of periodic structures is presented and for the first time it is also extended to the case of plasmonic/photonic crystal slabs. Within this (*FEM*) modal method based on the weak form of the Elmholtz's equation one can accurately extract all the complex Bloch-modes of an elettromagnetic periodic system thus leading to the possibility of calculating the modes losses. The method offers great reliability in computational time, extraction of complex *k*-bands, independence by any shape of periodic holes and kind of materials, extraction of complex isofrequency contours, for either 2D periodic photonic/plamonic crystal slabs or 2D-3D photonic/plamonic crystals. The thesis can be resumed as fellow: the introduction gives a brief historical overview of metamaterial research, and the main research directions in this area are outlined. The first part of the thesis summarize the theoretic framework for the investigation of the average properties of metamaterials. In the second part we report a design and a parametrical analysis of a *Fishnet* in the optical spectral range. In particular the dependence of both the magnetic and the electric resonance on the geometric features of the *Fishnet* is investigated in the optical frequency spectrum. The transmission and reflection coefficients and distribution of the electric field within the lattice were calculated by means of *FEM* electromagnetic simulations. Moreover the properties of *Fishnet* metamaterial have been investigated for a multi-layered structure. The *SPPs* modes propagating inside the stacked metamaterial have been identified and enumerated. We show that the asymptotic bulk properties for a multilayered Fishnet metamaterial are easily reached by staking just more than 3-functional layers along the propagation direction. The third part of the thesis reports a preliminary result on the nanofabrication of *Fishnet* type Au/dieletric/Au metamaterial stacks. Nano-hole arrays have been realized on Au(30 nm)-dielectric(50nm)-Au(30nm)/ITO stacks by means of direct ion milling with *FIB* using a *FEI* Nova 600i instrument. Finite element method simulations were used to design the structures and to foresee their optical behavior. The bianisotropic approach for a more accurate extraction of the physical parameters is presented. In the last part of the thesis a *FEM* modal method based on the weak form of the Helmholtz's

equation is presented. The dispersion characteristic of plasmonic/photonic crystals in the shape of a periodic slabs or of a 2D-3D periodic structure are calculated and the method is applied on a *Fishnet* metamaterial. The complex $\boldsymbol{k}$-band diagrams are calculated together with the isofrequency dispersion curves. The method allows the identification of the left-handed modes and the calculation of losses in metal. The simulation of the negative refraction from a *NRI* prism in the shape of a wedge is also showed. The electric and magnetic modes generating the *NRI* are than identified with plamonic resonances originating by the coupling of the incident momentum light with the grating diffractive orders. In Chapter 5 a preliminary fabricated sample of Fishnet metamaterial is reported. Moreover the presence of bianisotropy (always present in fabricated sample) is studied by means of scattering parameters. In Chapter 6 and 7 a powerful modal method based on weak formulation within the *FEM* environment is reported. This method represent a very useful tool for the investigation of photonic and plamonic structures allowing for the extraction of the complex photonic and plamonic dispersion curves of the Bloch-modes.

2   Effective method approach to metamaterials

Materials composed of small elements are known to respond as continuous media when the operating wavelength is much larger than the individual constituents. A classic example of such materials are natural dielectrics that can be described by a single parameter, the electric permittivity ε. All the negative and positive charges in a dielectric medium are bound to their location by atomic forces and are therefore not free to move like in a conductor. Under the influence of an external electric field, however, these assemblies of negative and positive charges may slightly reorganize, which results in the creation of bound electric dipoles. From a macroscopic point of view, the orientation of these dipoles generates a polarization vector $\boldsymbol{P}$ that influences the electric flux density $\boldsymbol{D}$ such as $\boldsymbol{D} = \varepsilon_0 \boldsymbol{E} + \boldsymbol{P}$, where $\boldsymbol{E}$ is the external applied electric field. This allows one to define a general permittivity ε such that $\boldsymbol{D} = \varepsilon \varepsilon_0 \boldsymbol{E}$, where naturally ε is defined in terms of the polarization vector. Similarly, magnetic media are described by a magnetic permeability μ, and ε and μ represent the constitutive parameters essential to the macroscopic Maxwell equations. In our case, the metamaterials are composite structures designed to exhibit specific electromagnetic properties at some particular wavelengths that are much larger than the elementary constituents. It is therefore legitimate to look for homogeneous or effective medium parameters, typically an effective permeability. Like in the case of more standard media, these constitutive parameters directly represent the properties of the medium: isotropic metamaterials should be described by scalar constitutive parameters while anisotropic ones should be described by second rank tensors $\bar{\varepsilon}$ and $\bar{\mu}$, losses induce an imaginary part to these parameters, frequency dispersion yields frequency-dependent parameters, non-locality makes them spatially dispersive (dependent on k), the passive nature of metamaterials forces the imaginary parts to be positive, reciprocity imposes conditions on the tensors, etc.

The homogenization procedure therefore involves two steps:

1. A hypothesis, more or less refined, on the characteristics of the medium (isotropic vs. anisotropic, lossless vs. lossy, etc). Paradoxically, the properties of the metamaterial are initially unknown, and yet a model has to be chosen to perform the homogenization procedure. Therefore, the model should also be tested a *posteriori*.

2. The determination (or retrieval) of the corresponding constitutive parameters using numerical or analytical algorithms.

Once the overall model has been ascertained, the next step is to obviously determine the numerical values of the components of the permittivity and permeability tensors. The number of unknowns is directly related to the model chosen and dictates the number of equations that must be obtained from measurements (either experimental measurements or numerical simulations). For example, a simple lossy isotropic dielectric material exhibits two unknowns, the real and imaginary parts of the scalar permittivity, which can be obtained from one complex measurement such as the reflection and/or the transmission coefficients.

Before detailing the homogenization procedures, it is necessary to say a few words about the limitations of homogenization. Although we are interested inhomogenizing metamaterials, the range of applicability of such process must be carefully examined. In particular, homogenization would not be valid under the following conditions:

1. When the constituents are not much smaller than the operating wavelength. This includes metamaterials with unit cells large or comparable to wavelength of the radiation, as well as dielectric photonic crystals operating close to hale wavelength.

2. When the wave propagation inside the material cannot be described by a single propagating mode. Such situation occurs for example close to the resonance of some constituents of the metamaterials.

Failing to comply with these conditions may produce unphysical artifacts in the frequency-dependent retrieved parameters, the most common of which are an anti-

resonance of the permittivity (with an associated negative imaginary part) at the location of the resonance of the permeability (74), and possibly a truncated resonance of the index of refraction as pointed out in Koschny et al.(2005). These artifacts have been suggested to be due to the fact that the periodicity of the medium becomes visible at the corresponding frequencies, making the homogenization hypothesis less accurate. A conservative ratio of about 30 between the wavelength and the size of the unit cell has been proposed for the homogenization hypothesis to be very well justified, although most of the metamaterials realized to date exhibit a ratio of about 10 at best.

Typically one can deals with two distinct approach in order to determine the constitutive parameters of an effective medium once: one consist on averaging the internal fields over some relevant volume in the medium and the other is based on the extraction from the reflection and transmission coefficients.

There are several methods based on the fields average more or less rigorous and more or less valid under certain geometries and materials under study. The Maxwell-Garnett approximation, which is essentially the quasi-static generalization of the Clausius Mossotti electrostatic approximation, has been used widely to calculate the bulk electromagnetic properties of inhomogeneous materials (75). The component with the largest filling factor is considered to be a host in which other components are embedded and the field induced in the uniform host by a single inclusion (assumed to be spherical or elliptical) is calculated and the distortion of this field due to the other inclusions is calculated approximately. The Maxwell–Garnett approach incorporates the distortions due to the dipole field on an average and has been very successful in describing the properties of dilute random inhomogeneous materials. There are other effective medium theories (76), (77) for high filling fractions that include more residual interactions or higher multi-pole effects. We should also note that there are more mathematically rigorous homogenization theories (78), which analyses the fields in an asymptotic expansion in terms of the microscopic length-scale associated with the inhomogeneities, which is however beyond the scope of this doctoral thesis.

In the case of periodically structured materials,. the periodicity, first of all, implies that the averaging need not be over orientational and density fluctuations.

Another approach   (12) was first used to discretize Maxwell's equations on a lattice and it is essentially based on the fields averaging of the unit cell of the lattice (assumed to be simple cubic).

The effective medium parameters determined from any such averaging process should be unique and independent of the manner of the averaging process. Likewise, it should give unique medium responses to applied fields, and it should be possible to uniquely determine the scattered fields for the metamaterial. In fact, experiments usually access only the emergent quantities such as the reflection and transmission through (say) a slab of the effective medium and not the internal microscopic fields.

The method which will be more extensively presented is based on the extraction of the complex materials parameters from the reflection and transmission coefficient and it is traditionally overwhelmingly used in the metamaterial scientific community (79), (80), (81), (82), (83), (84), (85).

This method is appealing because of its relative simplicity to set up in an experimental configuration, as well as its numerical efficiency since the electromagnetic fields need only to be computed over surfaces instead of volumes. In this procedure, the reflection and transmission coefficients (R and T) are used as the linking information between the incident electromagnetic field and the constitutive parameters, the latter relationship being essentially the purpose of inversion or parameter retrieval algorithms.

2.1   The standard retrieval method

The first step is to determine the relationship between the incident, reflected, and transmitted fields and the reflection/transmission coefficients. In order to comply to the previous hypothesis, an effective medium is supposed to be of infinite extent in the transverse x- and y-directions and of finite extent in the propagation z-direction. We first assume that the medium is isotropic and homogeneous or symmetrically inhomogeneous respect to the direction of propagation normal to the effective medium slab. We illustrate the effective medium in Figure 2-1 indicated as region (2) embedded in two air domains (region (1) and (3)). The single propagating mode here is taken to be a plane wave, equivalent to the TEM mode in a parallel plate waveguide.
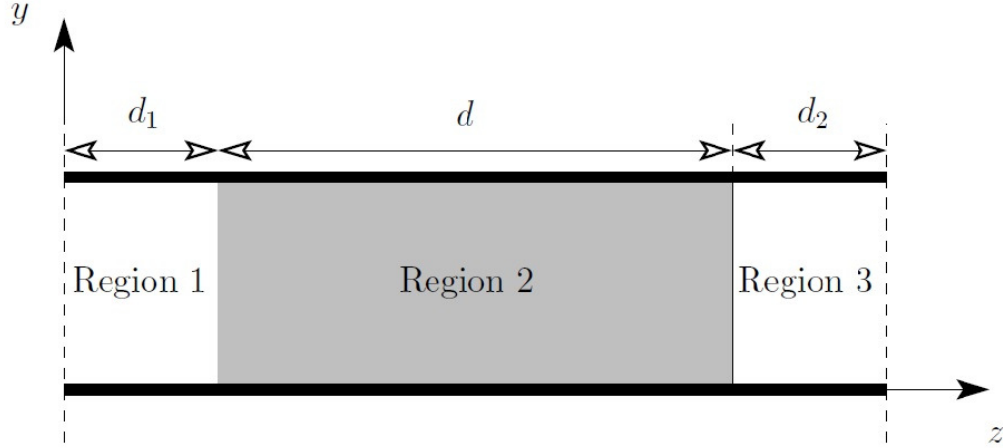
Figure 2-1.Measurement setup in a parallel-plate waveguide: the homogenized medium defines three regions and a reflection/transmission coefficient

The incident field propagating in the z-direction can be written as

$$\mathbf{E}_{inc}(z) = \hat{y}E_0 e^{ik_0 z} \tag{2.1}$$

A homogeneous effective medium is sought between the two interface boundaries at $z=z_1$ and $z=z_2$, thus defining an incident and transmitted region. The total field at z_1 and z_2 are so defined,

$$
\begin{aligned}
E_{tot}(z_1) &= \left(e^{ik_0 d_1} + \mathrm{Re}^{-ik_0 d_1} \right) \\
E_{tot}(z_2) &= Te^{ik_0(d_1+d)}
\end{aligned} \tag{2.2}
$$

In Eq. (2.2) the incident field is normalized to one.

For the sake of generality, it is useful to first define the one-dimensional transfer matrix, which relates the field on one side of a planar slab to the another. The transfer matrix can be definite from (82)

$$\mathbf{F}' = \mathbf{T}\mathbf{F} \tag{2.3}$$

where

$$\mathbf{T} = \begin{pmatrix} \cos(nk_0 d) & -iZ\sin(nk_0 d) \\ -iZ^{-1}\sin(nk_0 d) & \cos(nk_0 d) \end{pmatrix} \tag{2.4}$$

28

is the T-matrix and

$$\mathbf{F} = \begin{pmatrix} t_{E,1} \\ t_{H,1} \end{pmatrix}, \quad \mathbf{F}' = \begin{pmatrix} t_{E,2} \\ t_{H,2} \end{pmatrix} \tag{2.5}$$

In eq. (2.4) n and Z ($Z \equiv Z_{\text{eff}}$) are the effective refractive index and impedance of the effective medium respectively and $k_0 = 2\pi/\lambda$ is the free wavelength. In eq. (2.5) $t_{E,i}$, $t_{H,i}$ are the total field at the first (i=1) and last (i=2) interface of Region (2). For the particular configuration depicted in Figure 2-1 they are defined by normalizing Eq. (2) with ($e^{ik_0 d_1}$) as

$$
\begin{aligned}
t_{E,1} &= 1 - R\left(e^{-i2k_0 d_1}\right) \\
t_{H,1} &= 1 + R\left(e^{-i2k_0 d_1}\right) \\
t_{E,2} &= t_{H,2} = T\left(e^{ik_0 d}\right)
\end{aligned}
\tag{2.6}
$$

From Eq. (2.6) we define $r = R e^{-i2k_0 d_1}$ the reflectance amplitude and $t = T e^{ik_0 d}$ the transmittance amplitude (both modules and phases) at z_1 and z_2 respectively. Now Eq. (2.4) and (2.5) can be inserted in Eq. (2.3) and by inversion (83) it's easy to retrieve the constituent parameters (79):

$$n = \frac{N}{k_0 d} = \frac{\cos^{-1}\left(\dfrac{1 - (r^2 - t^2)}{2t}\right)}{k_0 d} \tag{2.7}$$

and

$$Z = \pm \sqrt{\frac{(1+r)^2 - t^2}{(1-r)^2 - t^2}} \tag{2.8}$$

Note that while the expressions for n and Z are relatively uncomplicated, they are complex functions with multiple branches, the interpretation of which can lead to ambiguities in determining the final expressions for ε and μ. One can resolve these ambiguities by making use of additional knowledge about the material. For example, if

the material is passive, the requirement that $Re(Z)>0$ fixes the choice of sign in Eq. (2.8). Likewise, $Im(n)>0$ leads to an unambiguous result for $Re(n)$ and $Im(n)$:

$$Re(n) = n' = (sign(N'')N' + 2\pi l) / (k_0 d) \tag{2.9}$$

$$Im(n) = n'' = sign(N'')N'' / (k_0 d) \tag{2.10}$$

with the conditions

$$\begin{aligned} Z' \geq 0 \\ n'' \geq 0 \end{aligned} \tag{2.11}$$

Where $sign(x)$ is equal to 1 if $x \geq 0$ and to -1 otherwise and l is an integer number. The branch factor is related to the number of wavelength that propagate inside the slab. By choosing short samples, it is therefore possible to ensure that the sample is smaller than one wavelength, thus automatically selecting $m = 0$ as solution. Such strategy works well with standard dielectric, where the constitutive parameters are usually reasonably small within the frequencies of interest and where their variations with respect to frequency are small. In the case of left-handed media, however, the parameters might take large absolute values, either at low frequencies for a Drude model or close to resonance for a Lorentz model. Therefore, the small thickness of the sample does not guarantee a sub-wavelength propagation distance due to the possibly large values of the permittivity and the permeability (and hence the effective wavelength inside the medium is small). A robust method for achieving the right branch number has yet been proposed in (81) . Commonly when the number of layer in the propagation direction consist of few elements in order to avoid ambiguities in selecting a phase-adjusting integer l in Eq. (2.9) one should start the restoration of n' from a higher wavelength (far away from resonances) and obtain physically sound values of n' . Then, the wavelength should be moved toward shorter values while simultaneously adjusting the values of l in Eq. (2.9) to obtain a continuous behavior for n'.

30

2.2 S-parameters

Scattering parameters (or S-parameters) are complex-valued, frequency dependent matrices describing the transmission and reflection of electromagnetic energy measured at different ports of devices like filters, antennas, waveguide transitions, and transmission lines. The use of *S*-parameter is common in electromagnetic simulation when one deals with a fundamental propagation mode which can be used to excite a port with a known analytic profile. For homogeneous slab with small features and small periodicity respect to the operative wavelength, the eigen-value associated to the fundamental mode is an incident plane wave with incident power conventionally normalized to one. *S*-parameters originate from transmission-line theory and are defined in terms of transmitted and reflected voltage waves. For high-frequency problems, voltage is not a well-defined entity, and it is necessary to define the scattering parameters in terms of *T*-matrix. For homogeneous or symmetric homogeneous slab it can be shown (82) that the S matrix is symmetric with:

$$S_{21} = S_{12} = \frac{1}{T_s + \frac{1}{2}\left(iT_{12} - iT_{21}\right)}$$

(2.12)

$$S_{11} = S_{22} = \frac{-i\frac{1}{2}\left(T_{21} + T_{12}\right)}{T_s + \frac{1}{2}\left(iT_{12} - iT_{21}\right)},$$

where $T_s = T_{11} = T_{22}$. Using the analytic expression for the *T*-matrix elements in Eq.(2.4) gives the *S*-parameters

$$S_{21} = S_{12} = \frac{1}{\cos\left(nkd\right) - \frac{i}{2}\left(Z + \frac{1}{Z}\right)\sin\left(nkd\right)}$$

(2.13)

and

$$S_{11} = S_{22} = \frac{i}{2}\left(\frac{1}{Z} - Z\right)\sin\left(nkd\right)$$

(2.14)

Equations (2.13) and (2.14) can be inverted to find n and Z in terms of the S-parameters as follows:

$$N = \cos^{-1}\left[\frac{1}{2S_{21}}\left(1 - S_{11}^2 + S_{21}^2\right)\right], \tag{2.15}$$

$$Z = \sqrt{\frac{\left(1 + S_{11}\right)^2 - S_{21}^2}{\left(1 - S_{11}\right)^2 + S_{21}^2}} \tag{2.16}$$

The computation of the reflection and transmission coefficients in Eqs. (2.7)–(2.8) as well as the computation of the S-parameters ins Eqs. (2.15), (2.16) requires the knowledge of the scattered electromagnetic fields. Various numerical algorithms are available toward this end, some of the most common ones being the Finite-Difference Time-Domain Method (FDTD), Finite Element Method (FEM), the Transfer Matrix Method, or an integral equation method such as the Method of Moments. The first three methods have the appeal of an extreme generality and mathematical simplicity: they have been applied for many years to solve a plethora of electromagnetic problems, and are well documented in various references. Among this methods I'm aware only with FEM and all the simulation have been performed by using the commercial FEM software COMSOL Multyphysics @ (86). More detailed treatments can be found elsewhere (87) , (88), (89). Eqs. (2.15), (2.16) are formally similar to Eq. (2.7), (2.8) respectively and the same considerations about the determination of the integer l must be careful token in mind. Moreover it's important to stress that operatively the S-parameters are defined at two boundaries at fixed distances (d=0 and d=d$_1$+d+d$_2$ respectively in our example) from the slab interfaces. For this reason it's necessary to de-embed the homogeneous slab from the cladding and substrate domains by multiplying the S-parameters with constant phases (83):

$$S_{11} = S_{22} = re^{i2k_0 d_1} = R = \sqrt{\left|\mathbf{P}_{tot}\right|}\Big|_{z=0}\, e^{\left[i\arg\left((\mathbf{E}_{tot} - \mathbf{E}_{inc})/\mathbf{E}_{in}\right)|_{z=0}\right]} e^{i2k_0 d_1} \tag{2.17}$$

and

$$S_{21} = S_{12} = te^{ik_0(d_1 + d_2)} = Te^{ik_0(d_1 + d + d_2)} = \sqrt{\left|\mathbf{P}_{tot}\right|}\Big|_{z=d_2}\, e^{i\arg\left[(\mathbf{E}_{out})|_{z=d_2}\right]} e^{ik_0(d_1 + d_d)}, \tag{2.18}$$

Where $\mathbf{E}_{out}$ is the electric field and $\mathbf{P}_{tot}$ is the power flow calculated at the two outer boundaries. The practical implementation of these equations for the retrieval of the index of refraction and the impedance is hindered by a few issues that need to be carefully examined :

1. The practical limitation of Eqs. (2.11)
2. The sensitivity of these parameters to noise
3. The definition of the material boundaries.

1. both numerical simulations and experimental measurements introduce perturbations in the S parameters that translate into perturbations on n and Z. These perturbations are typically small and can be filtered out unless the parameters themselves are close to zero, in which case a small perturbation can induce an unphysical sign change. This issue can be resolved by introducing a threshold in the use of Eqs. (2.11): when the absolute value of Z is greater than the threshold, Eq. (2.11) can be used. Otherwise, the sign of Z is determined such that the corresponding index of refraction has a non-negative imaginary part. This condition is equivalent to $\left| e^{ink_0d} \right| \leq 1$, where

$$e^{ink_0d} = \frac{S_{21}}{1 - S_{11} \dfrac{Z-1}{Z+1}} \tag{2.19}$$

2. When the transmission is either close to zero or close to unity. In the first case, which typically appears below the resonance band, S_{21} is close to zero which yields large values in Eq. (2.15) and hence, strong variations in the index of refraction (seen as unphysical spikes in the retrieved values). This situation is avoided by solving first for the impedance. The latter is indeed stable as can be seen by inspecting the first derivative

$$\frac{\partial Z^2}{\partial S_{21}} = \frac{8 S_{21} S_{11}}{\left[\left(1 - S_{11}\right)^2 - S_{21}^2 \right]} \tag{2.20}$$

33

The second situation is the mirror of this first one: the impedance is unstable, whereas the index of refraction is stable and should be used first in the retrieval process. Eqs. (2.17),(2.18) can then be solved within a threshold.

3. The purpose of the homogenization procedure is to find the effective parameters of metamaterials, but also to find the boundaries of the effective medium. The metamaterials being usually composed of discrete metallic elements, it is not immediately clear where these boundaries should be. The determination of the boundaries can be performed based on the requirement of homogenization, namely that the effective parameters of two slabs of different thicknesses should be identical at all frequencies. This principle, along with the fact that the impedance depends on the slab thickness, can be used to set up a minimization problem: the impedances of two different metamaterial slabs are computed, and their difference is optimized across the entire frequency spectrum of interest as function of the boundaries of the medium. The boundaries that reach the minimum in a pre-defined sense are chosen to be the boundaries of the effective medium. In the case of periodic structures, this method yields the expected results that the effective boundaries coincide with the boundaries of the unit cell of the metamaterial (81).

2.3   Retrieval method in presence of one or two substrate.

The retrieval method discussed thus far contains most of the essential physics for extracting effective parameters from the amplitudes and phases of the waves transmitted and reflected from a metamaterial slab. However, this technique is not immediately applicable to most optical metamaterials, because the procedure is based on the assumption that the metamaterial is in the form of a free-standing slab surrounded by a vacuum. In almost all reported metamaterials for the optical frequency, substrate layers are involved, and therefore the metamaterial slabs are embedded in an asymmetric environment. In the most usual case one side of the metamaterial slab is immediately attached to a microscopically thick substrate (usually glass) and the other side interfaces air or vacuum. The *NIM*-air interface coefficients $t_{E,1}$

and $t_{H,1}$ are still defined by Eq.(2.6) but the coefficients at the *NIM*-substrate interface are given by $t_{E,2}=t$ and $t_{H,2}=n_2 t$ and

$$N = \cos^{-1}\left[\frac{1 - r^2 + n_2 t^2}{\left(n_2 + 1\right)t + rt\left(n_2 - 1\right)}\right], \tag{2.21}$$

where t is calculated (measured) in the substrate $t = S_{21}e^{-ik_0(n_2 d_2 + d_1)}$, $r = S_{11}e^{-i2k_0 d_1}$ and $n_2 \equiv n_{Glass}$.

Coefficients $t_{E,1}$ and $t_{H,1}$ at the *NIM*-air interface of a *NIM* layer on an ITO-glass substrate are also defined by Eq.(2.6), but back side coefficients should be first calculated (measured) in the substrate at the ITO-glass interface ($t_{E,3}=t$ and $t_{H,3}=n_3 t$) and then back-propagated using Eq. (2.4),

$$\tag{2.22}$$

$$\begin{pmatrix} t_{E,2} \\ t_{H,2} \end{pmatrix} = T_2 \begin{pmatrix} t \\ n_3 t \end{pmatrix}, \tag{2.23}$$

where

$$T_2 = \begin{pmatrix} \cos\left(n_2 kd\right) & -in_2^{-1}\sin\left(n_2 kd\right) \\ -in_2\sin\left(n_2 kd\right) & \cos\left(n_2 kd\right) \end{pmatrix} \tag{2.24}$$

with $n_2 \equiv n_{ITO}$, $n_3 \equiv n_{Glass}$. After some algebra the effective parameters are the fellow:

$$N = \cos^{-1}\left(\left(1 - r^2 + t^2\left(\left(\frac{i}{2}\right)\sin\left(2n_2 d_2 k_0\right)\left(n_2 + n_3\,/\,n_2\right) + n_2\cos\left(2n_2 d_2 k_0\right)\right)\right)\right)/$$

$$\left(t\begin{bmatrix} \cos\left(n_2 d_2 k_0\right)\left(1 + n_2\right) + i\sin\left(n_2 d_2 k_0\right)\left(n_2 + n_3\,/\,n_2\right) \\ +r\left(\cos\left(n_2 d_2 k_0\right)\left(n_3 - 1\right) + i\sin\left(n_2 d_2 k_0\right)\left(n_2 - n_3\,/\,n_2\right)\right) \end{bmatrix}\right),$$

$$\tag{2.25}$$

and

$$Z = \frac{\sqrt{\left((1 + r)^2 - t^2\left(\cos(n_2 d_2 k_0) + i(n_3\,/\,n_2)\sin(n_2 d_2 k_0)\right)^2\right)}}{\sqrt{\left((1 - r)^2 - t^2\left(n_3\cos(n_2 d_2 k_0) + in_2\sin(n_2 d_2 k_0)\right)^2\right)}}, \tag{2.26}$$

with $t = S_{21}e^{-ik_0(d_1+n_3d_3)}$, $r = S_{11}e^{-i2k_0d_1}$ and d_3 is the glass layer thickness under ITO.

2.4   S-parameters in presence of bi-anisotropy medium.

A common method to retrieve the effective constitutive parameters is based on the complex transmission and reflection coefficients (S-parameters). The standard retrieval method discussed in the last sessions assumes isotropic constitutive parameters (ϵ, μ) for a symmetric structure (82). However, this fails if the unit cell of the NIM is not symmetric in the propagation direction. The asymmetry can causes the electrical field in one specific direction to induce a magnetic dipole in the orthogonal direction while the magnetic field can also induce an electrical dipole in its orthogonal direction. By assuming that the medium is reciprocal (90) and that the harmonic time dependence is $e^{-i\omega t}$, one can write the constitutive relationships as

$$\begin{aligned} \mathbf{D} &= \overline{\overline{\varepsilon}}\mathbf{E} + \overline{\overline{\xi}}\mathbf{H} \\ \mathbf{B} &= \overline{\overline{\mu}}\mathbf{H} + \overline{\overline{\zeta}}\mathbf{E} \end{aligned}, \tag{2.27}$$

where

$$\overline{\overline{\varepsilon}} = \varepsilon_0 \begin{pmatrix} \varepsilon_x & 0 & 0 \\ 0 & \varepsilon_y & 0 \\ 0 & 0 & \varepsilon_z \end{pmatrix}, \qquad \overline{\overline{\mu}} = \begin{pmatrix} \mu_x & 0 & 0 \\ 0 & \mu_y & 0 \\ 0 & 0 & \mu_z \end{pmatrix},$$

$$\overline{\overline{\xi}} = \frac{1}{c}\begin{pmatrix} 0 & 0 & 0 \\ 0 & 0 & 0 \\ 0 & -i\xi_0 & 0 \end{pmatrix}, \qquad \overline{\overline{\zeta}} = \frac{1}{c}\begin{pmatrix} 0 & 0 & 0 \\ 0 & 0 & i\xi_0 \\ 0 & 0 & 0 \end{pmatrix}. \tag{2.28}$$

The seven unknowns ϵ_x, ϵ_y, ϵ_z, μ_x, μ_y, μ_z, and ξ_0 are quantities without dimensions. If , for instance, a plane wave that is polarized in the x-direction is incident in the z-direction, three parameters ϵ_x, μ_y, and ξ_0 will be active, while the other four parameters, ϵ_y, ϵ_z, μ_x and μ_z will not be involved in the bianisotropic process and, therefore, are out

of the scope of the study. Compared to an isotropic material, the most interesting and important feature of a bianisotropic material is that the characteristic impedances have different values for the waves propagating in the two opposite directions of the z-axis. For an electromagnetic wave traveling in the z-direction, the impedances will be

$$z^+ = \frac{\mu_y}{n + i\xi_0}, \quad z^- = \frac{\mu_y}{n - i\xi_0}, \tag{2.29}$$

respectively. Here n is the effective refractive index (n_{eff}), which has the same value for the EM wave traveling in the two opposite directions on the z-axis,

$$n = \pm\sqrt{\varepsilon_x \mu_y - \xi_0^2} \tag{2.30}$$

There are two different situations to be considered, i.e., incidence in the $+z$- and $-z$- directions. After applying the boundary continuous conditions, it is easy to obtain the expressions for the S-parameters by using the transfer matrix method (90),(82). When the incidence is in the $+z$-direction (see Figure 2-1 in which the homogeneous slab is now to be considered as a bianisotropy medium) the corresponding reflection (S_{11}) and transmission (S_{21}) coefficients are (84),(85)

$$S_{11} = \frac{2i\sin(nk_0 d)\left[n^2 + (\xi_0 + i\mu_y)^2 \right]}{\left[(\mu_y + n)^2 + \xi_0^2 \right]e^{-ink_0 d} - \left[(\mu_y - n)^2 + \xi_0^2 \right]e^{ink_0 d}},$$

$$S_{21} = \frac{4\mu_y n}{\left[(\mu_y + n)^2 + \xi_0^2 \right]e^{-ink_0 d} - \left[(\mu_y - n)^2 + \xi_0^2 \right]e^{ink_0 d}}, \tag{2.31}$$

while the case when the incidence is in the $-z$-direction, we obtain the corresponding reflection (S_{22}) and transmission (S_{12}) coefficients as

$$S_{22} = \frac{2i\sin(nk_0 d)\left[n^2 + (\xi_0 - i\mu_y)^2 \right]}{\left[(\mu_y + n)^2 + \xi_0^2 \right]e^{-ink_0 d} - \left[(\mu_y - n)^2 - \xi_0^2 \right]e^{ink_0 d}},$$

$$S_{12} = S_{21} = \frac{4\mu_y n}{\left[(\mu_y + n)^2 + \xi_0^2 \right]e^{-ink_0 d} - \left[(\mu_y - n)^2 + \xi_0^2 \right]e^{ink_0 d}}, \tag{2.32}$$

After some trivial treatment, the analytical expression for the refractive index n is obtained,

$$\cos(nk_0 d) = \frac{1 - S_{11}S_{22} + S_{21}^2}{2S_{21}} = \cos(N) \tag{2.33}$$

Obviously, when (S_{11}) is equal to (S_{22}), Eq. (2.33) will degenerate into a standard retrieval Eq. (2.15). Eq. (2.33) shows that an effective index can be recovered from a modified S-parameter retrieval procedure that utilizes all elements of the S-matrix. A comparison of Eq. (2.33) with Eq. (2.15) shows that the standard retrieval procedure can be applied to find the index for an inhomogeneous structure using an averaged S_{av} of

$$S_{AV} = \sqrt{S_{11}S_{22}} \tag{2.34}$$

Note that the retrieval procedures for both homogeneous and symmetric inhomogeneous unit cells are identical, since $S_{11}=S_{22}$.

Again when solving for n from Eq. (2.33), one must determine one branch from many branches of solutions as just discussion in the last session Therefore, it will not be detailed here again. For a passive medium, the solved n must obey the condition

$$n'' \geq 0. \tag{3.35}$$

After n is obtained, other constitutive parameters can be obtained easily (84)

$$\xi_0 = \left(\frac{n}{-2\sin(nkd)} \right)\left(\frac{S_{11} - S_{22}}{S_{21}} \right),$$

$$\mu_y = \left(\frac{in}{\sin(nkd)} \right)\left(\frac{2 + S_{11} + S_{22}}{2S_{21}} - \cos(nkd) \right), \qquad (2.36)$$

$$\varepsilon_z = \frac{(n^2 + \xi_0^2)}{\mu_y}.$$

Consequently, the impedances $\mathrm{Re}(z^+)$ and $\mathrm{Re}(z^-)$ can be obtained from Eq. (2.29). Again, for a passive medium, the following conditions should be satisfied:

$$\mathrm{Re}(z^+) \geq 0, \quad \mathrm{Re}(z^-) \geq 0. \qquad (2.37)$$

2.5 Conclusion

Using port for solving the scattering problem is a very common approach because it offers a straightforward implementation: each port is associated with a fundamental mode and automatically generates the related S-parameters. However there are two situation in which one has to be more careful and the port implementation fails.

1. When the direction of the incident wave is not perpendicular to the homogeneous slab.
2. When the substrate dielectric constant is so great that the effective wavelength is reduced and the scattering is no longer dominated by the fundamental mode, thus invalidating hypothesis of effective response by metamaterial.

1. In case of incident wave not perpendicular to the slab it's not easy to excite the right mode on both ports, in particular the polarization state of the transmitted wave is not known *a priori.* In this case it's possible to abandon the port implementation in favor of the *scattering formulation* (87). The scattering formulation in FEM is a common approach for the solution of the EM waves scattering problem when the scattering object has smaller dimension than the incident wavelength. The scattering field is calculated as the difference between the total and the incident field. The incident field is the back-ground field which can be calculated analytically (for the most simple cases) or numerically from simulation. In the simulations considered in the next chapters the back-ground field is a free plane wave in air or propagating in *air+glass* domains. The scattered field is calculated from the initial analytical back-ground field expression and it is absorbed by Perfectly Matched Layers which truncate the mesh under and above the computational cell. Once the incident field profile is set together with the absorbing condition and the lateral boundary condition (Floquet-periodic condition for oblique incidence (87)) the total field is computed automatically by COMSOL.

2. When the index of dielectric in the substrate is quite high so that Bragg-scattering becomes more efficient and several orders can be produced causing the two-port implementation to be un-correct. In this case the right way to proceed (at least when the incident field is perpendicular to the slab and there are no uncertainties on the transmitted polarization generated by the effective refractive index) is to set more than one port in the input and output domain in order to absorb all the diffracted orders and capture the fundamental one associated with the effective medium. Fortunately the typical experimental set up consist in metamaterials upon a thick substrate of glass or glass+ITO with moderately small index of refraction ($\sim 1.5, 1.7$ respectively). Than for this configuration the homogenization condition holds well for large wavelength thus allowing the calculation by means of Eqs. (2.21), (2.25).

3 Fishnet metamaterial

The refractive index $n = n' + n''$ is the key parameter in the interaction of light with matter. Normally n' has been considered to be positive, but the condition $n' < 0$ does not violate any fundamental physical law (1). Negative index metamaterials (*NIMs*) with $n' < 0$ have some remarkable properties. The refractive index is expressed in terms of the real and imaginary parts of the permittivity and permeability as

$$n = n' + in'' = \sqrt{(\varepsilon'\mu' - \varepsilon''\mu'') + i(\varepsilon'\mu'' + \varepsilon''\mu')}, \qquad (3.1)$$

where $\varepsilon = \varepsilon' + \varepsilon''$ and $\mu = \mu' + \mu''$. To achieve a negative n', the imaginary part inside the square root needs to be < 0, which can be satisfied for a sufficiently large imaginary term without requiring both ε' and μ' to be negative. Typically, a *NIM* is an artificially engineered metal-dielectric composite that exhibits $n' < 0$ within a particular wavelength range. From Eq. (3.1) this can be accomplished either through the strong (sufficient) condition that $\mu < 0$ and $\varepsilon < 0$, or through a more general (necessary and sufficient) condition $\varepsilon'\mu'' + \mu'\varepsilon'' < 0$. The latter strictly implies that there cannot be $n' < 0$ in a passive metamaterial with $\mu = 1 + 0i$. Following the above discussion, two types of *NIMs* can be introduced. A double-negative *NIM* (*DNNIM*) is a material with simultaneously negative real parts of effective permeability and permittivity ($\varepsilon' < 0$ and $\mu' < 0$). A single-negative *NIM* (*SNNIM*) has a negative refractive index with either ε' or μ' (but not both) being negative. At optical wavelengths, obtaining $\varepsilon' < 0$ is easy compared to $\mu' < 0$, since noble metals naturally have a negative permittivity. The ratio $-n'/n''$ is often taken as a figure of merit (*FOM*) of *NIMs*, since low-loss *NIMs* are desired. The *FOM* can be rewritten as $-(|\mu|\varepsilon' + |\varepsilon|\mu')/(|\mu|\varepsilon'' + |\varepsilon|\mu'')$ indicating that a *DNNIM* with $\varepsilon' < 0$ and $\mu' < 0$ is better than a *SNNIM* with the same $n' < 0$, but with $\mu' > 0$. In other words, a

DNNIM will have a lower n'' when compared with a *SNNIM* with the same value for n'; in addition, *DNNIMs* can provide better impedance matching as compared to *SNNIMs*.

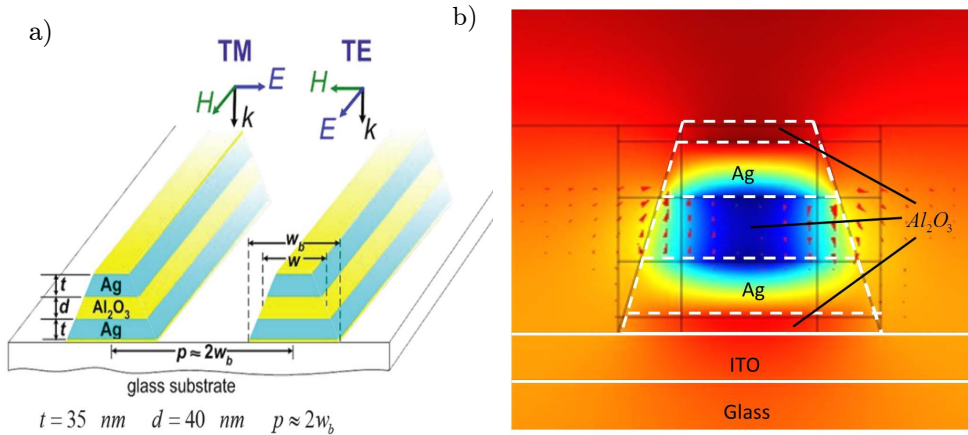## 3.1   Single negative μ metamaterial

Figure 3-1.a) Structure of the coupled nano-strip samples. b) Simulation of magnetic field (color in a.b) and electric field (arrow) at the magnetic resonance. (the black lines track the structure boundaries and are guides for eyes)

In Figure 3-1 is shown a periodic array of pairs of thin silver strips. The structure has just experimentally proved to possess a negative permeability (with positive refractive index) in the visible spectrum thus behaving like a *SNM* (91), (92). The period is d=2w=300nm while the Silver and dielectric (alumina with n=1.63) layer size are t=35nm and d= 40nm respectively. The silver permittivity was extracted from a Drude-Lorentz   model: $\varepsilon_{Ag} = 1 - w_p^2 / (w^2 - iw\gamma)$ with $\omega_p = 1.37 \times 10^{16}$ and $\gamma = 2.6 \times 10^{13}$. The entire   structure is simulated on glass+ 15nm of ITO layer.   In addition, two thin 10-nm layers of alumina are added, one between the lower silver strip and the substrate and the second on top of the structure. Both additional alumina layers appear to be necessary for the stable fabrication of samples. In the resonant

(TM) polarization the magnetic field is aligned with the largest dimension , the infinite length of the strips. Only one component of the magnetic field should ideally be present in this case. In the non-resonant (TE) polarization the single component of the electric field is aligned with the strip length, giving no resonant effects. In such an ideal sub-wavelength grating of Figure 3-1a, a relatively wide negative magnetic response exists in the TM regime and it extends from a wavelength of 675 nm to 770 nm, as shown in Figure 3-2.

a)

b)
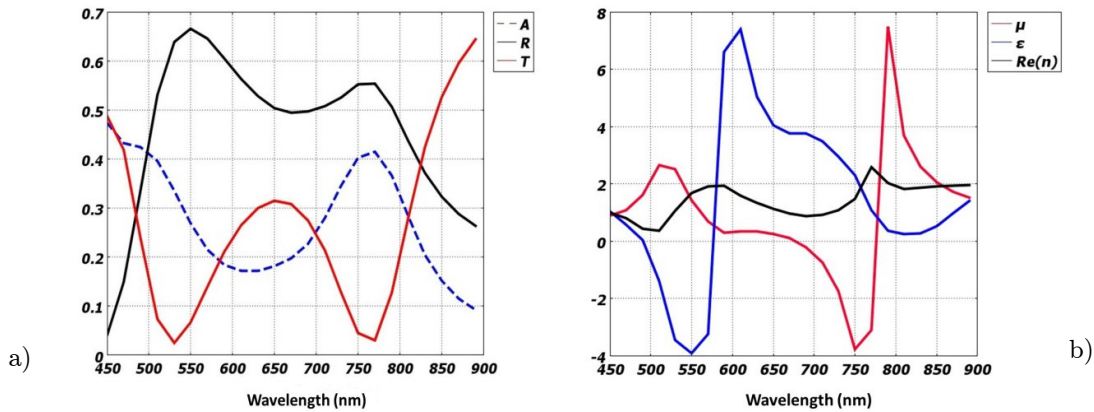
Figure 3-2. Effective parameters extracted from the unite cell simulation of Figure 3-1: a)Reflectance, absorbance and transmittance; b) permeability, permittivity and refractive index.

In Figure 3-2b the permittivity around the electric resonance (near 570nm) in the TM configuration appears in the form of Lorentz-Drude. The resonant frequency is dipol-like and it is due to the finite boundaries of the structure along the polarization direction of the electric field. As reported in (93) this kind of resonance leads to a upper edge $\left(\lambda_{res} \neq 0 \right)$ due to the finite extent of the wires and this turns in a strong reduction or disappearance of the negative refractive index regime.

3.2   A *DNNIM* in the optical spectral range: the Fishnet metamaterial.

The Fishnet can be seen as the combination of two metamaterials, like shown in Figure 3-3. On the left, magnetic field induced by circular oscillating currents counteract with the incident TM magnetic field thus generating a negative permeability. In the middle the electric field enables charge oscillation in the metal thus producing a negative permittivity in TE configuration. This is a typical behavior for the most common metal like Gold, Silver, Chrome etc… Both the TM and TE nano-strip generally are not able to produce negative refractive index. However by composing both in a 'fish-net' like structure as shown on the right we sum the effect of negative permeability and negative permittivity in one only structure. The overlap of negative permittivity and negative permeability produces a negative index of refraction and it can be set in several frequency ranges by only operating on the geometric features of the structure.
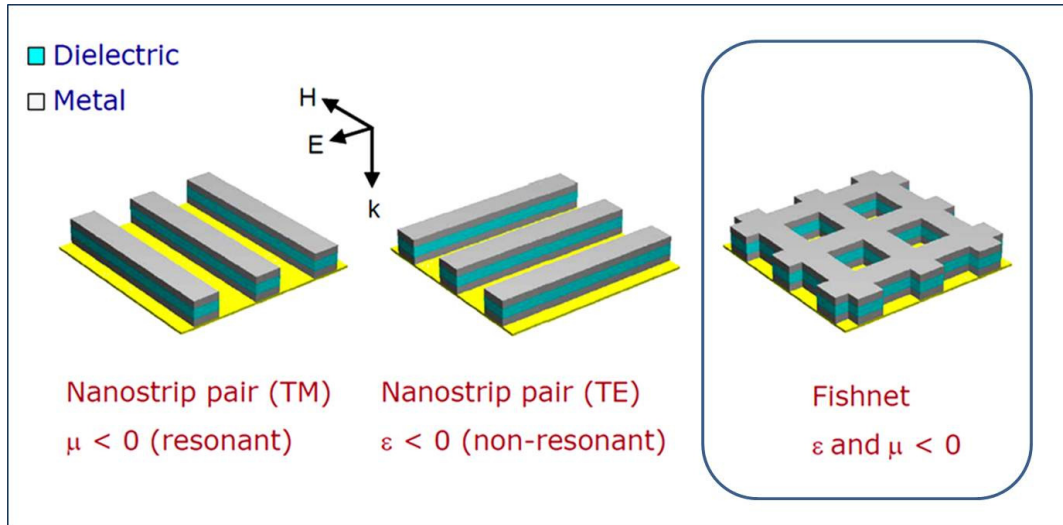

Figure 3-3. Geometric examples of a) nano-strip pair in TM polarization, b) nano-strip pair in TE polarization and c) Fishnet metamaterial

The standard Fishnet structure is a combination of double-strip (or cut slab) pairs and long connected wires, as shown in Figure 3-3. Their combination and sizes can be accomplished in various geometric features: squared, circular, elliptical holes or isotropic Fishnet (94), (95). For our purposes we have simulated and analyzed a

Fishnet with squared holes. The structure is illuminated at normal incident with the long wires along the electric fields. All the geometric features are illustrated in Figure 3-4. The thickness of the metal (Au) layers and the dielectric (Al$_2$O$_3$) layer are fixed to t=30 nm and h=40 nm respectively and a_z=2t+h is the total Fishnet thickness in the longitudinal (parallel to $\boldsymbol{k}$) direction. We chose D=150 nm and W= 120 nm as the major and minor size of the squared holes respectively and P=300 nm is the lattice parameter in the lateral directions. Alumina (Al$_2$O$_3$) with index of refraction n=1.63 has been chosen for its low losses in the terahertz range. For the extraction of the S-Parameters and the verification of our design, parametric simulations were done with the commercial Comsol Multiphysics ® software, employing the Finite Element Method (FEM) for finding approximate solutions of Maxwell's equations. The Fishnet has been regarded theoretically as an artificial waveguide surrounded by air, with two perfect magnetic conductor planes normal to the incident magnetic fields and two perfect electric conductor planes normal to the incident electric fields. Two ports under and above the unite cell Fishnet have been added for the evaluation of the S-Parameters of the wave-guide. In this way the structure is equivalent to a periodic infinite tri-layer medium (homogeneous for the operative wavelengths over 400 nm) with a polarized normal incident wave. Drude model extracted from experimental data for metallic bulk has been used to describe the electron plasma behavior at the surface of Gold (96), (97).The value of plasma frequency (ω_p) and collision frequency (γ) are 2175 THz and 6.5 THz respectively. These values are guaranteed to fit the experimental data over a frequency range from 30 to 900 THz (96),(97). The effective parameters, permittivity, permeability and refraction index are retrieved according to the traditional method (81),(82) by inverting the simulated S-Parameters, under the assumption that the metamaterial can be treated as homogenous. For most of the potential applications of metamaterials, like super-lensing resolution, waves propagate at non zero angle of incidence with respect to the plane perpendicular to the boundary of the structure ($\boldsymbol{E}$-$\boldsymbol{k}$ plane). So we recalculated the transmission data of our Fishnet for different angles of incidence in TE configuration (only a part of the magnetic incident field is oriented

parallel to the *z*-axis) and using circular holes of ray *r*=76nm. In Figure 3-4 we see that the spectral position and shape of the observed transmission band in the magnetic resonant regime varies slightly with the angle of incidence although the magnetic coupling decrease with larger angles of incidence ($\vartheta > 40°$).
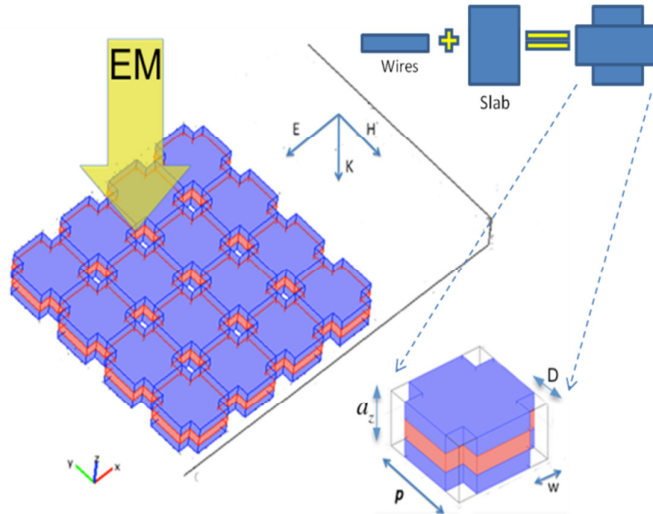

Figure 3-4. Unit cell of the Fishnet with parameters indicated: The lattice constant along x-y direction P=300 nm, the metal (Au) thickness t=30 nm, the dielectric (Al$_2$O$_3$) thickness h=40 nm and the widths of the rectangular holes respectively D=75 nm and W=60 nm. The electromagnetic field is incident along the z direction, with the electric and magnetic fields in the x and y direction respectively.

3.3   The effective Fishnet parameters

In Figure 3-5 we show the effective parameters extracted from the simulation. Two dips in the reflectance (and two corresponding maxima in the transmittance) spectrum are clearly visible. They are evident manifestation of two resonances at 600nm and 830nm. The two dips in the reflectance correspond to the two local minima of permeability: μ=-0.46 at 599 nm and μ=-1.52 at 834 nm. Two left handed *LH* bands of negative index are foreseen in the two regions: from 595nm to 600nm and from 810nm to 840nm where the real part of permeability and permittivity overlaps giving rise to a negative refractive index.
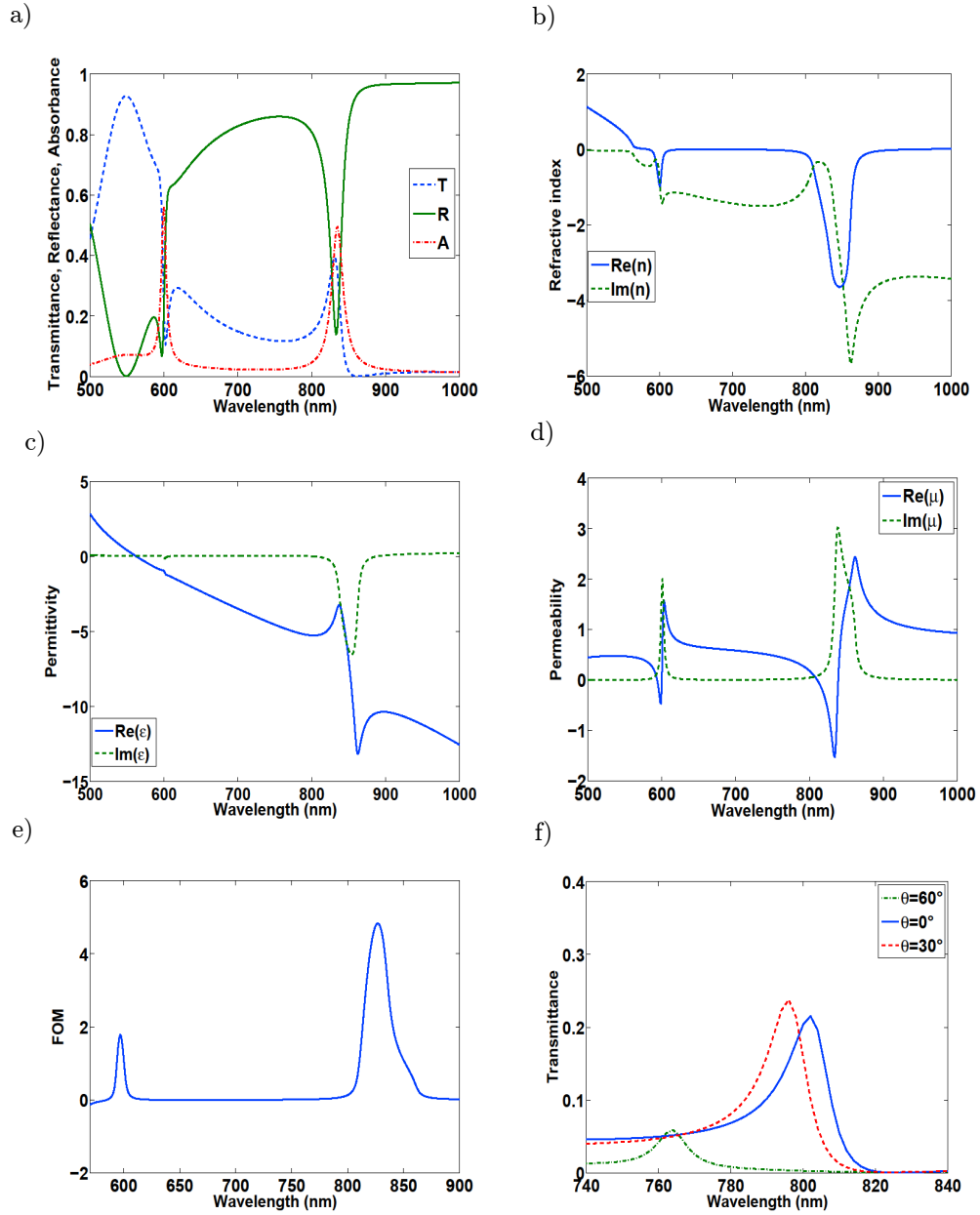
Figure 3-5. Effective retrieved parameters: transmittance (blue dashed line), reflectance (green solid line), absorbance (red solid dotted line) (a); index or refraction n with real part (blue solid line) and imaginary part (green dashed line) (b); permittivity ε with real part (blue solid line) and imaginary part (green dashed line) (c); permeability with real part (blue solid line) and imaginary part (green dashed line) (d);FOM definited by $-\mathrm{Re}(n)/\mathrm{Im}(n)$; Magnetic coupling with different angles of incidence using circular holes with r=76nm

3.4   The Fishnet modes (an overview)

The nature of this resonances is quite different. Christ et al (98) and more recently J.Parson at al (99), have investigated the nature of these modes. They are related to the hybridization of *LSPRs* (Localized Surface Plasmon Resonance). The absorbance maxima in the hole-array structure is attribute to the coupling of the incident radiation to *LRSP* modes associated with the charge distribution induced in the vicinity of the nano-holes. As long as the dielectric separation is not too large (about few tens of nanometers), we expect two modes to be possible: an electric symmetric and a magnetic anti-symmetric mode. Symmetric and anti-symmetric refers to the orientation of currents along the two metal-dielectric interfaces. In Figure 3-6 we show simulations mapping the electric and the magnetic fields in the unit cell around the hole. In Figure 3-6b two opposite currents are visible inside the hole volume at frequency of 834nm.

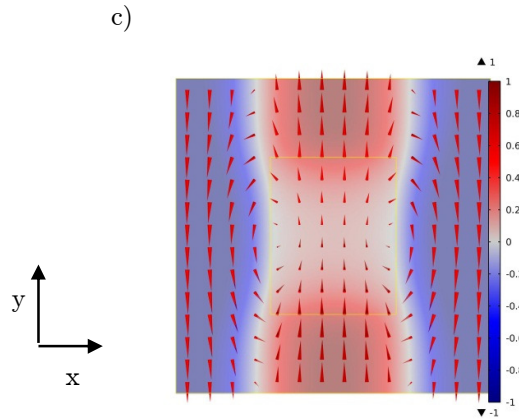a)   b)

c)
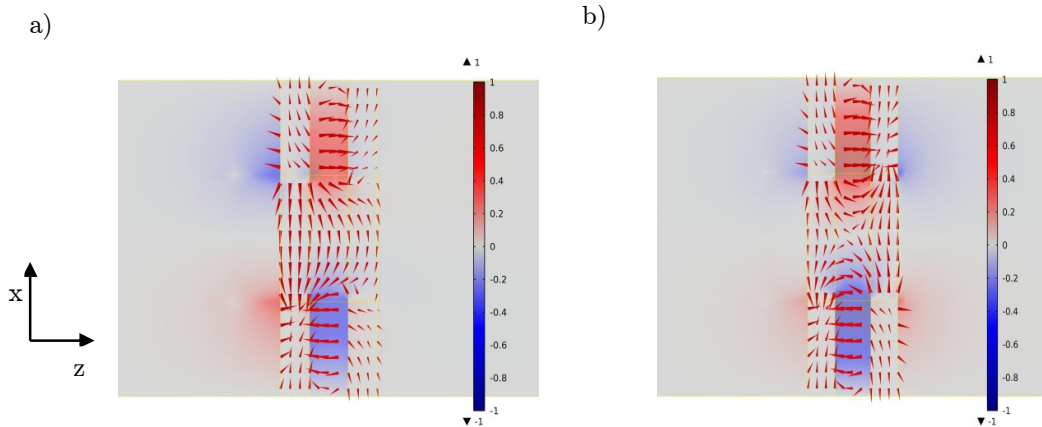
Figure 3-6 Maps of electric and magnetic fields: Electric field components at the electric resonance and the z component (contour plot) (a); electric field components (arrows) at magnetic resonance and the z component (contour plot) (b); magnetic field components at the magnetic resonance (arrows) and the y component (contour plot) (c); For the 3 cases the unit cell has been centered around the hole and the observation planes have been fixed at P/2 in the y direction (a,b) and az/2 in the z direction (c) respectively.

The π-phase change in the incident electric field is not possible over a distance less than one wavelength (which in turn enforces the homogeneity condition). Instead, the excitation of the anti-ymmetric mode occurs through the incident time-varying magnetic field which induces currents in both the upper and lower layers being in anti-phase. For this reason this kind of resonance is referred to as a magnetic resonance. In Figure 3-6b is also shown the z-component of the electric fields. Two effective magnetic capacitance are generated by the magnetic resonance as it appears from the arrows of the electric field in the z-direction. In Figure 3-6c are also shown the magnetic fields components (arrow plot). The magnetic field components at the resonance have opposed direction between the neck and the slab. This is consequence of counteracting currents between the neck and the slab generated by opposite charges between the slabs (see the arrows in opposite directions between the neck and the slab). This produces two magnetic inductances in parallel. As a result a resonant magnetic LC circuit is induced by the charge distribution in the Fishnet metamaterial. Moreover from Figure 3-6a the current distribution around the hole appears symmetric at frequency of 598nm and its related resonance is mainly electric in nature. In this case the currents flow through the electric capacitance between two parallel wires of approximate length P and radius t without charge accumulation between the slab and

50

the neck of the opposite metallic sheet. Moreover two electric inductances related to the metallic neck and slabs respectively are induced and they can be described by effective straight-wire inductances. Again a resonant electric LC circuit is formed.
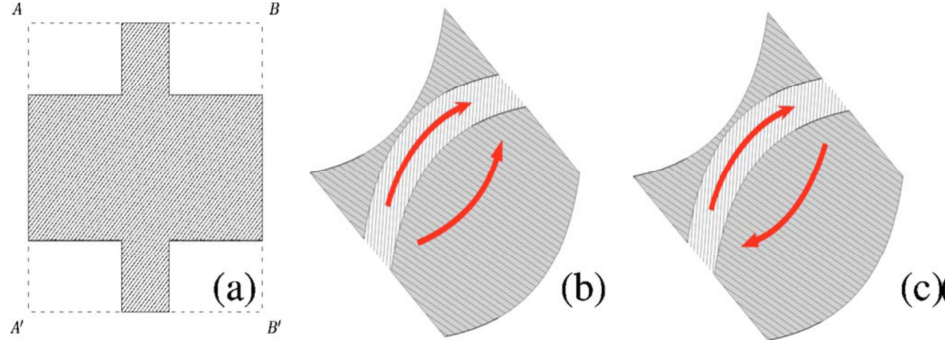

Figure 3-7. a)Schematics of one unit cell of the Fishnet design. Dashed lines show the boundaries of the unit cell. Due to the periodicity, the lines $A\ B$ and $A'B\ '$ are equivalent. Panels (b) and (c) are redrawings of the metallic sheet of panel (a) taking advantage of the periodicity, and drawing also the two possibilities for current flow: (b) topologically opposite direction current flow and (c) topologically same direction flow.

One way to think about this problem of current flowing in a Fishnet-like structure is to realize first that the line AB and the line $A'B'$ in Figure 3-7 are identical. This is so because the periodicity implies Bloch's theorem, stating that the solution $F(\mathbf{r})$ has the form

$$F(\mathbf{r}) = u(\mathbf{r})e^{i\mathbf{k}\cdot\mathbf{r}} \tag{3.2}$$

where $F(\mathbf{r})$ is any component of the EM field and the current, $u(\mathbf{r})$ is a periodic function of $\mathbf{r}$ in the x-y, and $\mathbf{k_r}{=}k_z$ since $\mathbf{k}$ is along the z-direction. Hence, $F(\mathbf{r})$ is a periodic function of x and y, and A and A' are equivalent. As a result, we can redraw the metallic sheets of the Fishnet design as in Figure 3-7 creating thus a closed loop consisting of two distinct elements: the slab and the neck. There are at least two distinct ways for current to flow in this two-component loop (100): either in opposite directions ´topologically´, as in Figure 3-7b or at the same direction, as in Figure 3-7c.

Both modes are admissible; the current distribution in the Fishnet is in general a superposition of (at least) these two current modes. The basic difference between the two modes is that the first one creates charge accumulation where the opposite currents in slab and neck meet, while the second is just a circular current without charge accumulation. The first mode is easily identified with the resonant oscillatory modes of the slab: the magnetic resonance which has opposite polarization of the corresponding slabs in the two sheets of a single Fishnet unit cell, and the electric short-wire response where the corresponding slabs are polarized in the same direction. Charge conservation enforces pairwise spatial charge accumulations with opposite sign, the capacitance of which constituted the back-driving force in the resonant oscillation. (For the magnetic resonance, this capacitance is predominantly between the sheets, while for the electric resonance, at higher frequency, between the ends of the slabs within a sheet). The second mode, as non-resonant (no charge accumulation, no capacitance) current, can be identified with the plasmonic electric response of the "continuous wires" constituted by the connection of slabs and necks. Those wires are simply polarized by the external electric field, which gives rise to a linear electric (polarization) current through slabs and necks in the same direction (and, moreover, in parallel in both sheets of the Fishnet layer). In the vicinity of the magnetic response of the Fishnet structure, these plasmonic currents are usually much weaker than those of the resonant mode.

Figure 3-8 Electric dipole induced by the current distribution.(a) Anti-symmetric current distribution, (b) symmetric current distribution

From Figure 3-5b we see that the magnetic resonance occurs at wavelength greater than the electric one. This derives from the current distribution. In the anti-symmetric

current case, they induce an electric dipole which counteracts the incident electric fields, reducing the resonance frequency (thus the resonant wavelength is up-shifted) (compare Figure 3-6b with Figure 3-8a). In the symmetric current case they generate an electric dipole aligned to the incident electric field thus enforcing the oscillation frequency (the resonance wavelength is down shifted) ,(compare Figure 3-6a with Figure 3-8b,(99)). This also explains why in Figure 3-3e the dissipation of magnetic mode is lower than the electric one (the first being weakly coupled to the incident radiation).

3.5   Electric and magnetic response of metamaterial Fishnet

To understand and explain the results presented in the previous section, we use the common approach of describing the artificial magnetic structures (at the resonant magnetic response regime) as equivalent effective RLC circuits (see Figure 3-9). Using circuit theory and basic electromagnetic considerations, (101) one can easily obtain an expression for the frequency dependence of the effective magnetic permeability, $\mu(\omega)$ for a lattice of artificial magnetic elements.
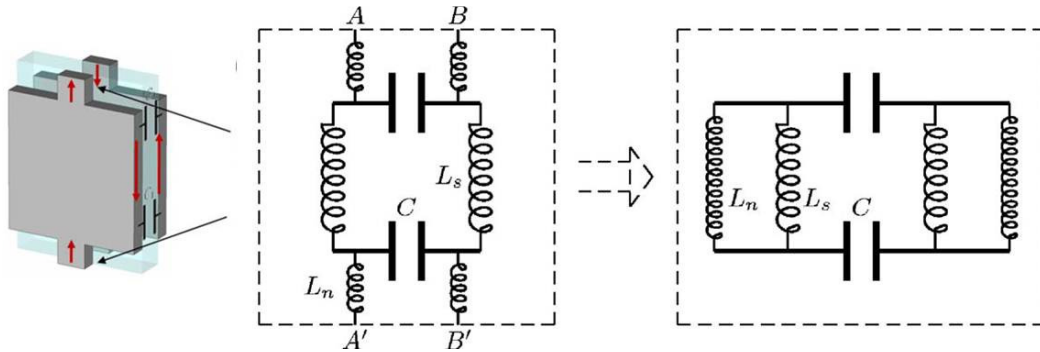

Figure 3-9 An LC circuit model for the Fishnet structure. L_s and L_n denote the loop inductances at the slabs and necks, respectively, and C the capacitance of the structure. The right panel results from left panel after taking into account the periodicity and thus the equivalence of the points A and A' and B and B'.

Assuming a Fishnet system like the one shown in Figure 3-9, of length l and slab separation h, excited by a magnetic field of the form $H = H_0 e^{-i\omega t}$ and direction as shown in Figure 3-3, and applying the Kirchhoff voltage rule, one can obtain

$$L\ddot{I} + \frac{1}{C}I + \dot{I}R = -\ddot{\phi} = \omega^2 \mu_0 lh H_0 e^{-i\omega t}. \tag{3.3}$$

ϕ is the external magnetic flux, $\phi = \mu_0 lh H_0 e^{-i\omega t}$, and R, C and $L \equiv L_{\text{Fishnet}}$ the resistance (frequency independent, accounting for ohmic losses in metal), the capacitance and the inductance of the system (the parallel of two inductances: the neck inductance L_{neck} and the slab inductance L_{slab}). The obvious solution of Eq.(3.3) is $I = I_0 e^{-i\omega t}$, with

$$I_0 = -\frac{\omega^2 \left[\mu_0 lh \,/\, L \right]}{\omega^2 - (1\,/\,L)C + i\omega R\,/\,L} H_0 \tag{3.4}$$

Having the current, one can easily obtain the pair magnetic dipole moment, $m = area \times current$,

$$m = I_{slabs} lh - I_{neks}(a_E - l)h = I_0 L_{fishnet} \left[\frac{lh}{L_{slabs}} - \frac{(a_E - l)h}{L_{necks}} \right], \tag{3.5}$$

where $I = I_{slabs} + I_{necks}$ and $I_0 L_{fishent} = I_{slabs} L_{slabs} = I_{necks} L_{necks}$ and the magnetization $M = (N_{LC}/V)\,m = (1/V_{UC})m$, N_{LC} is the number of RLC circuits in the volume V, and $V_{UC} = a_E a_H a_k$ is the volume per unit cell, where $a_H, a_E \,(= l)$ and a_k are the system lattice constants along the H, E, and k directions, respectively. Finally, using $M = \chi_m(\omega)H$, $\mu(\omega)\,/\,\mu_0 = 1 + \chi_m(\omega)$, with χ_m the magnetic susceptibility, one obtains

$$\mu(\omega) = \mu_0 \left\{ 1 - \frac{(1\,/\,V_{UC})\mu_0 a_E h\omega^2 \left[hl\,/\,L_{slabs} - (a_E - l)h\,/\,L_{necks} \right]}{\omega^2 - 1\,/\,L_{fishnet}C + i\omega R\,/\,L_{fishnet}} \right\} \tag{3.6}$$

.

From Eq. (3.6) one can see already that the presence of the necks weakens the magnetic response of the structure since the neck contribution in the magnetic moment opposes that of the slabs. This is clearly seen in Figure 3-6c where two opposite currents are generated between the slabs and the necks. Eq. (3.6) can be expressed as

$$\mu(\omega) = \mu_0 \left[1 - \frac{F\omega^2}{\omega^2 - \omega_{LC}^2 + i\omega\gamma} \right],$$

(3.7)

where $F = (1 / V_{UC})\mu_0 a_{\mathrm{E}} h \left[lh / L_{slabs} - (a_{\mathrm{E}} - l)h / L_{necks} \right]$.

From eq. 3.7 one derives that for achieving a strong magnetic resonance it's necessary to have:

- Metals of highest possible plasma frequency ω_p and the lowest possible collision frequency γ (Silver is the best choice)

- Thick separation layer between the slabs of the pair (i.e., high h but not as high though as to cancel the interaction between the slabs

- Structures of short neck width (i.e., short neck width to maximize both the neck inductance and F in Eq. 3.7 but not as short though as to strongly reduce the effective plasma, see next section)

In Figure 3-10 we fitted the effective permeability and permittivity of the Fishnet around the magnetic resonance. In this case $a_{\mathrm{H}} = a_{\mathrm{E}} = l$ and $a_{\mathrm{k}} = 2t + h$. We see that the permeability follows a Drude-Lorentz like model:

$$\mu = 1 - \frac{\lambda_m^2 f}{\lambda_m^2 - \lambda_o^2 - i\Gamma\lambda_0},$$

(3.8)

which reproduce the oscillation of fictitious magnetic charge around the magnetic resonance wavelength $\lambda_m = 830$nm and $\Gamma = \gamma\lambda_m^2 10^{-9} / c = 14.92$ is compatible with the fitted parameter value of 15.0. As we see form fig (2c) the permittivity around the

55

magnetic resonance shows an anti-resonance behavior. This has been amply discussed in (74) and is attributed to the periodicity of the lattice. We fitted with the following analytic model:

$$\varepsilon_{eff} = a - \frac{\dfrac{1}{\lambda_1^2} - \dfrac{1}{\lambda_2^2}}{\dfrac{1}{\lambda^2} - \dfrac{1}{\lambda_2^2} + i\dfrac{\Gamma}{\lambda 2\pi c}} - \frac{\dfrac{1}{\lambda_p^2}}{\dfrac{1}{\lambda^2} + i\dfrac{\Gamma}{\lambda 2\pi c}}$$

(3.9)

The second term is taken in analogy to the short-wire like electric responses and the third one is due to the metal electron oscillation in the continuous wire. The best fit leads to a=1, $\lambda_1 = 840nm$, $\lambda_2 = 880nm$, $\Gamma \approx \gamma$.
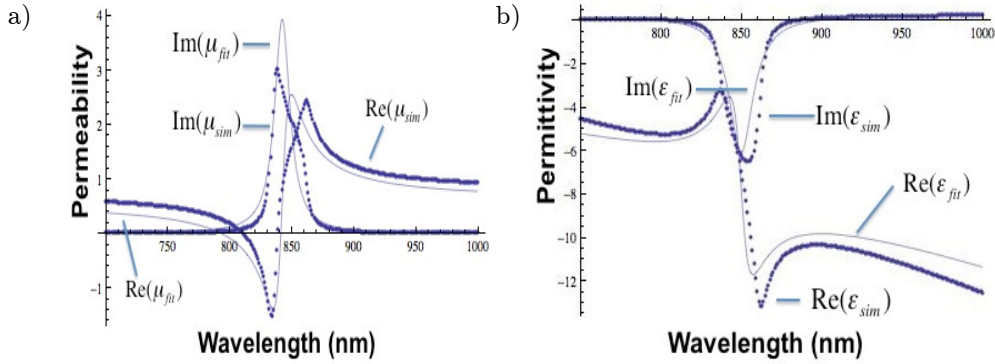
Figure 3-10. Fit to the magnetic permability and electric permitivity. Fit with a Drude-Lorentz like model (A); fit with a Drude-Lorentz like model plus Drude like model describing the free electron oscillation in the continuous wires (B)

3.6   Parametric analysis of Fishnet metamaterial

In the last session it has been showed that the Fishnet has an equivalent description in terms of LC circuit. It has been demonstrated (101), (102), (103), (104), (105) that the electric and magnetic resonances are the same of an equivalent RLC resonant circuit (see Figure 3-9). The inductance and the capacitance can be expressed in terms of

geometric parameters. In the case of magnetic mode ,for example, the capacity can be approximated by that of a capacitance with plate faces and the inductance can be approximated by that of a solenoid. The inductance for both the magnetic and electric mode is the parallel with the inductance generated by the slab and that generated by the necks. With this assumption it's possible to approximate the magnetic capacitance and inductance as:

$$C^{(m)} \simeq P(P - 2W)/2h, \quad L^{(m)} \simeq 1/L_{slabs}^{(m)} + 1/L_{necks}^{(m)}, \tag{3.10}$$

where $L_{slabs}^{(m)} \simeq (P - 2W)h / P$ and $L_{necks}^{(m)} \simeq Wh / (P - 2D)$, see Figure 3-9.

As a result a magnetic LC circuit is induced by the charge distribution in the Fishnet with magnetic resonance frequency given by (102).

$$\omega_m = \frac{1}{2\pi\sqrt{L^{(m)}C^{(m)}}} = K\frac{c}{2\pi}\sqrt{\frac{1}{\varepsilon_d}}\sqrt{\frac{2}{(P - 2W)^2} + \frac{(P - 2D)}{WP(P - 2W)}} \tag{3.11}$$

Where c is the light speed and ε_d is the dielectric permittivity constant. On the other hand because of anti-parallel currents between the slab and the neck at the electric resonance frequency, the effective neck's inductance $L_{necks}^{(e)}$ is in parallel with the slab inductance $L_{slabs}^{(e)}$. As a consequence, the electric resonance frequency is given by (102):

$$\omega_e = \frac{1}{2\pi\sqrt{L^{(e)}C^{(e)}}} = \frac{c}{2\pi}\sqrt{\frac{\ln(b/t)}{P}}\sqrt{\frac{A}{(P - 2W)\ln\left(\frac{P - 2W}{P}\right)} + \frac{B}{W\ln\left(\frac{W}{P - 2D}\right)}} \tag{3.12}$$

where $C^{(e)} = P / \ln(b/t)$ is the approximate capacitance between two parallel wires of length P and radius t, (b is the separation between neighbor short-cut wires, it's the same of 2W) and the inductances $L_{slabs}^{(e)} = (P - 2W)\ln((P - 2W)/P)$ and

$L_{necks}^{(e)} = W \ln\big(W \, / \, (P - 2D) \big)$ are approximate formulas for a straight-wire inductance.

In the last relation, the increase of the first term in the sum (as a result of increasing *W)* counteracts the decrease of the first one and this leaves the electric resonance frequency almost unaffected (except the slow logarithmic variation *ln(b/t)*). The constant *K, A, B* are intrinsically related to the shape of the system and they don't have a simple analytic expression related to the geometric parameters. From Figure 3-5b it's possible to see that the electric resonance lies well above the magnetic resonance frequency ω_m. Therefore, the effective electric response of the Fishnet design is actually the Drude-like electric response of the continuous wires only. This effect is associated with an advantage for the *LH* behavior of the structure, stemming from the fact that the Drude-like effective ε experiences slower changes than an effective ε influenced by electric resonances and this allows a wide frequency spectrum of negative effective permittivity negative into which the negative permeability can overlap thus accomplish for negative effective refractive index.

3.7   Parametric simulations under *D, W, h* variation

The simulations will prove that the *LC* model is an effective description and guideline for metamaterial Fishnet. In order to optimize our design we perform a complete analysis varying all the geometric features of the Fishnet. In Figure 3-11 we perform a parametric simulation varying the width *W* of the squared holes. As shown in Figure 3-11, when *W* decreases both the electric and magnetic resonant wavelength increase (the electric resonance wavelength increases slowly due to the logarithmic dependence as just discussed above). This is predicted by the above formulas (Eqs.3.11-3.12). Physically, when *W* decreases, the electric-induced slab-dipole resonance wavelength

tends to increase (the resonance frequency tends to decrease). Thus the slab dipoles interact with the incident electric fields leading to a decrease of the resonance frequency. In Figure 3-11 the resonance at $\lambda=600$nm change from LH to RH when W decreases (the plasma wavelength is up-shifted). Moreover, reducing the parameter W corresponds to reducing the area of the holes thus disturbing the magnetic performance of the Fishnet. This leads to a weaker strength and to a positive values for the permeability around the electric resonance, see Figure 3-11c.

a)

b)

c)
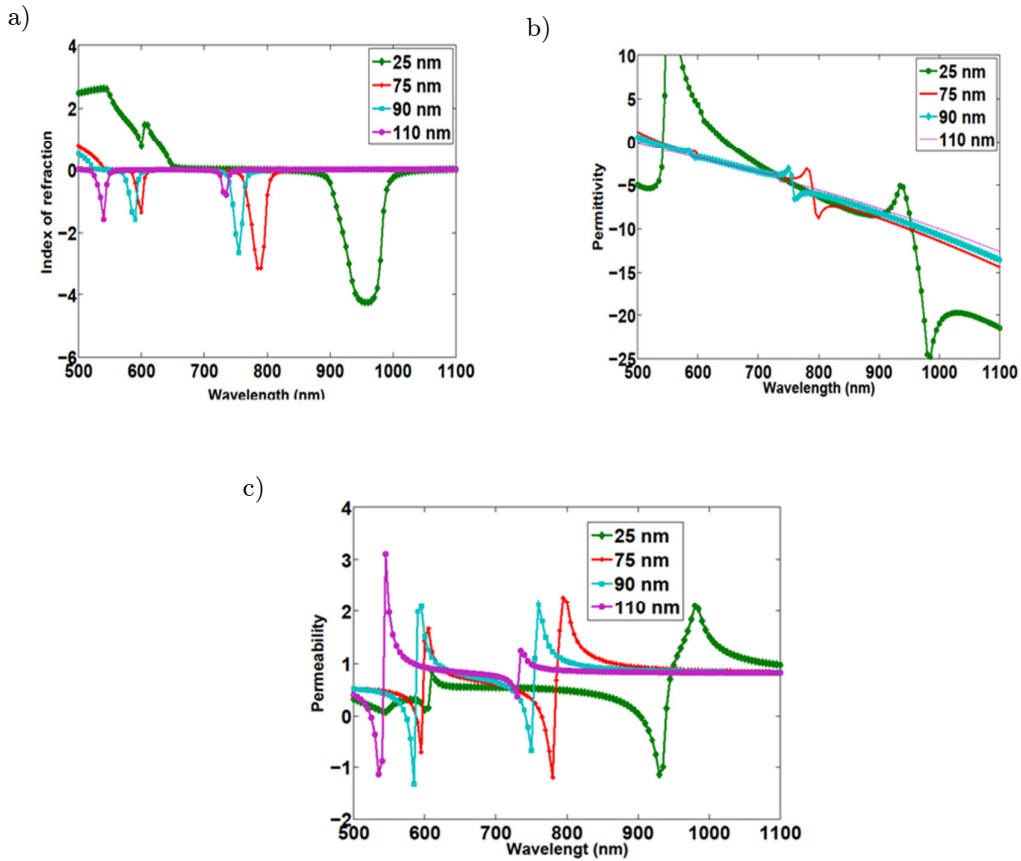
Figure 3-11. Refractive index (A), permittivity (B), permeability (C) varying the W parameters of the holes (from 25 to 110 nm).

In Figure 3-12 we perform a parametric analysis of the effective index of the Fishnet varying the hole width parameter D Figure 3-4. We see that both the magnetic and the electric resonances wavelengths increase when D increases. This is confirmed by the

above formulas (Eqs. 3.11-3.12). When D decreases the neck loop inductance decreases leading to a greater contribution for the neck's inductance to the magnetic resonance frequency (the magnetic resonant wavelength decreases), (see expression above for $L_n^{(m)}$). In the same way, also the electric inductance at the necks is reduced when D decreases leading to a greater electric resonant frequency (a shorter magnetic resonant wavelength), (see expression above for $L_{necks}^{(e)}$). A proportional down-shift of the effective plasma wavelength is seen when D decrease leading to well-shifted permittivity curves. This can be explained by the decrease of the continuous wire's plasma wavelength being inversely proportional to the electron density in the metal $\lambda_{e,p} = \left(n_\varepsilon e^2 \ / \ m_e \varepsilon_0 c^2 \right)^{-1/2}$. As we can see in Figure 3-12a when D increases the resonance at $\lambda = 600$ change from LH to RH for D greater than 150nm. This is due to an non-overlapping of the wavelength range of negative permeability and negative permittivity.
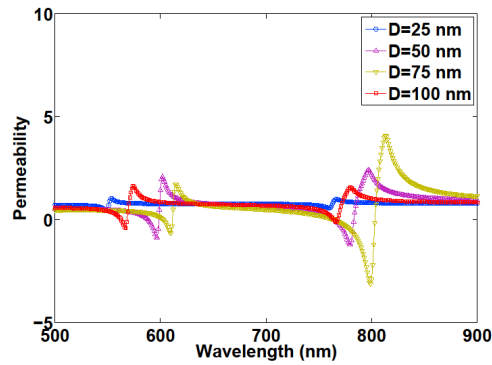
a)

b)
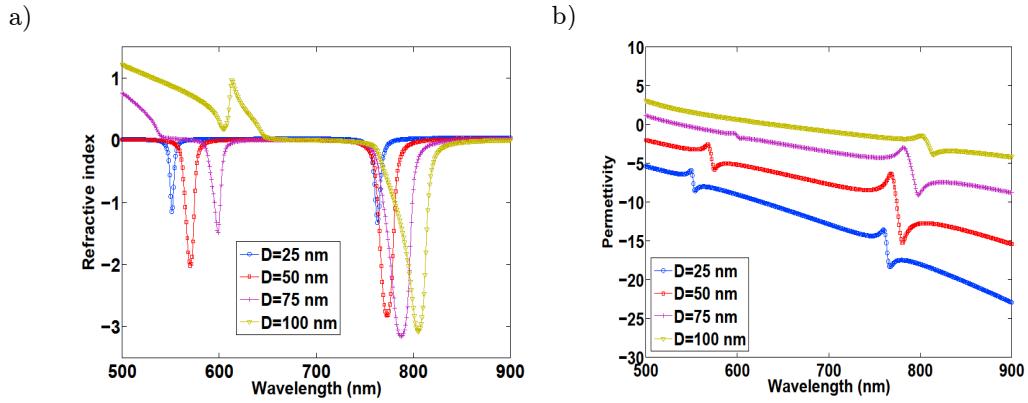
c)

Figure 3-12. Refractive index (A), permittivity (B), permeability (C) varying the D parameter of the hole.

For both D and W variations the LH behavior around the magnetic resonance wavelength $\lambda = 830$nm is quite unaffected. This is strictly related to the geometry of the unit cell. For this reason the Fishnet is a very favorable candidate structure in order to achieving negative refraction index in the visible range. Physically in a Fishnet-like structure the resonance electric wavelength lies well under the magnetic resonant wavelength (as we can see in all the above plots) and the effective plasma wavelength of the system lies above that of the continuous wires only (101). This leads to a great geometric parameter space that one can manage leading to a negative LH regime. In Figure 3-13 we have increased the dielectric layer thickness h varying the wavelength and plotting the absorbance. We see two distinct splitting converging to a common values (not shown here) which corresponds to the resonant wavelength of only one dielectric-metal interface. According to the LC circuit description the effective inductance is proportional to t, while the effective capacitance is inversely proportional to it ,so that their product as well as the magnetic resonance should not change. Instead by increasing the dielectric size h the hybridization model fails and the two modes at the opposite interface begin to decouple leading to an inappropriate description of the physics based on the simple LC circuit equations, (Eqs.3.11-3.12).
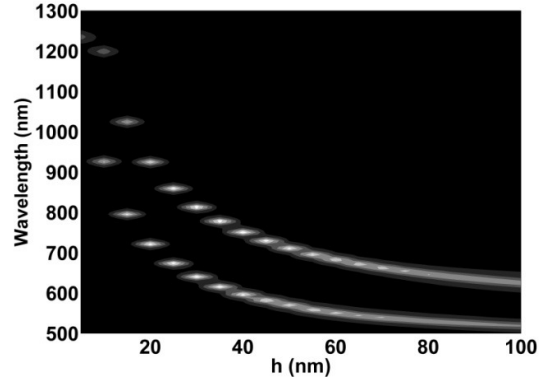
Figure 3-13. Scaling of the magnetic and electric resonances increasing the dielectric layer thickness h

3.8   Scaling law under P and a_z variation

In Figure 3-14 we have plotted the resonance magnetic frequency varying the period P of the Fishnet and the total stack thickness a_z (along the **k** propagation) of the unit cell. As expected from the formulas above, when all the geometric parameter (P,W,D,h,t) scale like P or a_z, the magnetic (as well as the electric) resonance scales like $1/P$ and $1/a_z$ respectively (the wavelength is proportional to P and a_z respectively). This linear behavior is confirmed by the plot in Figure 3-14a,b where we chose for both P and a_z values greater than 100 nm and 80 nm respectively , far from the saturation regime (103), (106).
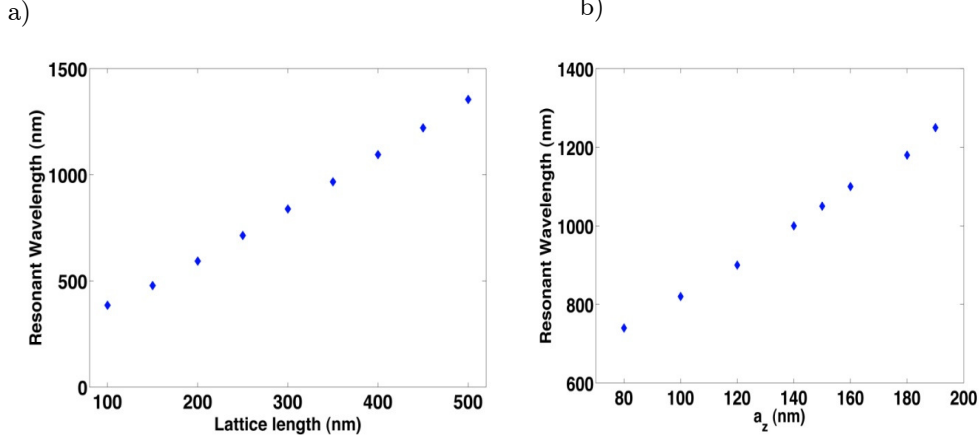
a)   b)

Figure 3-14. Linear scaling of magnetic resonance by varying the lattice constant P (A) and the total Fishnet stack thickness a_z (B)

The saturation regime corresponds to the frequency spectrum in which the scaling with the period or with the transversal size is no longer linear but saturates to a constant. In Eqs. (3.3-3.4) it has not taken into account for the kinetic energy of the electrons in the metal, E_k and its related inertial inductance because the simulations are far from this saturation regime and the scaling is linear. The inertial inductance originates from the electron inertia and represents the "difficulty" of electrons to follow high-frequency motions, i.e., their difficulty to respond to high-frequency fields. In the saturation regime one should replace the magnetic inductance of the system in the effective RLC circuit description by the total inductance resulting as a sum of the magnetic field inductance, L_m, and the kinetic inductance, L_e, where L_e is defined in $E_k = N_e m_e v_e^2 / 2 = L_e I^2 / 2$ (N_e is the total number of electrons, m_e is the electron mass, and v_e is the average electron-velocity). It can be shown (103), that after taken into account for the inertial inductance the general scaling law for the RLC circuit is

$$\omega_{LC} = \frac{1}{\sqrt{(L + L_e)C}} \propto \frac{1}{\sqrt{A_1 a^2 + A_2}} \qquad (3.13)$$

where A_1 , A_2 are constants depending on the geometry of the system and a can represent the period or the transversal size depending on the scaling. The first term

under root depends on the total magnetic inductance while the second term is only due to the inertial inductance contribution. The scaling law (Eq.3.13) shows that reducing a to zero has as consequence the saturation of the resonant magnetic frequency ω_{LC}.

3.9   Scaling with dielectric permittivity ε_d

Important effects on the behavior of the metamaterial stack are connected with the modulation of the dielectric constants values of the dielectric layer. Several materials present modulable dielectric constants values, such for example electro-optic ferroelectric crystals that allow electrically controlled tunability (107), or materials that under semiconductor-to metal phase transitions such as VO_2 and can be thermally and reversibly cycled leading to refractive index variations as large as Δn=0,55 (108). This can potentially allow very interesting modulable effects on the position of the negative refractive index peak. In Figure 3-15 this effect can be easily observed. The linear dependence of the magnetic resonant wavelength on the dielectric constant ε_d of the dielectric spacer is moreover predicted by Eq. 3.11.
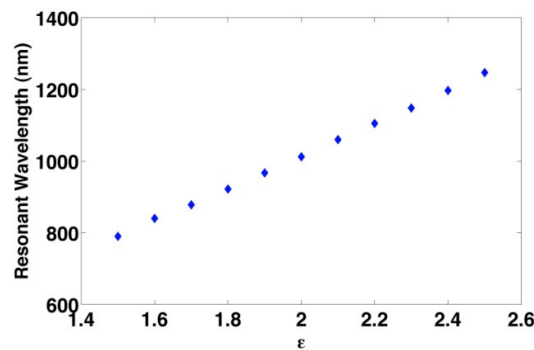

Figure 3-15. Linear scaling of the magnetic resonance by varying the dielectric costant ε_d of the dielectric spacer.

64

3.10 Conclusion

In this chapter we carried out a comprehensive theoretical analysis of the Fishnet metamaterial in the optical spectral range based on the effective parameters retrieved from simulation. We first operated a systematic variation of the two widths parameters of its holes. Even if this influences the negative left handed regime around the electric resonance, it doesn't affect the LH behavior around the magnetic resonance. This suggests the possibility to employment of the Fishnet structure for achieving negative refraction index around the magnetic resonance in a wide region of the optical spectrum. Moreover we varied the dielectric spacer observing that the simple LC circuit interpretation is not longer valid when the dielectric size increase above tens of nanometers. A theoretical explanation in terms of $LRSP$ is needed for a better understanding of this phenomena. Moreover, as clearly illustrated it is possible to tune the position of the resonance peak acting on the unite cell lattice parameters and the total Fishnet stack thickness. Moreover a particularly interesting result regards the prospect of tunable $NIMs$ related with the dependences of the negative refractive index band position on the dielectric constant of the dielectric layer. As is well known several materials present reversible modulable dielectric constants values, such as for example electro-optic ferroelectric crystals or materials that undergo a metal-insulator phase transition.

4   Multilayered Fishnet and bianisotropy

In the last two years, there has been much progress towards the realization of NIMs at optical frequencies. This has included numerical studies of infrared magnetic metamaterials (109) and *NIMs* (110) and experimental demonstrations of THz, mid-infrared and near-infrared magnetic metamaterials (37), (111),(63),(64) as well as near-infrared *NIMs* (112),(65). However, to date, the experimentally demonstrated near-IR NIMs exhibit large *Im*(n), which makes them unsuitable for many applications. As a result, a figure of merit, just introduced in the last chapter as the ration $-n'/n''$, has been introduced (112) to allow comparison between different *NIM* structures. As shown in (112), a thin metamaterial ($\ll\lambda$) slab consisting of a metal/dielectric/metal layer stack with a periodic array of holes exhibits a negative refractive index in the vicinity of its quasi-static *LC* resonances. This thin metamaterial slab can be considered as a basic *NIM* building block that can be used to construct a much thicker metamaterial ($\sim\lambda$). The evolution of the optical properties of a metamaterial as a function of the number of unit cells is an interesting question in its own right as well as providing insight into the design of *NIMs* (113). Most of the metamaterials exhibiting artificial magnetism, and a negative refractive index n at THz and optical frequencies consist of only a functional layer. The number of actual layers *M=2N+1*, where *N* is the number of functional layers. The first five-functional layer of SRRs operating at 70 THz (114) was published in 2008 and recently, a ten-functional layer of Fishnets (21 layers of silver and AL2O3) operating at 200 THz was fabricated (115). However, it is very important to study how the optical properties (ε, μ, and n) change as one increases the number of layers. How many layers are needed to achieve convergence of the optical properties and can one call this metamaterial bulk? How do optical properties

behave as one changes the distance between two neighboring Fishnets? If the distance is small, there is a strong-coupling . The convergence of optical properties is slow, and more importantly, it does not converge to the isolated Fishnet case (113), (116). Actually it's not well understood the mechanism at the base of the field distribution in a multilayered Fishnet metamaterial. In this chapter a phenomenology model will be presented inspired by the 'magnetic' molecule model (117). In this model the electromagnetic modes between the Fishnet layers couple in a similar way as a 'magnetic' molecule system hybridize. In the last third section a modal analysis will be performed in order to identify the electromagnetic modes of the multi-layered Fishnet metamaterial (up to 7 layers) to the Bloch-modes of a 2D-periodic structure.

4.1   Negative Refractive index of a multilayered Fishnet structure.

In this section, a detailed study on the coupling effects in stacked magnetic metamaterials in the optical frequency regime will be presented. The formation of 'magnetic molecules' from coupled 'magnetic atoms' in stacked Fishnet metamaterials has just been be demonstrated (117) together with the concept of 'magnetic molecules' as well as 'magnetic solids', generalizing the plasmon hybridization scheme to N 'magnetic atoms' that form a 'magnetic solid'. The evolution of effective material parameters with increasing layer numbers will be shown. Figure 1 shows the schematic of a stacked Fishnet structure, which is constructed from five alternating layers of silver Fishnets and dielectric spacers.
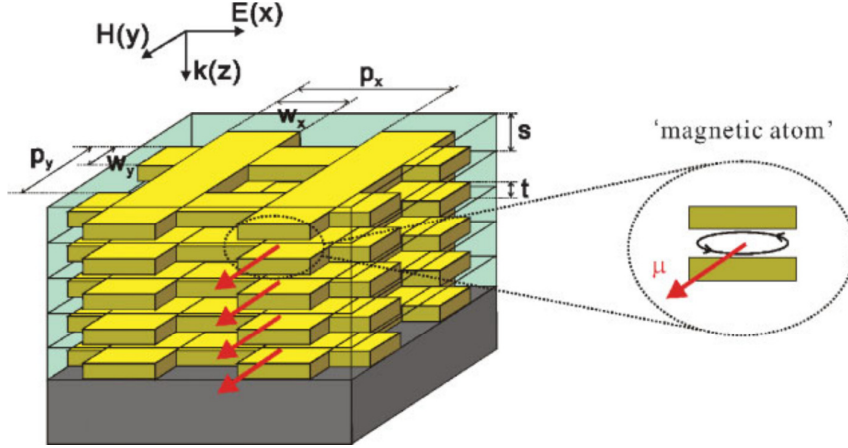
Figure 4-1. Schematic of the polarization configuration and the structure design for a 5-layer Fishnet metamaterial. The geometry parameters are $w_x = w_y = 150$ nm, $p_x = p_y = 300$ nm, $t = 30$ nm, and $s = 70$ nm. Right: The definition of a 'magnetic atom' is highlighted. The solid black circle represents the circular current excited between a double-wire pair. The red arrows in the figure denote the magnetic moments associated with the 'magnetic atoms'. Here, we plot the specific mode with all magnetic moments aligned in parallel.

In the structure, the wire widths, w_x and w_y are designed to be equal for the consideration of an improved polarization behavior, i.e., polarization independence in *x*- and *y*-directions. In order to investigate the resonant behavior with the number of stacked layers, 2-, 3-, and 4-layer structures with the same geometry have been studied for comparative analysis. All numerical simulations were performed with the FEM software COMSOL. The permittivity of silver is described by the Drude model with the plasma frequency $\omega_{pl} = 1.37 \times 10^{16} s^{-1}$ and the damping constant $\omega_c = 8.5 \times 10^{13} s^{-1}$ (96). A dielectric spacer with refractive index of 1.63 (AL2O3) has been employed. The simulated reflectance and transmittance spectra for different layers of structures are presented in Figure 4-2a,b respectively. The character of the resonances manifests itself in the reflectance spectra. As shown in Figure 4-2a, one resonance (I_1) is observed for the 3-layer (one functional layer) structure, whereas two resonances (I_2 and II_2) are clearly visible in the case of the 5-layer structure. There are three (I_3, II_3 and III_3) ,

four (I_4, II_4, III_4, and IV_4) and five (I_5, II_5, III_5, IV_5 and IV_5) resonances emerging in the case of 7- , 9-layer and 11-layer structures, respectively, for the entire observed spectral region.
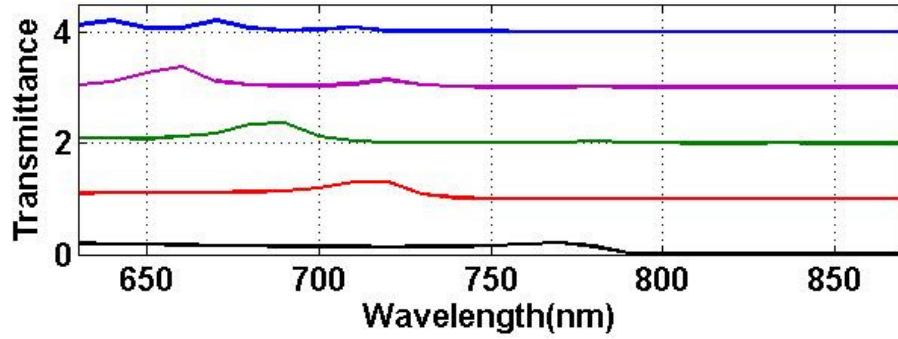
a)
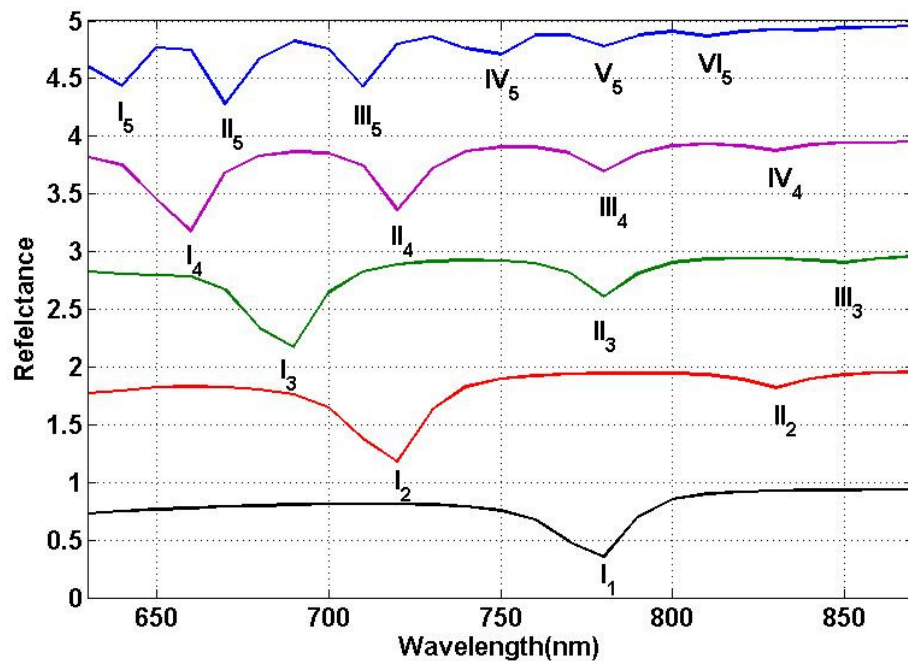
b)

Figure 4-2. (a) Reflectance for N=1 (black), N=2 (red), N=3 (green), N=4 (magenta), N=5 (blue). (b) Transmittance, colours like in (a)

To understand the origin of the spectral characteristics, the distributions of the electric currents J_x at the resonances for different layers of structures are depicted in Figure 4-3. The contour plots represent the current vector distribution in a slice cutting the unit cell in the middle of the air hole and laying at y=0 plane. The positions of the dielectric and metallic layer alternating in the Fishnet are marked by black lines in the corresponding figures. The electric currents distribution at resonance I_1 is illustrated in Figure 4-3a. As has been discussed in the last chapter the incident light field can induce an electric resonance (not shown here) and a magnetic resonance at higher and lower frequencies, respectively. In the following, the studies will be concentrated on the evolution of magnetic resonances, induced by the electric currents, with increasing Fishnet layer numbers. Actually, for the 3-layer Fishnet structures, the magnetic resonance is associated with the excitation of a circular current loop between the double-wire pair. This corresponds to an induced magnetic dipole moment inside the spacer layer, giving rise to a magnetic response to the incident electromagnetic field.
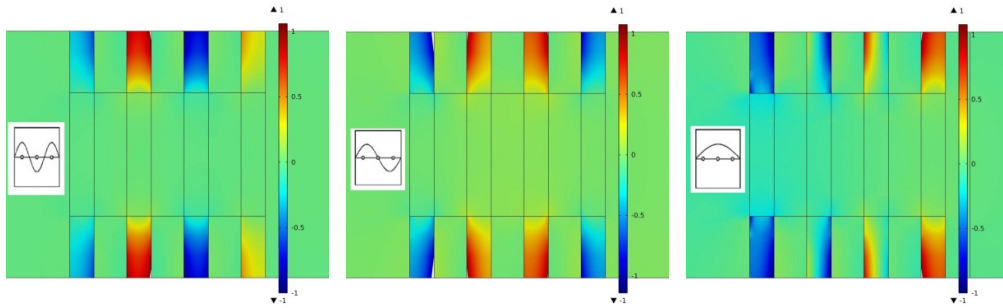
a)
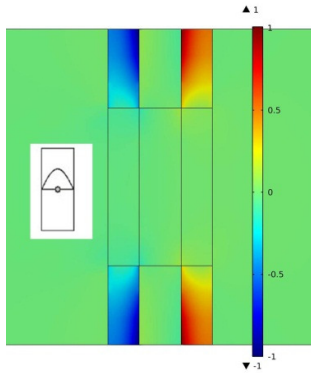
b)
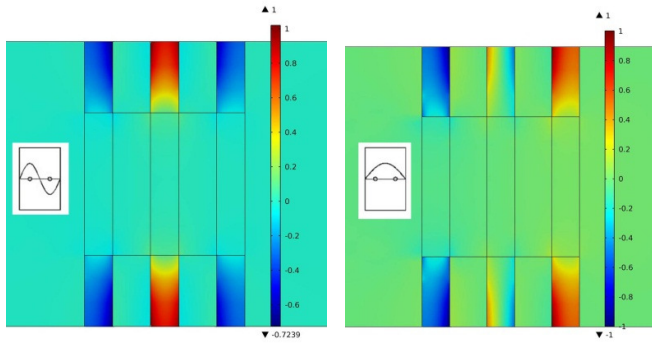
c)

Figure 4-3 Simulated electric current of Jx in the plane y=0 at the corresponding resonant frequencies together with the schematic wave-functions for (A) 1-, (B) 2- and (C) 3-functional layer Fishnet metamaterials. The grey circles in the schematic drawings represent the 'magnetic atoms'.

In analogy to electric plasmons excited in metallic nanostructures, the magnetic dipole oscillation inside the spacer layer has been defined (112) to be a magnetic plasmon. For the 5-layer structure, two circulating current loops are induced in the three-wire

71

system, with the central metallic wire acting as the common layer for the flowing currents. It leads to the excitation of two localized magnetic dipole moments inside the neighboring spacer layers as depicted in Figure 4-3b, oscillating in-phase and anti-phase with respect to one another at resonances I_2 and II_2, respectively. The above phenomenon has been well interpreted using the hybridization of magnetic plasmons. (118) The close proximity results in the coupling between the magnetic plasmons inside the two neighboring spacer layers and gives rise to the formation of two new hybridized modes: the symmetric mode and the anti-symmetric mode (119),(118). The resulting two magnetic resonances I_2 and II_2 blue-shift and red-shift, respectively, in comparison to resonance I_1, which corresponds to the bare mode of an individual magnetic plasmon. This is a clear signature of the interaction between the two plasmons. Taking this one step further, the 7-layer structure forms three hybridized modes as presented in Figure 4-3c. One mode is fully symmetric (resonance III_3), one mode is fully anti-symmetric (resonance I_3), and the intermediate mode is non-symmetric between neighbors (resonance II_3). As demonstrated by the reflectance spectra of Figure 4-2a, resonances I_3 and III_3 show a further blue-shift and red-shift compared to resonance I_1, respectively, whereas resonance II_3 is situated nearly at the same spectral position of resonance I_1. The general effect of adding successive Fishnet stacked layers is to introduce additional hybridized modes as well as to spread the range of resonant energies. In fact, the whole picture discussed above is a compelling analogy to the formation of linear molecules from single atom wave-functions (120). In this case, each magnetic plasmon excited inside a double-wire pair can be regarded as an excitation of a 'magnetic atom' (see Figure 4-1). When a second 'magnetic atom' is added, the interaction of the two 'magnetic atoms' leads to the energy splitting and the formation of symmetric and anti-symmetric 'molecular orbitals'. Subsequently, when further 'atoms' are added, the interaction of the 'magnetic atoms' with their nearest neighbors will result in additional energy levels and lead to the formation of complex artificial

'magnetic molecules'. A schematic which describes the 'molecule formation' is illustrated in Figure 4. The energy levels are constructed with the fully anti-symmetric mode having the lowest and the fully symmetric mode having the highest energy, consistent with the picture of transverse dipole-dipole interaction (121). In addiction the oscillator strength of the individual magnetic modes can also be deduced from the dipole arrangements: Neighboring antiparallel dipoles cancel each other, while neighboring parallel dipoles add up. As a consequence, the fully anti-symmetric mode has very little oscillator strength, whereas the fully symmetric mode has the largest oscillator strength and therefore strongly couples to the light field. This interpretation is confirmed by the simulated spectra in Figure 4-2. respectively. Intuitively, when N 'magnetic atoms' have been included, an energy band consisting of N different energy levels will be formed (120) as depicted in Figure 4-4 and this constitutes a 'magnetic solid'.
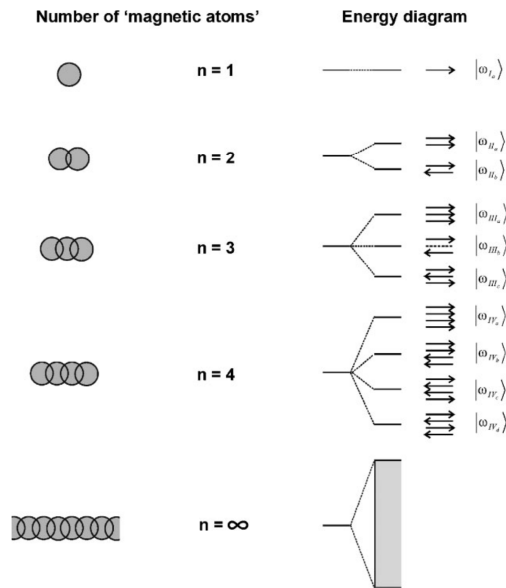

Figure 4-4 Energy diagrams describing the hybridization principle resulting from the interactions of magnetic plasmons in stacked Fishnet metamaterials.

Transmission and reflectance for N=1-5, have been numerically calculated in Figure 4-2a,b and inverted in order to extract the effective refractive index using the just mentioned method discussed in Chapter 2. For a single unit cell

(air/metal/dielectric/metal/air), the transmission shows a peak around 775nm and a dip around 780nm. With an increasing number of layers, the transmission at long wavelengths (λ >790nm) decreases rapidly and approaches zero, consistent with a simple metallic response away from resonance. For multiple unit cells at wavelengths below 790nm, T and R exhibit characteristic one-dimensional Fabry-Perot slab oscillations. As will be shown later, this is the negative index region. This number of resonances (five for the N=5 structure) is due to the large and varying absolute value of the effective index across the negative refraction region. Further increasing the number of metamaterial layers eliminates the oscillation in transmission and reflectance curves and gives the asymptotic feature for a bulk, lossy metamaterial, as shown in (122) where a multi-stack of 200-layesr has been simulated for the bulk Fishnet-metamaterial in μm regime.
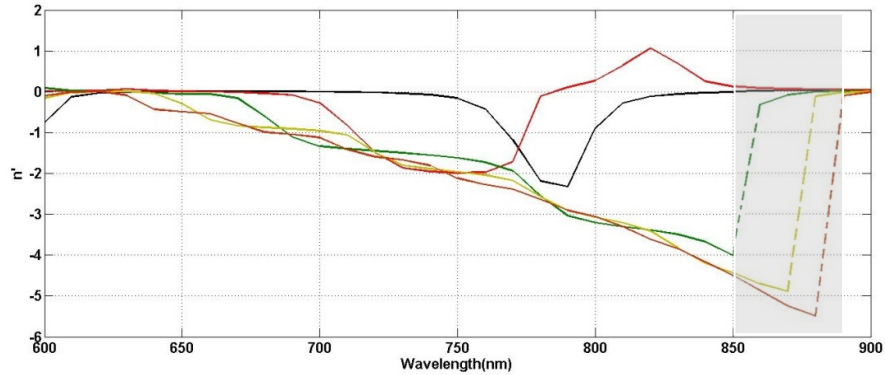

Figure 4-5. Refractive index extracted from the complex coefficient of transmission and reflectance for different numbers of unit cells. The black, red , green, yellow, brown solid lines represent the effective index extracted from slabs consisting of 1, 2, 3, 4 and 5 functional layers respectively.

As shown in Figure 4-5 for N=4,5 the refractive index converges well to the asymptotic bulk value. The shadow region in Figure 4-5 show a discontinuity in $Re(n)$ at around 900 nm. However, to meet the requirement that the refractive index be consistent for different number of unit cells of metamaterial, we need to accept these two branches for different wavelength regions. For wavelengths over 890nm, the real part of index is almost zero and the imaginary part (not shown here) is much larger

than the real part, exhibiting metallic properties. For light propagating in a periodic structure, an infinite number of modes exist for a given frequency (each mode is the linear combination of many Floquet plane waves based on the periodicity in the transverse directions). As the number of unit cells along the propagation direction is increased, the mode with the smallest imaginary part dominates the optical response (122),(116). The reason for the discontinuity has been cleared in (122): the imaginary part of the fundamental mode exceeds that of the first higher mode for wavelengths above 850nm, and therefore, for a thick slab, the second mode becomes the dominant mode at longer wavelengths. As shown in Figure 4-5, the effective index calculated for five to ten layers converges very well except for a narrow wavelength range around 850nm where the two modes exhibit comparable losses, indicating that the fundamental mode is absolutely dominant over other modes over most of the frequency range (up to 850nm). A modal analysis will be presented in Chapter 6 which reproduces the complex dispersion curves of the first least-damped modes in such structure.

4.2   The role of surface polaritons in multilayered Fishnet metamaterial

A surface plasmon polariton (*SPP*) is an electromagnetic surface wave traveling along the interface separating a dielectric and a metal. It is produced by the interaction of collective oscillations of free electrons in the metal surface with the electromagnetic wave impinging on the metal. The first theoretical description of surface plasmons dates back to 1957 when Ritchie (123) predicted the existence of surface plasmons when he discussed the plasma losses in thin films. However, it was in 1998, when Ebbesen *et al.* (124) published their pioneering work about Extraordinary Optical Transmission ˙EOT˙ through hole arrays in metallic films, when SPPs attracted the attention of fundamental research giving rise to the field of plasmonics. Since then, other studies have proved the existence of *EOT* (for a complete review see (125)), mostly on single-layer metal films with periodic hole arrays, being well accepted that the *EOT* through single-layer hole arrays originates from the grating coupling between

the dispersion relation of the SPPs that propagate along a smooth infinite metal-dielectric interface and the momentum of the incident light taking into account the lattice structure provided by the holes. However, this procedure has to be considered as an approximation due to the fact that it models the momentum of the *SPPs* on a holed array using the expression of SPPs on a smooth metal-dielectric interface, thus ignoring the effect which the holes may have on the *SPP* propagation. Nevertheless the predictions of this model are usually very accurate (126). In the last session the phenomenological model of 'magnetic molecules' has been discussed in order to explain the distribution of magnetic resonances inside a multi-layered Fishnet metamaterial. Only the magnetic resonances have been taken into account. Next numerically studies are carried out to find the correlation (at least in a good approximation) between all the magnetic resonances of a N= 1,2,3 and 4 functional layers Fishnet metamaterial. It is known that when two metal layers are placed closer than the *SPP* attenuation length, the *SPPs* that propagate along each of the two inner interfaces couple to each other, thus creating a mode called internal *SPPs* whose dispersion relation differs from the usual aforementioned dispersion relation of the SPPs on a single interface. In the fellow will be presented, in analogy with the model for single-layer hole arrays, the dispersion relation of the *SPPs* propagating on a multilayer structure without holes and it will be equate with the momentum of the incident light ,taking into account the periodicity of the structure provided by the holes.

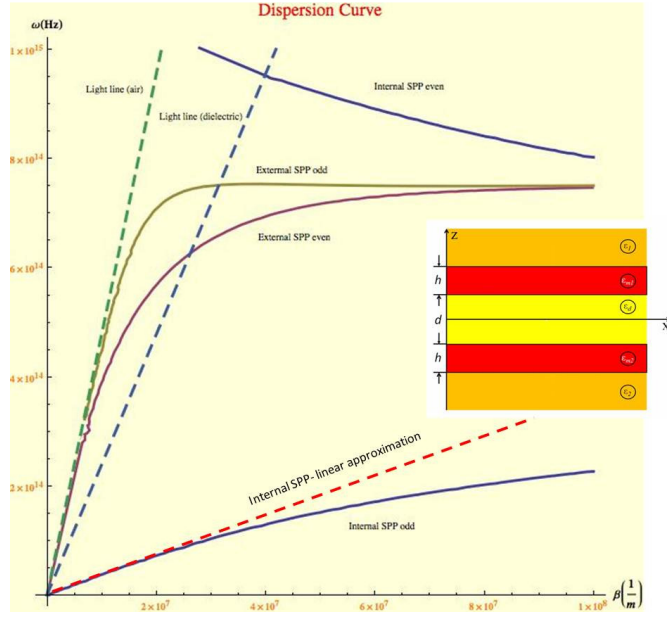In Figure 4-6 the analytic dispersion curves for a 5-layers structure is shown.

Figure 4-6. Dispersion relation for a 5-layers periodic structure. The inset is the schematic of the 5-layers structure.

To calculate the dispersion relation of the structure the waves are considered propagating along the *x*-direction of a Cartesian coordinate system, showing no spatial variation in the perpendicular, out-of-plane *y*-direction (see Figure 4-6). The solutions with an evanescent decay in the *z*-direction normal to the interfaces are considered, i.e., propagating wave solutions confined to the interfaces (126). After imposing the proper boundary conditions an analytic expression can be obtained (127). The metal layers (depicted in red in the inset of Figure 4-6) are 30 nm thick and the dielectric layer is 5 nm thick (depicted in yellow in the inset of Figure 4-6). The internal dielectric layer is responsible for two internal modes (for the two metal-dielectric internal interfaces) They are symmetric and anti-symmetric modes depending on the field distribution between the two internal interfaces and they always exist when the dielectric separation is not so large to prevent the modes to couple each other (126). The small dielectric separation (5 nm) allow the external mode to couple too. With an analogue mechanism they appear to be symmetric or anti-symmetric coupling. The analytic expression of this simple stack has been explicitly derived in (127), (128) and the algebraic computation is a little laborious. Moreover the analytic curve has an

77

implicit dependence by frequency and wave vector. When more layers have to be taken into account the computation becomes even challenging. A simple way to overcome the algebraic computation is to employ a modal analysis for extracting the dispersion curves in a more straightforward way by simulation. The out-of-plane modes package in COMSOL has been used. This 2D simulation calculate modes propagating in the third direction (perpendicular to the computational plane) with periodic boundary condition in one direction (x-direction for the present case) and with PEC (Perfect Electric Conductor) condition under and above the unite cell. Once know the way to simply extract the dispersion curves for a multi-flat layered structure evolving in the z-direction it's possible to equal them (in good approximation) to the momentum of the incident light (tacking into account the periodicity of the structure provided by the holes).

$$\left| \overline{k}_{SPP,flat} \right| \simeq \left| \overline{k}_{SPP,holes} \right| = \left| \overline{k}_x + \overline{G}_{i,j} \right| = \left| \overline{k}_0 \sin \phi + i \overline{G}_x + j \overline{G}_y \right| \tag{4.1}$$

The second step is to extract the reflection and transmission coefficients of the multi-layered system. In this way it's possible to identify the modes of the stacked structure by equaling its resonant frequencies to the ones of the dispersion curves. The modal analysis for the flat multi-layered structure and its correlated full vectorial simulation for multi-layered structure with periodic holes has been performed for 1 up to 4 functional layers structures with period P=600nm, hole sizes w_x, w_y =100nm, and metal (Drude silver)/dielectric (n=1.38) spacers of h_m= h_d=30nm respectively. In Figure 4-7 the dispersion relations for a 27-multi-layer structure (*N*=13) has been calculated with the modal solver. As predicted by Economu (127) the internal modes of a multi-layered structure (13 in this case) have a phase velocity

$$\tilde{c} = c \left[h_d \bigg/ \left(h_d + 2\lambda_p \frac{\exp(2k_m h_m) + 1 - 2\cos(ah)\exp(k_p h_{m)}}{\exp(2k_p h_m) - 1} \right) \right]^{1/2} \tag{4.2}$$

Where $h = h_m + h_d$ and λ_p, k_p are the plasma wavelength and wave-number wavelength respectively. The cyan curve is a particular solution of Eq. (4.2) with $cos(ah)$=0. All the internal modes are confined among two extremes, c_{min} and c_{max} (the green curves in Figure 4-7) obtained from Eq. (4.2) with k_p<<1,(127).
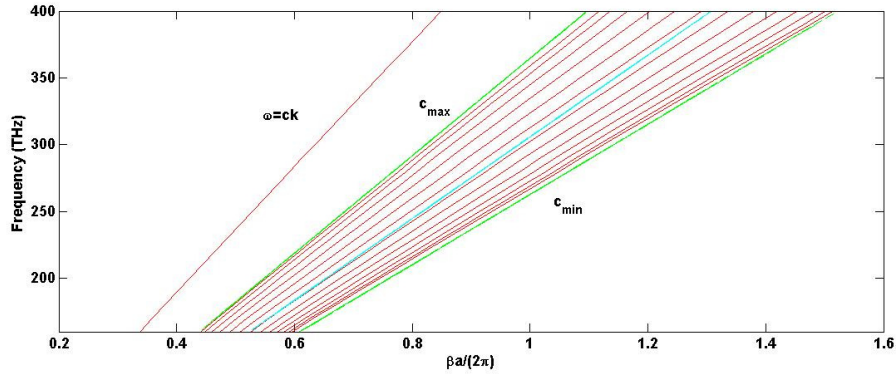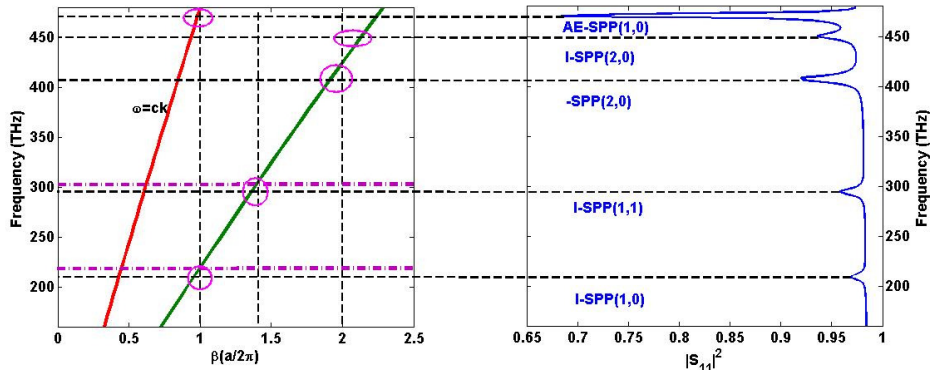

Figure 4-7.Dispersions curves for a 27-layer structure along z-direction.
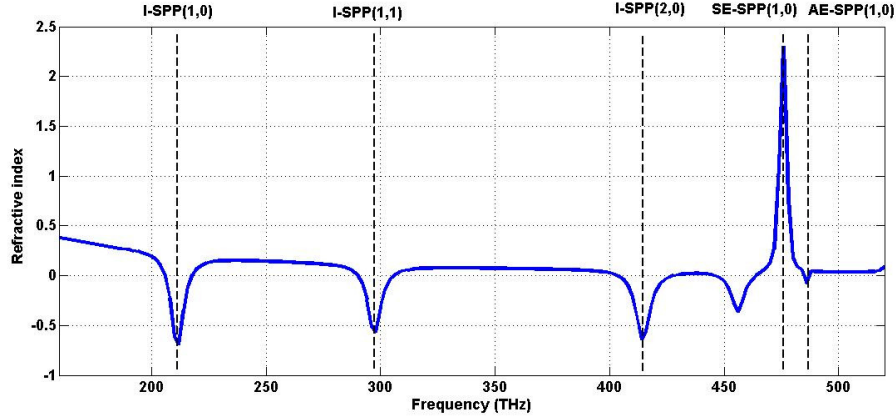
a)

b)

Figure 4-8. (a)-left: dispersion relation from the model analysis for a 3-layer structure along the z-direction in the flat case. The red curve is the light curve, the green curve is the dispersion of the internal modes. (a)-right: $|S_{11}|^2$ parameter for the 3-layer Fishnet with periodic holes. (b) refractive index of 3-layer Fishnet metamaterials.

In Figure 4-8a is shown the comparison between the frequencies predicted by the modal analysis and the resonant frequencies associated to the reflectance deeps for several values (i,j) of internal (I-SPP) and external (E-SPP) SPP modes. In Figure 4-8a the predicted frequencies are seen to approximately match the simulated spectra reflectance deeps (correlated to the *EOT* peaks) according to Eq. (4.1). Agreement between simulation and the model is not perfect because the dispersion relation of the *SPPs* used as matching condition does not take into account the presence of the holes, which cause scattering losses and a resonance shift. As a consequence, the predicted resonant frequencies are slightly larger than those obtained by simulations (128). The magenta circles mark the frequency region of the matching while the magenta dashed horizontal lines represent the resonant frequencies for the same model with smaller hole (60nm thick). In this last case the matching is even better as expected.
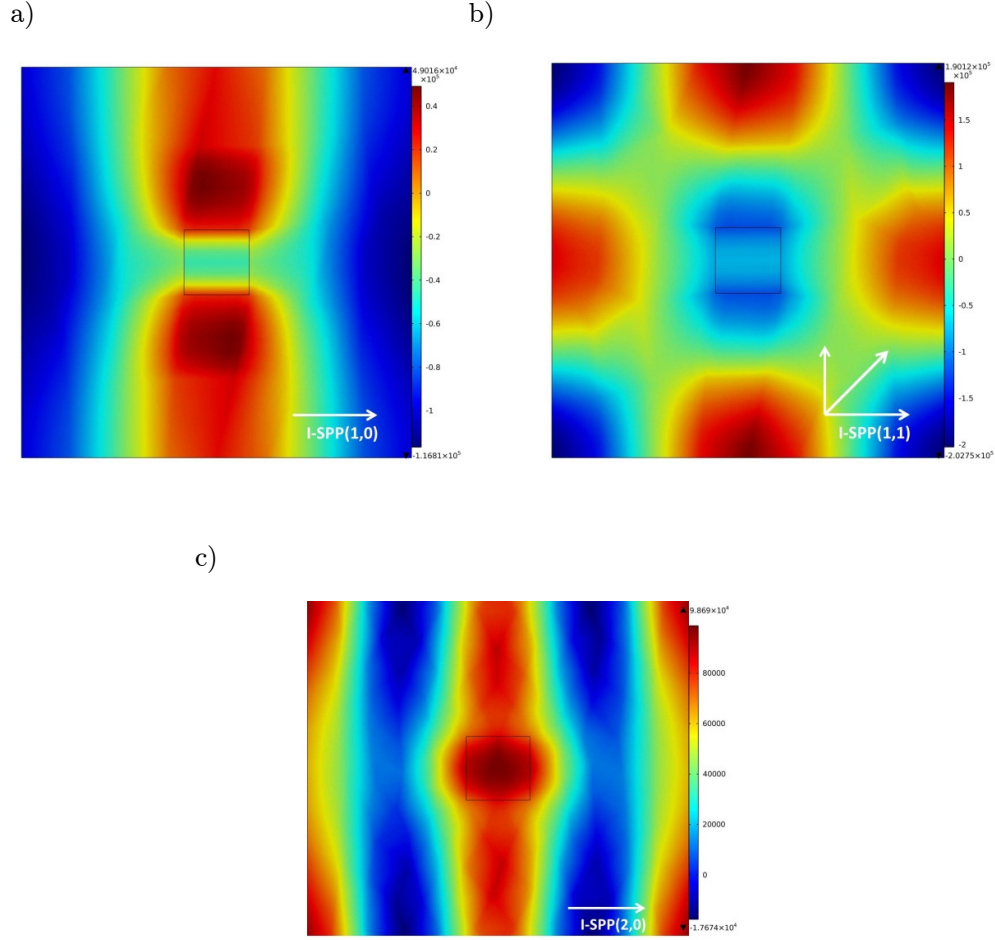
a)

b)

c)

Figure 4-9. Magnetic internal modes for the 3-layer Fishnet metamaterial calculated in a plane perpendicular to the k-direction and cutting the hole in the middle of the dielectric spacer. (a) y-magnetic component at the first I-SPP(1,0) resonance. (b) y-magnetic component at the first I-SPP(1,1) resonance. (c) y-magnetic component at the first I-SPP(2,0) resonance.

The first internal modes can be enumerated, on the base of the grating order coupling, as I-SPP(1,0), I-SPP(1,1), I-SPP (2,0) and are shown in Figure 4-9(a,b,c) respectively. Consequently, the y-magnetic component in Figure 4-9 fellows the grating direction $\Gamma - X$ (Figure 4-9a and c) and $\Gamma - M$ (Figure 4-9b) of the first reduced Brillouin zone. Figure 4-8b shows the refractive index for the 3-layer Fishnet metamaterial. The negative refractive index deeps are associated to the first internal *SPPs*. Although the permeability (not shown) is positive due to the small hole, w=(P/6), preventing a strong magnetic performance in the Fishnet, the high negative permittivity (not shown) and high losses can fulfill the single negative condition $\varepsilon'\mu'' + \mu'\varepsilon'' < 0$.
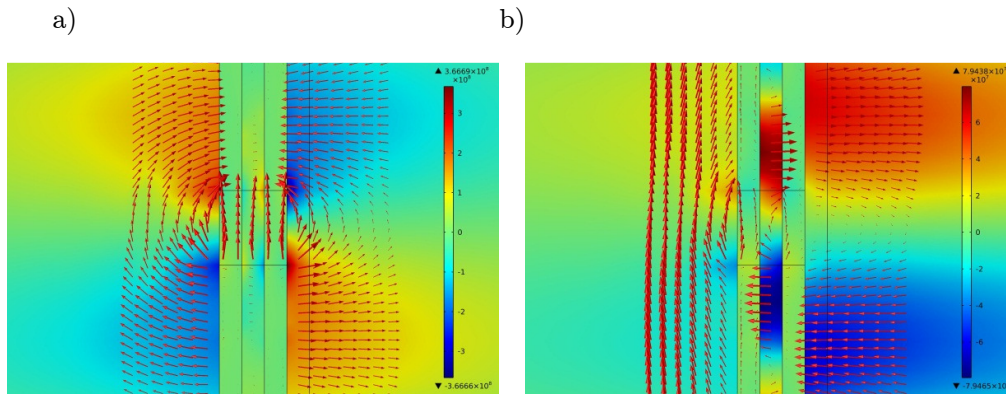
81

Figure 4-10. Magnetic external modes for the 3-layer Fishnet metamaterial calculated in the x-k plane and cutting the hole in the middle of the unit cell. (a) symmetric mode, (b) anti-symmetric mode. The arrow represent the electric field.

The internal *SPPs* show in general less transmission than the external *SPPs* as they are concentrated inside optically thick metallic layers which increase the attenuation due to the absorption of the metal layer. The external *SPPs* peak show high transmission, as the *EM* field is concentrated at the edges of the holes and the transmission is achieved by tunneling through them (129). At frequencies of 474THz and 486 THz two external resonances appear in Figure 4-8b. The first external resonance is symmetric as shown in Figure 4-10a. It can't cause the refractive index to be negative as shown in Figure 4-8b because no internal electric loop is generated between the metal plates (see Figure 4-10a) and the electric field is almost all concentrated inside the air hole. On the

contrary the second external resonance is anti-symmetric as shown in Figure 4-10b and some virtual current loop is clearly seen between the metal plates in Figure 4-10b, enabling the refractive index to be negative.
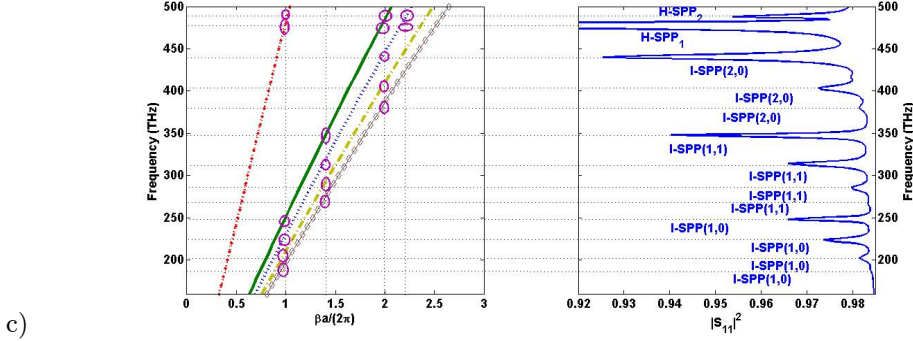

a)

b)

c)
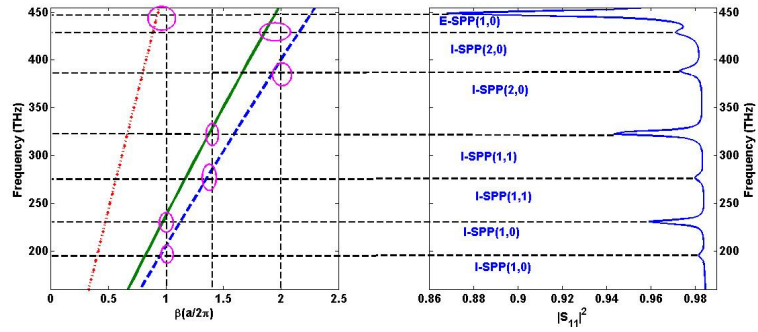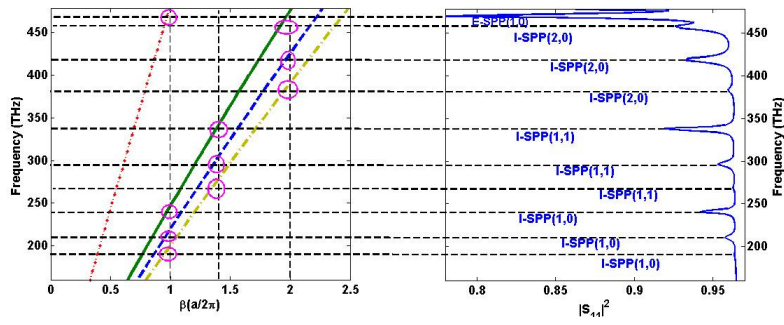
Figure 4-11. As in Figure 4-8 for (a) *N*=2 functional layer, (b) *N*=3 functional layer and (c) *N*=4 functional layer.

In Figure 4-11 the comparison between the modal curves and SPP resonant frequencies for N=2,3,4 functional layer is shown. Note that the 1-layer resonances split into *N* in the multilayer configuration (130). By increasing the number of layers, the new resonances blue-shift and their strength becomes stronger because of the stronger coupling between the 'magnetic atoms' as just shown in the last section. In Figure 4-11c the external resonances are so close to the internal resonances I-SPP(2,0) and I-SPP(2,1) that the reflection deeps overlap, thus forming two single hybridized deeps (H-SPP$_1$, H-SPP$_2$) in which the resulting EM field has a (2,0) and (2,1) pattern in the inner dielectric layer and a (1,0) pattern in the claddings.

4.3   Conclusion

In conclusion, it has been shown that plasmonic building blocks can be utilized for the construction of 'magnetic molecules' in metamaterials. In particular, we correlated the magnetic plasmons excited in stacked Fishnet metamaterials with artificial 'magnetic atoms'. We investigated in detail the evolution of the magnetic response with respect to increasing layer number. It has been shown that the plasmon hybridization method, which is generally applied to describe electric interactions in complex metallic nanostructures, can also be used for understanding the magnetic interactions in stacked

84

Fishnet metamaterials. This allowed us to classify and explain the rather complex spectra in the case of up to 3-functional layered Fishnet metamaterials. More specifically, the interaction of the magnetic plasmons or namely 'magnetic atoms' leads to the formation of artificial 'magnetic molecules', following the same hybridization mechanism of simple atoms bonded into linear molecules. An easy scheme for evaluating the oscillator strength of different coupled modes was proven to be applicable. Moreover it has been obtained analytically the dispersion relation of SPPs in a double-layer metallic structure and it has been shown by numerical analysis that light coupling to the external and internal *SPPs* originates *EOT*. A good matching between the theoretical and simulated resonant frequencies is observed. In addition, at the internal-*SPP* resonant frequencies a negative effective permeability is achieved as a virtual current loop is formed between the metallic layers which can be used to design negative-index metamaterials. Understanding the coupling of evanescent waves in complex double-layer metallic hole arrays nanostructures is of fundamental interest and practical importance in designing optical devices that could become important building blocks in future nano-optical systems.

5   Experimental Fishnet

In the recent years metamaterials have attracted more and more interest in the scientific community. A first example of a material with a negative index was represented by the split-ring resonators (*SRRs*). Such magnetic structures were realized in the spectral range from microwave up to 200 THz. To create a metamaterial at optical wavelengths other structures were proposed [13], however in all the cases small periodicities (about 300 nm and less) and tiny feature sizes (about 30 nm) are essential. Thus, the fabrication of optical metamaterials is challenging since high-precision, high-throughput, and low-cost manufacturing processes are needed. Feature sizes can require nanofabrication processes with sub-100-nm resolution. For rapid prototyping of metamaterials, focused-ion beam milling techniques can be used. In *FIB*, a focused beam of gallium ions is used to sputter atoms from the surface and it is used as a micro-machining tool, to pattern materials at the micro and nano-scale. Recently, this technique was used for fabricating magnetic metamaterials based on split-ring resonators (131). In order to get the resonance wavelength down to NIR/Vis range the structure requires sub-100-nm gap sizes (down to 35 nm). For such small features, *EBL*-based fabrication requires time consuming tests and careful optimization of writing parameters and processing steps, leading to relatively long overall fabrication times. In contrast, the rapid prototyping of complete structures can be achieved via *FIB* writing. In fact, although the E-beam lithographic step is faster, with *FIB* writing the structure is ready and no further post-processing steps are required. However, due to the low throughput, *FIB* has certain limitation in its use for fabricating optical metamaterials. However, it should be mentioned that for some specific designs and proof-of-principle experiments, for example including nonlinear materials, *FIB* is the first choice for rapid prototyping.

Here we report on the *FIB* fabrication of "fish-net" structured metamaterial that shows a resonance in the *NIR* spectral range. The fish-net structure was previously proposed by several authors and demonstrate interesting properties for an easy design

of an effective negative index material (*NIMs*). *FEM* simulations have been used to design the optimized system and the prepared samples have been analysed by means of transmittance and reflectance measurements in order to verify the presence of the resonance.

5.1 Experimental methods

The fabrication of nano-holes array, also called "fish-net" structure requires few step of process: e-beam evaporation; spin-coating and focused ion beam lithography. A schematic illustration of the prepared structure is reported in Figure 5-1.
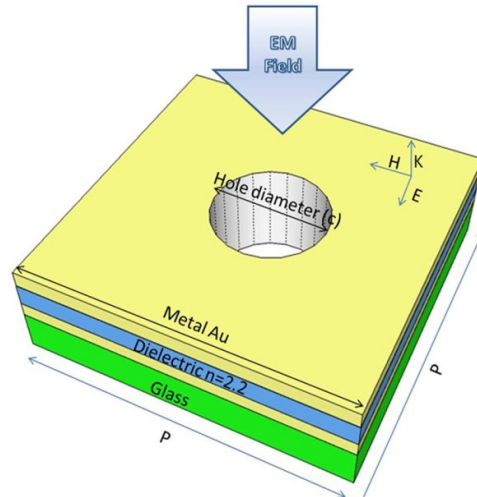

Figure 5-1. Unit cell

A suitable substrate for this metamaterial must be transparent in the spectral region of interest. A soda-lime glass covered with 110nm of ITO was used. The ITO layer ensures a good adhesion for the coatings to be prepared in a 3 layers stack. Our design comprises 30nm of Gold (Au) / 50nm of dielectric (n=2.2 ; k=0) / 30nm of Gold. Au evaporations were performed by means of e-beam, while the interlayer of dielectric was prepared via sol-gel. The film stack was then patterned by Focused Ion Beam lithography. An array of 400μm x 400μm was prepared by using an accelerating voltage of 30kV and a probe current of 28pA. The period was fixed at 780nm while two

examples of holes with diameter of 300nm and 480nm were prepared. Here we report theoretical and experimental results regarding the sample with hole's diameter 480nm. The total etched thickness is 150nm and comprise the 3 layers Au / dielectric / Au and 40nm of the base layer of ITO.

The realized structure has a theoretical resonance in the *NIR* spectral range. For both samples the *FEM* simulations show a negative refractive index at the wavelength of resonance. The complete characterization of a *NIMs* requires a not easy development of spectroscopic ellipsometry in order to measure negative refractive index (132). Here, we report preliminary experimental results where the samples characterization was performed in terms of reflectance and transmittance in order to verify the presence of the resonances shown by *FEM* simulations. The measurements have been performed by means of a WVASE spectroscopic ellipsometer by using a focusing probe.

5.2   Results and discussion

SEM micrographs reporting details of the prepared samples are reported in Figure 5-2.
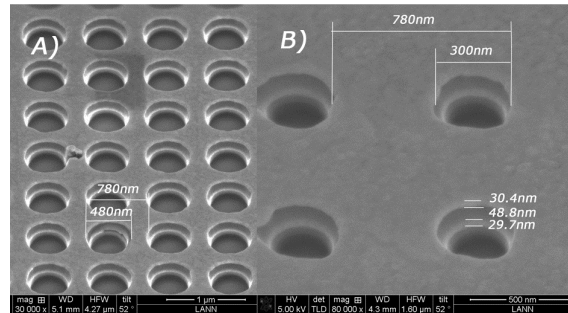

Figure 5-2. Experimental sample

In Figure 5-2a the dimension and the periodicity of the holes can be observed (sample with hole's diameter 480nm). Figure 5-2b reports the detail of the three layers structure (sample with hole's diameter 300nm). The hole through the layers shows the thickness of the Au / dielectric / Au stack and the base layer of ITO. As can be observed, good vertical walls have been obtained by using low current during the lithography process (28pA), while higher current leads to flared holes. This effect is well

known in *FIB* lithography (133). It mainly depends on the resputtering effects and on different densities of the etched materials in a multi-stack configuration. Unfortunately, this can only be partially solved by etching the holes in two steps: a first small diameter hole and a second concentric hole with the final diameter. The necessity of using a low current beam leads to very long exposure time. The $400 \times 400 \mu m$ array presented here required more than 10 hours of exposure. This represents the main limitation of the FIB technique and, as discussed above, limits its application to prototype realization.

A small patterned area leads to a measurement issue. The characterization of the metamaterial in the optical spectral range, in fact, needs to be performed by means of a suitable instrumentation. In order to illuminate the small area array, a collimated beam over an area $400 \times 400 \mu m$ is needed to be used. In Figure 5-3 the result of spectroscopic transmittance and reflectance measurements are reported.
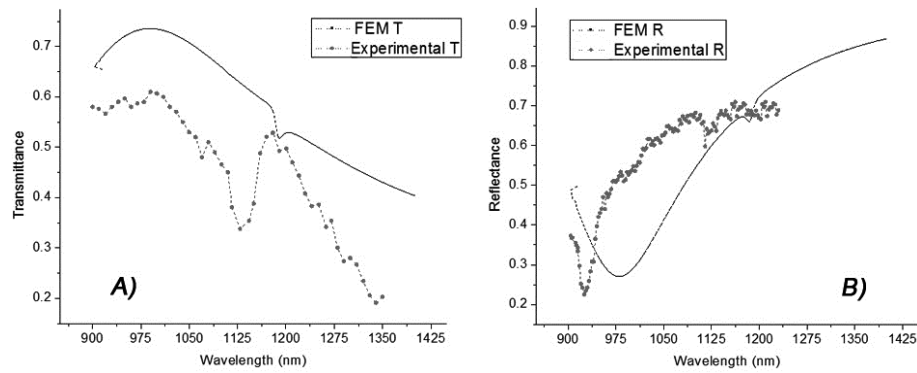

Figure 5-3. Transmittance (a) and Reflectance (b) .

These measurements have been collected by using a focusing probe optic that allows the concentration of light on $400 \times 400 \mu m$. The transmittance measurement has been performed at normal incidence (0 degree), while the minimum angle for the reflectance measurement is 15 degree. The FEM predicted curves are also reported in Figure 5-3. From this comparison it's possible to argue about the expected values of refractive index. In fact, by inverting the simulated reflection-transmission results, effective permittivity, permeability and refractive index can be obtained by a retrieval procedure

under the assumption of the homogeneity of the metamaterial (82). As mentioned before, to study the properties of the structure, a simulation of the TEM transmittance and reflectance spectra was carried out by means of COMSOL Multiphysics. Figure 5-1 depicts the layout of the simulated structure. Although two samples were prepared and characterized, here we report and discuss the case where the hole radius is r=240nm and the transverse profile of the structure has a lattice constant of 780 nm. Because of the homogeneity of the structure, for normal incidence, the electromagnetic wave with electric field vector parallel to the metallic network, visibly see a left-handed-metamaterial (LHM) slab and there is more freedom in the selection of polarization. The gold permittivity was approximated by a Drude model, $\varepsilon(\omega) = 1 - \omega_p^2 [\omega(\omega + i\gamma)]$, where ω_p is the electron plasma frequency $(1.37 \times 10^{16} \text{Hz})$ and λ is the scattering frequency $(4.08 \times 10^{13} \text{Hz})$ for bulk material at 2 μm with the exception that the scattering frequency was assumed to be 2 times that of bulk (e.g 2γ). This corresponds to additional losses in gold due to imperfections in gold including roughness, granularity and size effect. This is important in order to match the experimental results. For the dielectric layer we take n=2.2 as refractive index with negligible losses. These values derive from experimental ellipsometry measurements. Figure 5-4 reports the effective parameters extracted by the simulation.
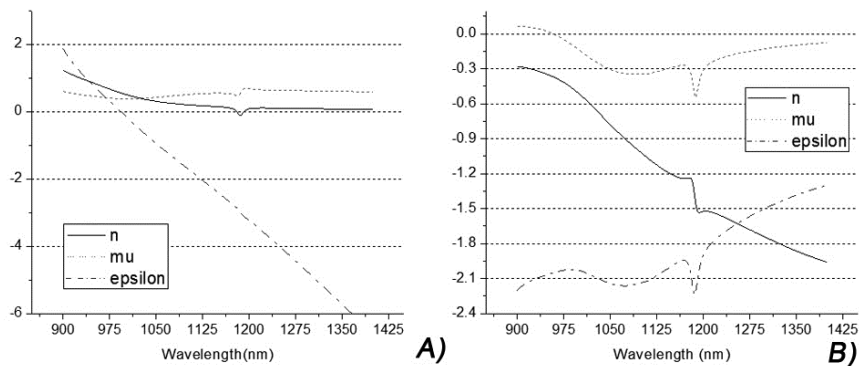

Figure 5-4. Simulated refractive index, permeability and permittivity for (a) sample A and (b) sample (B)

The experimental and simulated spectra shown in Figure 5-3 demonstrate a good match over a broad spectral range (from 900nm up to 1400nm) and include a sharp resonance feature: a magnetic resonance close to 1100 nm. The slight shift in the position of the dip between *FEM* and experimental data can be explained with the uncertainty of the value of n for the dielectric layer. Simulation provides a comprehensive explanation of the origin of the resonance observed. Field maps indicate that at 1150 nm the resonance is magnetic in origin: the electric displacement forms a loop which in turn induces an electromagnetic field opposing the incident one. In this way a *LRC* operates with 2 effective inductances (with a magnetic flux generated inside the necks and the slabs) and 2 effective capacitances (with the electric field induced by opposite charges on the opposite slabs) for each unit cell. The patterned metal layers behave as a diluted metal, providing a controllable broadband negative effective ε. In this way, achieving a negative permittivity is quite straightforward due to the metallic network. Figure 4 shows that in the proposed design the magnetic resonance should be not sufficiently strong, resulting in positive values for the effective permeability also in the case of one γ for gold loss. However the effective refractive index is seen negative at the resonance. In general the negativity of the real part of n can be accomplished either through the strong (sufficient) condition that $Re(\mu)<0$ and

$Re(\varepsilon)<0$ or through the necessary and sufficient condition $\varepsilon'\mu''+\mu'\varepsilon'' < 0$. In our case we were able to produce a single negative index metamaterial (*NIM*) which has a negative refractive index with either ε' or μ' (the permittivity in this case) being negative (but not both). In conclusion numerical simulation of the structure (the transmittance (T) and reflectance (R)) are in good qualitative agreement with optical measurements in a wide range of wavelengths. A wavelength band of single-negative operation is found where the sample exhibits NIM behavior in the infrared at 1200 nm.

5.3   Bianisotropy Fishnet metamaterial.

The present fabrication techniques for making one- to multiple-functional layer *NIM*s, include interferometric lithography (*IL*) (134), E-beam lithography (*EBL*) (135), focused ion beam (*FIB*) (115), nanoimprint (*NIL*) (136), and so on. In general, the processing procedure to fabricate the Fishnet *NIMs* is to define the hole-size using a polymetric material, usually by lithographically defining polymer posts, followed by deposition of the constitutive materials and dissolution of the polymer (liftoff processing). This processing (fabrication of posts, multi-layer deposition, liftoff) often gives rise to significant sidewall-angles (*SWAs*), resulting from continuous growth of the tops of the posts during the deposition. *NIMs* with *SWAs* are not symmetric structures, but rather are bianisotropic, exhibiting different reflectivities at normal incidence from the two sides of the film stack. This fabrication induced *SWA* effect requires a modified method to retrieve the effective parameters (84),(85) in place of the conventional approach that is appropriate only to symmetric, vertical sidewall structures (81). The *FEM* approach is used to simulate   an Ag (silver) $-$ AL$_2$O$_3$ (n=1.63) - Ag sandwich Fishnet structure with 1- and 3-functional layers (*FLs*). No substrate is present in the simulation to allow clearer demonstration of the effects of the bianisotropy. The geometrical parameters of the multi-functional layered Fishnet *NIMs* are indicated in tilted view in Figure 5-5. The orthogonal pitches of the 2D gratings p$_x$ (pitch along x-axis) and p$_y$ (pitch along y-axis) are both fixed at 300 nm. The thicknesses of Ag/AL2O3/Ag are fixed at 30/40/30 nm, respectively. The w$_x$ and w$_y$ are both fixed at 75nm. In this way the structure is independent by the incident wave polarization (in the x-y plane)
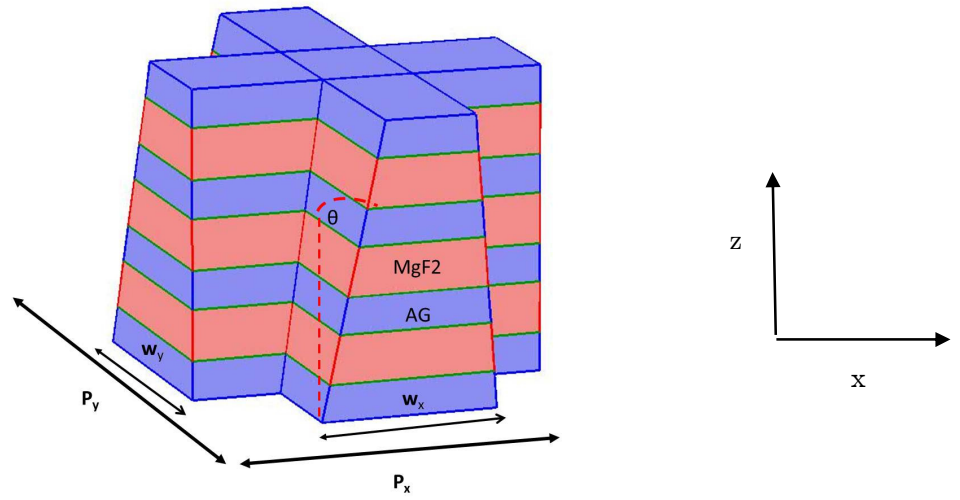
Figure 5-5 Schematic tilted view of the unit cell for 3 functional layered Fishnet NIMs with SWA with geometrical parameters.

When a TEM plane wave propagating in the z-direction as is generated in COMSOL ,the complex frequency dependent S-Parameters S_{11}, S_{12}, S_{21}, and S_{22}, can be retrieved, where the subscript 1(2) represents the waveguide port at larger (smaller) aperture. The simulated transmission $(|S_{21}|^2 = |S_{12}|^2)$, reflectances $(|S_{11}|^2, |S_{22}|^2)$ and reflection anisotropy $(|S_{11}|^2 - |S_{22}|^2)$ are plotted in Figure 5-6.

a)

b)

c)

d)

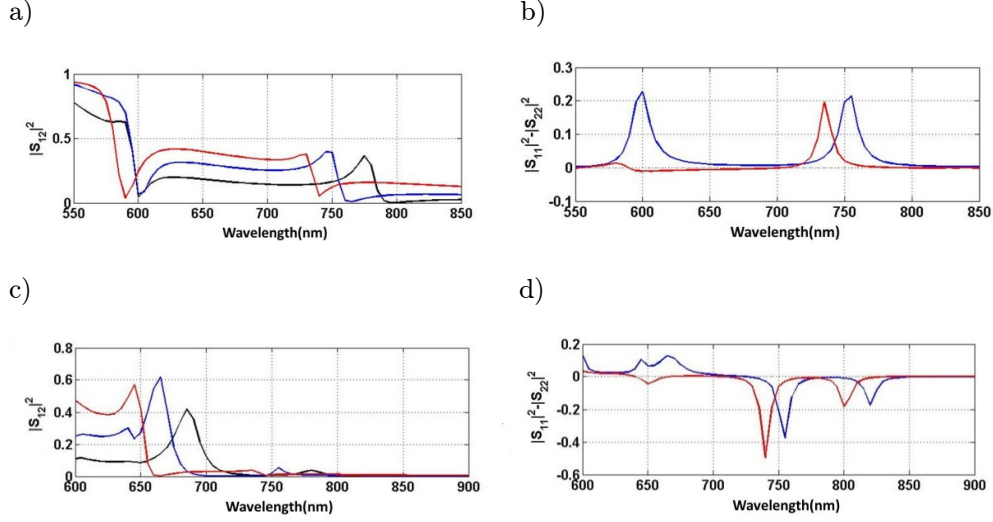**Figure 5-6 $|Sij|^2$, where i, j = port 1, port 2 for one (a),(b) and 3 (c),(d) functional layered Fishnet NIMs with SWAs (0°(black), 10° (blue),20° (red)) as a parameter using COMSOL. (a), (c) The Transmittance ($|S_{12}|^2$, $|S_{22}|^2$) ;(b),(d) Reflectivity difference $|S_{11}|^2$ - $|S_{22}|^2$.**

As just mentioned in Section 2.5, the standard retrieval method assuming isotropic constitutive parameters (ε, μ) for a symmetric structure fails if the unit cell of the NIM is not symmetric in the propagation direction as a result of the sidewall-angles induced during fabrication. In case of a NIM with *SWAs*, the S-Parameters, especially S_{11} and S_{22} are different depending on the propagation direction of incident light with respect to the unit cell ($S_{11} \neq S_{22}$, S21 = S12), e.g. the structure exhibits inhomogeneous asymmetry or bianisotropy [21]. The constitutive relations for Fishnet structured NIMs with SWA-induced bianisotropy in the *x-y* plane have been just presented in Section 2.5. In particular Eqs. 2.33, 2.36 have been employed for numerical calculations. Structures with different *SWAs* were modelled to investigate the effect of the *SWA* on the strength and position of the effective parameters-effective refractive index, permeability and permittivity. For 1 and 3 functional layers, the wavelength at the minimum value of $Re(\mu_{eff})$ decreases as the *SWA* increases as shown in Figure 5-7b,d. This tendency can be qualitatively interpreted by the magnetic resonance of an

94

equivalent *LC* circuit: a larger SWA corresponds to smaller capacitance and inductance (137), which in turn leads to a shorter resonance wavelength.
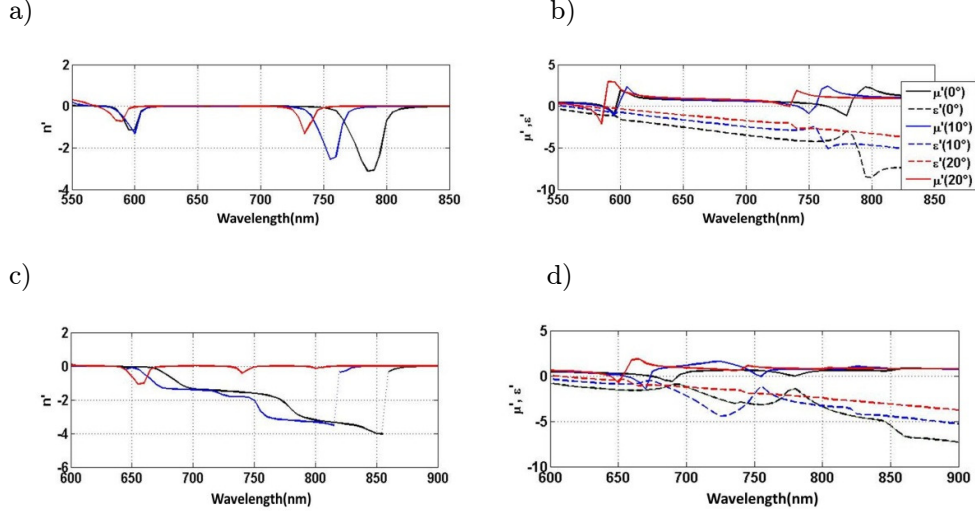

Figure 5-7. Real parts of the effective parameters (n, μ and ε) for one-(a,b) and three-(c,d) functional layered Fishnet NIMs with SWAs (0°(black), 10° (blue), 20°(red)) using the modified retrieval equation. (a),(c) shows Re[n_{eff}] and (b),(d) shows Re[μ_{eff}] and Re[ε_{eff}].

The magnitude of negative refractive index in *NIMs* with 1 *FL* depends on the sidewall-angle, that is, the minimum value of $Re(n_{eff})$ increases as the *SWA* increases as shown in Figure 3-7a. The reason for the increase is clear: as the sidewall-angle increases, the absolute values of $Re(\varepsilon_{eff})$ decreases (as shown in Figure 5-7b,d) due to the decrease of the Ag line-width along the direction of electric field. The wavelength at the minimum of $Re(n_{eff})$] decreases with increase of sidewall-angle, which is a result of the blue-shifted resonance peaks of both $Re(\varepsilon_{eff})$ and $Re(\mu_{eff})$. Also, the blue-shifted resonance frequency of effective permittivity and permeability as mentioned above accounts for decrease of the wavelength at minimum effective refractive index in multi-functional layered NIMs with the increase of the side-wall angle. Moreover Figure 5-8

shows that the bi-anisotropic parameter ξ_0 for multiple functional layered Fishnet NIMs as a function of the sidewall-angle.
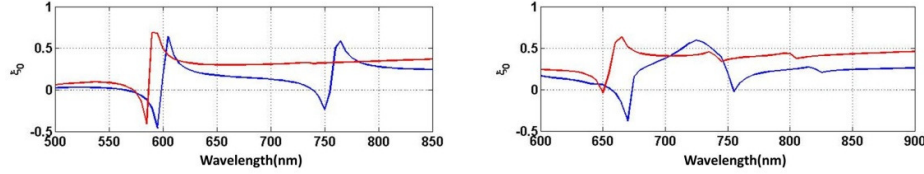

Figure 5-8. Real and imaginary parts of the bi-anisotropic parameter (ξ_0) for one- (left) and to five (right) functional layered Fishnet NIMs with SWAs (10° blue),20° (red)).

As shown in Figure 5-7d the wavelength of the minimum value of $Re(\mu_{eff})$ is linearly dependent on the *SWA*. The trend of a decreasing minimum value of $Re(\mu_{eff})$ can be explained as a more complicated coupling between magnetic and electric dipoles. In an ideal Fishnet structured *NIM* with vertical sidewalls the bianisotropic parameter ξ_0 for Fishnet NIMs with zero sidewall-angle is identically zero, independent of number of functional layers. The structure is composed of independent electric atoms and magnetic atoms: the electric response results from the array of thin metal wires parallel to the electric field direction and the magnetic response from pairs of metal stripes separated by a dielectric spacer along the direction of magnetic field that support an anti-symmetric current as shown in Figure 5-9. However, in realistic Fishnet structured *NIMs* with a fabrication-induced side wall angle, the *NIMs* are bianisotropic (138). In the thin metal wires (electric response), a magnetic dipole in the *x*-direction is induced by an electric field $\boldsymbol{E}$ in the y-direction, resulting from the disparity of the current distribution in the two metal films, so the magnetic and electric dipoles induced by $\boldsymbol{E}$ are coupled to each other. Similarly, the electric dipoles induced by $\boldsymbol{H}$ (magnetic loop response) now include a net *y*-component, so the electric and magnetic dipoles induced by $\boldsymbol{H}$ are also mutually coupled as shown in Figure 5-9.

a)
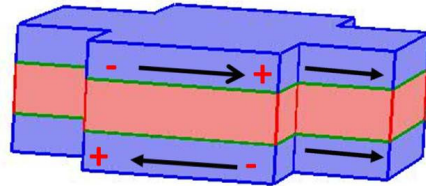
b)
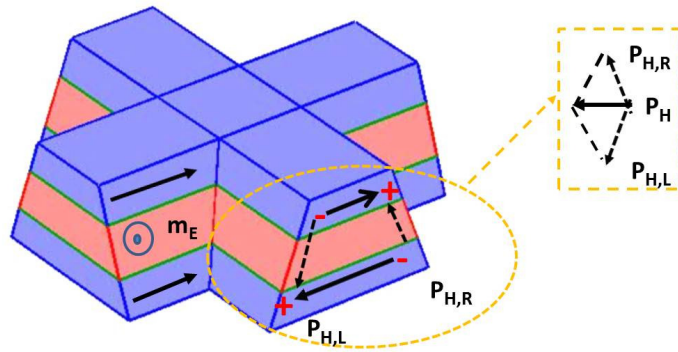
Figure 5-9. Schematic depicting the electric and magnetic dipoles in an ideal Fishnet structure (SWA= 0°) and a realistic Fishnet structure with a fabrication-induced sidewall-angle (SWA ≠ 0°). (a) Electric/magnetic dipole induced by electric/magnetic field, respectively. (b) Electric dipole response, indicated by the two rightmost arrows, also induces a magnetic dipole (m_E) due to the unbalanced current distribution in the two plates. The magnetic dipole response, asymmetric current loop, also induces an electric dipole (P_H) in the metamaterial plane given by the vector sum of the two induced polarizations.

5.4   Conclusion

Focused-ion beam lithography has been used to prepare prototypes of simple and effective metamaterial structures well known as "fish-net". These structures

97

theoretically exhibit a band of negative refractive index at optical frequencies and reduces the selection of the polarization direction of electromagnetic wave. The prepared samples were characterized by means of spectroscopic ellipsometry in terms of transmittance and reflectance measurements. Numerical simulation of the structure (the transmittance (T) and reflectance (R)) are in good qualitative agreement with optical measurements in a wide range of wavelengths although a shift in the position of the peak was observed. A wavelength band of single-negative operation is expected where the sample exhibits *NIM* behavior in the infrared at 1200 nm. Moreover an analytic approach has been presented in order to calculate the effect of bi-anisotropy induced by fabrication, which appears not negligible in order to improve the accuracy of the extracted effective parameters.

6   Complex dispersion curve calculation by means of FEM

The numerical simulation of electromagnetic fields inside both metamaterial and photonic crystals is an important tool for analyzing these periodic structures. In particular, the eigen-modes of crystals, defined as freely propagating waves not coupled to external currents, are often of the most interest. The conventional method (139), (140) of numerically solving for crystal eigen-modes is to define the geometry of the unit cell of the crystal of interest and the differential equation that the fields must obey in this geometry and then impose Bloch periodic boundary conditions. The partial differential equation problem is then discretized using one of the many standard methods (finite element, finite integral, finite difference, etc.) thereby turning it into an algebraic eigenvalue problem with a finite number of degrees of freedom and the frequency ω as the eigenvalue. The band structure of the photonic crystal, $\omega(\mathbf{k})$ is then obtained as a function of the crystal momentum $\boldsymbol{k}$. When material dispersion plays a crucial role, as in the case of metal nanostructures, the resulting eigenvalue equation is nonlinear (141). Besides time consuming brute force methods (142) , involving non-linear iterative solvers, other methods have been proposed to solve such kind of problems, which are based on the solution of Helmholtz's equation considering the wave vector as eigenvalue instead of the frequency (obtaining therefore the bands as $\mathbf{k}(\omega)$) (143), (144), (145), (146), (147), (148). Generally these methods end up with a much more tractable quadratic eigenvalue equation in $\boldsymbol{k}$, which is can be solved by proper linearization procedures (147). Moreover the imaginary part of $\boldsymbol{k}$ as well as the real one is naturally retrieved. In a recent work Fietz et al. (148) showed a modal analysis method based on reformulation of the eigenvalue equation in weak form, which enables to obtain a quadratic eigenvalue equation in $\boldsymbol{k}$. This formulation of the problem finds then natural solution in the frame of Finite Elements Methods, which inherently handle weak forms of partial differential equations. The method, originally developed

by Hiett et al. (146), demonstrated to be very powerful since it allows to deal with completely general materials, dispersive, lossy and possibly anisotropic.

Here we present the method and its potential application to 2D and 3D plasmonic-crystal slabs. In the next chapter we'll extend the application to a full periodic metamaterial Fishnet showing the complex bands for its least-damped modes.

6.1   The FEM simulation

The aim of the present section is to briefly revisit the FEM weak formulation of Helmholtz's eigenvalue equation presented in (148) keeping the treatment sufficiently general in roder to handle problem invonvilng anisotropic dispersive lossy material dielectric constants. Maxwell equations for time harmonic fields E(x,t)=E(x)exp(-jωt), H(x,t)=H(x)exp(-jωt) are

$$\nabla \times \mathbf{E} = -j\omega\hat{\mu}\mathbf{H}$$
$$\nabla \times \mathbf{H} = j\omega\hat{\varepsilon}\mathbf{E}. \tag{6.1}$$

Here $\hat{\varepsilon}(\omega)$ and $\hat{\mu}(\omega)$ are the microscopic permittivity and permeability tensor of the plasmonic structure. These two equations can be recast in the following general wave equation

$$\nabla \times \left(\hat{p}\nabla \times \mathbf{V} \right) - \omega^2 \hat{q}\mathbf{V} = 0, \tag{6.2}$$

where $\mathbf{V} = \mathbf{E}$, $\hat{p} = 1/\hat{\mu}$, $\hat{q} = \hat{\varepsilon}$ for the magnetic formulation and $\mathbf{V} = \mathbf{H}$, $\hat{p} = 1/\hat{\varepsilon}$, $\hat{q} = \hat{\mu}$ for the electric formulation. For a structure periodic in the x, y, z-directions, the problem reduces to finding Bloch waves solutions (Bloch theorem (149)) of the form:

$$\mathbf{V}(x, y, z\ ;\mathbf{k}) = e^{-i\mathbf{k}\cdot\mathbf{r}}\mathbf{u}(x, y, z) = e^{-i(k_x x + k_y y + k_z z)}\mathbf{u}(x, y, z). \qquad (6.3)$$

According to the Minimum Theorem (149) by substituting Eq. (6.3) in Eq. (6.2), the vector function $\mathbf{V}$ minimizes an energy-related functional or weak expression, given by (148)

$$F(\mathbf{v},\mathbf{u}) = \hat{p}\left[k^2(\mathbf{v}\cdot\mathbf{u}) - (\mathbf{k}\cdot\mathbf{v})(\mathbf{k}\cdot\mathbf{u})\right] - i\hat{p}\mathbf{v}\cdot\left[\mathbf{k}\times(\nabla\times\mathbf{u})\right] - i(\nabla\times\mathbf{v})\cdot\hat{p}(\mathbf{k}\times\mathbf{u}) +$$
$$+ (\nabla\times\mathbf{v})\cdot\hat{p}(\nabla\times\mathbf{u}) - \hat{q}\frac{\omega^2}{c^2}\mathbf{v}\cdot\mathbf{u} + \nabla\cdot\left[\hat{p}(\mathbf{k}\times(\mathbf{u}\times\mathbf{v}) + \nabla\times(\mathbf{u}\times\mathbf{v}))\right], \qquad (6.4)$$

where $\mathbf{v}(\mathbf{r})$ is a test function and we considered the following vector identity $\nabla\cdot(\mathbf{a}\times\mathbf{b}) = (\nabla\times\mathbf{a})\cdot\mathbf{b} - \mathbf{a}\cdot(\nabla\times\mathbf{b})$. Integrating both sides on the unitary cell volume and applying the divergence theorem to the last term in Eq. (6.4) yields

$$\int_\Omega d^3\mathbf{r} F(\mathbf{v},\mathbf{u}) =$$
$$\int_\Omega d^3\mathbf{r}\left(\hat{p}\left[k^2(\mathbf{v}\cdot\mathbf{u}) - (\mathbf{k}\cdot\mathbf{v})(\mathbf{k}\cdot\mathbf{u})\right] - i\hat{p}\mathbf{v}\cdot\left[\mathbf{k}\times(\nabla\times\mathbf{u})\right] - i(\nabla\times\mathbf{v})\cdot\hat{p}(\mathbf{k}\times\mathbf{u})\right) + \qquad (6.5)$$
$$+ \int_\Omega d^3\mathbf{r}\left((\nabla\times\mathbf{v})\cdot\hat{p}(\nabla\times\mathbf{u}) - \hat{q}\frac{\omega^2}{c^2}\mathbf{v}\cdot\mathbf{u}\right) + \int_{\partial\Omega} dA\mathbf{v}\cdot\left[\hat{\mathbf{n}}\times\hat{p}(-i\mathbf{k}\times\mathbf{u} + \nabla\times\mathbf{u})\right] = 0,$$

where we use the scalar triple product for the surface term of Eq.(6.5). The last integral is over the boundary of the domain and represents a natural boundary

101

condition (148). Eq.(6.5) can be interpreted as an eigenvalue problem in weak formulation and solved for the Bloch wavenumber $\mathbf{k}$. In order to turn Eq. (6.5) into an eigenvalue problem the three degrees of freedom that comprise the Bloch wave-vector $\boldsymbol{k}$ must be reduced to one by restricting two degrees of freedom. This is accomplished by setting $\mathbf{k} = \mathbf{k}_0 + \lambda \hat{\mathbf{k}}_n$ where λ will be the eigenvalue solved for, $\mathbf{k}_0$ is an offset vector and $\hat{\mathbf{k}}_n$ is a unit vector $(\hat{\mathbf{k}}_n \cdot \hat{\mathbf{k}}_n = 1)$ that defines the direction of the complex wave-number eigenvalue λ. This integral-differential equation may be transformed into matrix format by following the usual finite element method discretization: the domain is divided into several tetrahedral subdomains (elements) in which locally supported expansion functions are defined, $\mathbf{u}$ is expanded in terms of such functions within each element, and $\mathbf{v}$ is taken to be each one of the local expansion functions inside each element. Then the following matrix eigenvalue equation in λ (148):

$$\hat{A}\mathbf{u} + \lambda\hat{B}\mathbf{u} + \lambda^2\hat{C}\mathbf{u} = \mathbf{0} \tag{6.6}$$

where A, B and C are N×N matrices and $\mathbf{u}$ is an N×1 solution vector. N is the number of degrees of freedom of the discretized system. This quadratic eigenvalue problem can be recast in the form of a generalized eigenvalue equation

$$\begin{pmatrix} \hat{A} & \hat{B} \\ 0 & 1 \end{pmatrix}\begin{pmatrix} \mathbf{u} \\ \lambda\mathbf{u} \end{pmatrix} = \lambda\begin{pmatrix} 0 & -C \\ 1 & 0 \end{pmatrix}\begin{pmatrix} \mathbf{u} \\ \lambda\mathbf{u} \end{pmatrix}. \tag{6.7}$$

The eigenvalue equation may be solved at at fixed frequency ω (and thus fixed $\varepsilon(\omega)$) and $\mathbf{k}$-vector direction. The eigenvalue itself is the k-vector amplitude λ.

The presented weak formulation of the eigenvalue problem is inherently handled by Finite Elements solution procedure. All the models and examples in this paper have been performed and calculated with COMSOL Multiphysics, which allows the user to

specify the field equation to be solved. The *FEM* software turns the weak form, Eq.(6.1.5), with accompanying boundary conditions into the algebraic problem Eq. (6.1.7) For more details about the FEM approach we remand to Ref. (87), (150). In the following we adopt the magnetic formulation ($\mathbf{V}=\mathbf{H}$, $\hat{p}=1/\hat{\varepsilon}$, $\hat{q}=\hat{\mu}$). This simplifies treatment of SPPs which can only exist in TM polarization. However, for periodic structures solving for the magnetic field is equivalent to solving for the electric field. The spatial profile of the eigenmode $\mathbf{u}(\mathbf{x})$ is also recovered providing the magnetic field profile according to Eq. (6.1.3) with ($\mathbf{V}=\mathbf{H}$) and the electric field profile according to

$$\mathbf{E}(\mathbf{x}) = \frac{1}{i\varepsilon\omega / c}\nabla \times \mathbf{H} = \frac{1}{i\varepsilon\omega / c}\left(-i\mathbf{k}\times \mathbf{u}+ \nabla \times \mathbf{u}\right)\exp(\mathrm{i}(\omega\mathrm{t}\text{-}\mathbf{k}\cdot \mathbf{x}) \qquad (6.8)$$

6.1.1   The boundary conditions

On an external boundary, the natural boundary condition enforced by the integral in Eq. (6.5) over the boundary $\partial\Omega$ forces the expression $(-i\mathbf{k}\times \mathbf{u}+ \nabla \times \mathbf{u})/\varepsilon$ to be equal to zero. Recalling Eq. (6.8) this simply enforces the boundary condition $\hat{\mathbf{n}}\times \mathbf{E} = 0$. This is known as the perfect electric conductor or PEC boundary condition. This natural boundary condition is the default if no other boundary condition is enforced. The PEC condition is also equivalent to the zero flux $(-\mathbf{n}\cdot \text{flux}=0)$ condition or Neumann condition (87). On an internal boundary within the unit cell the surface integrals over each side of the boundary must be equal to each other. The effect is that the tangential components of the electric field must be continuous across the internal boundary or $\hat{\mathbf{n}}\times \mathbf{E}^{+} = \hat{\mathbf{n}}\times \mathbf{E}^{-}$ where $\mathbf{E}^{+}$ and $\mathbf{E}^{-}$ are the electric fields on opposite sides of the internal boundary. The periodicity of $\mathbf{u}$ is enforced by imposing periodic boundary conditions on the exterior boundaries of the unit cell. In COMSOL, these periodic boundary conditions override the natural. boundary condition. On the other hand if a Perfect Magnetic Conductor or PMC boundary condition ($\hat{\mathbf{n}}\times \mathbf{H} = 0$) is desired while solving for the magnetic field, this can be enforced with constraints (87)

on the tangential magnetic field on the boundary. In COMSOL this correspond to a Dirichlet boundary condition. The condition $\hat{\mathbf{n}} \times \mathbf{H} = 0$ can be expanded into three scalar expressions as

$$n_x E_y - n_y E_x = 0, \quad n_y E_x - n_z E_y = 0, \quad n_z E_x - n_x E_z = 0 \tag{6.9}$$

Where n_x, n_y and n_z are the components of the normal to the conducting surface $\left(\hat{\mathbf{n}} = n_x \hat{x} + n_y \hat{y} + n_z \hat{z} \right)$. Once this is done, a nonzero component, say n_z can be used to eliminate the other two components:

$$E_x = \frac{n_x}{n_z} E_z, \quad E_y = \frac{n_y}{n_z} E_z, \tag{6.10}$$

consistently with the fact that only one field component can be independent at the surface of a perfect conductor.

6.2   Plasmonic Chrystal slab

Periodic metallic nanostructures have received great attention in recent years due to their surprising optical properties. The interaction of electromagnetic fields with the free electron gas of metals gives rise to particular electromagnetic field waves which are known as Surface Plasmon Polaritons (SPPs). Due to their properties of extreme light confinement and sensitivity to the dielectric environment, *SPPs* have found lots of interesting application in the fields of sensing (151), thin film photovoltaics (152), near field imaging (140), waveguides (153) etc.

In particular, periodically nanostructured metal-dielectric interfaces have been subject of many researches due to their unexpected optical properties such as Extraordinary Optical Transmission (125) and negative refraction (154) . Surface Plasmons propagation across such structures exhibits analogous properties of light propagation in dielectric photonic crystals (140). A complicated system of band gaps has indeed been calculated and measured using different metallic gratings and bi-gratings (140). Shallow surface features can be assigned an effective refractive index

describing their interaction with SPP, thus enabling a complete analogy with 2D photonic crystals. The description of Plasmonic Bloch waves propagating in a plasmonic crystal slabs, however, is a much more challenging task with respect to the description of photonic Bloch waves in fully periodic dielectric systems.

The treatment of Photonic Crystal *Slabs* (PCS), however, requires proper handling of not only truly bound modes but also of *leaky* modes. This term addresses eigen-modes whose crystal momentum lies inside the light cone. In these cases the mode can couple to waves propagating in the semi-infinite half space resulting in radiative losses (3). Simulation of open space boundaries is a tricky task both for methods based on discretization of real space (like Finite Elements and Finite Differences) as well as for methods suited for fully periodic structures (like Plane Wave Expansion method). A common approach introduces a fictitious periodicity in the direction normal to the slab (Super-cell approach (155),(3)). The period is chosen sufficiently large in order to decouple the bound modes of the slabs. However, the artificial periodicity produces many spurious modes and moreover it perturbs the physical eigen-modes profile and it requires much computational time (because of the large super-cell size necessary for decoupling of modes). Plane Wave Expansion Method has been extended by Shi and coworkers (145) including Perfectly Matched Layers (PMLs) which correctly absorbs leakage radiation. These layers are characterized by a slowly space varying relative permittivity and permeability, properly designed in order to minimize reflection of plane waves impinging on them at arbitrary incidence. The method can deal with photonic crystal slabs with arbitrarily dispersive materials but only in case of absence of losses, excluding therefore the important class of plasmonic crystal slabs. Other methods, based on *FDTD* can handle the lossy dispersive problem but are computationally very expensive (156). To our knowledge, a complete and efficient numerical treatment of metallic planar crystals still lacks.

In this paper we adopt the weak formulation of the Helmholtz's eigenvalue equation, which allows to solve the problem with wave vector as eigenvalue, adding PMLs to correctly deal with leaky modes radiation. The method is compared to

scattering FEM simulations, which serve as test tool for the accuracy and reliability of the method.

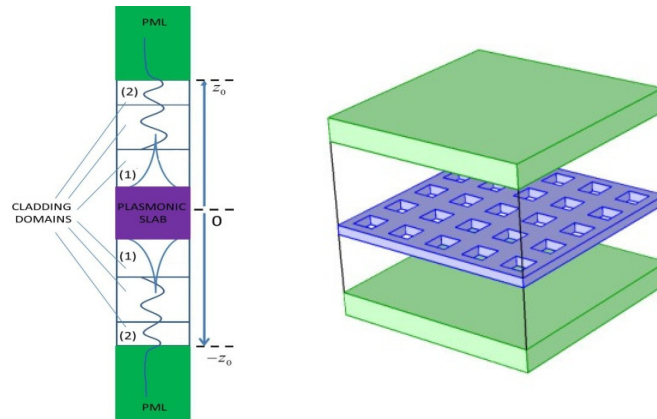## 6.2.1 The perfect matched layer (PML) implementation

Figure 6-1. Scheme of photonic crystal slab (violet) with PMLs truncating the computational domain (green).

A photonic crystal slab (PCS) is a photonic crystal with two-dimensional periodicity but a finite thickness along the third spatial dimension (156),(3), as depicted in Figure 6-1. As mentioned before, the modal analysis of a PCS requires proper truncation of the computational domain in the direction normal to the slab. Such a truncation may be performed introducing the so-called Perfectly Matched Layers within the unitary cell, above and below the PCS (Figure 6-1), whose function is to absorb light coming from the slab, for any frequency and angle of incidence.

As proposed by Sacks et al (157), (158), a PML can be treated as an anisotropic absorber in which the permittivity and permeability tensors are modified according to the following (158),(159)

106

$$\hat{\varepsilon} = \varepsilon\hat{\Lambda}, \ \hat{\mu}=\mu\hat{\Lambda}, \tag{6.11}$$

with

$$\hat{\Lambda} = \begin{pmatrix} a & 0 & 0 \\ 0 & b & 0 \\ 0 & 0 & c \end{pmatrix}. \tag{6.12}$$

Where, in case of absorption in the third direction,

$$a = b = \frac{1}{c}. \tag{6.13}$$

This condition assures perfect absorption of any plane wave incident upon the PML boundary, independently of frequency or incidence angle (159). The most general form for the $\hat{\Lambda}$ tensor is than

$$\hat{\Lambda} = \begin{pmatrix} \alpha - j\beta & 0 & 0 \\ 0 & \alpha - j\beta & 0 \\ 0 & 0 & 1/(\alpha - j\beta) \end{pmatrix}. \tag{6.14}$$

We impose $\alpha = 1$ in order to match the PML domains with the adjacent air domains while

$$\beta = \bar{\sigma}\frac{\left|(z \pm z_0)\right|^n}{L^n}. \tag{6.15}$$

In Eq.(6.15) $\bar{\sigma} = \sigma/\omega$, L and n are free constant parameters. The plus (minus) sign refers to *PML* along negative (positive) z-directions respectively. L is the PML thickness while $\bar{\sigma}$ is the wave attenuation rate in PML. Condition (6.15) assures a smooth increasing of the damping rate of waves incoming into the absorbers. The

discrete approximation of fields and material parameters results in a spurious impedance loading at the interface (159). This mismatch problem in the discrete space can be tempered by using spatially varying material parameters (159). Optimal PML performance, however, requires a careful optimization of parameters σ and L and n. The problem will be addressed in next sub-section.

6.2.2 2D sinusoidal grating and PML test

We want to demonstrate the effectiveness of the method outlined in previous sections in extracting the complex $\mathbf{k}(\omega)$ dispersion curves of 2D and 3D planar metallic periodic structures. We first start with the 2D example depicted in Figure 6-2 left.

The unit cell consists of a sinusoidal metal-dielectric interface in the plane x-y, infinitely extended in z-direction (out of plane). In y-direction the unitary cell is limited above by a *PML* layer and below by the bulk silver. The period in x-direction is set to 600nm while the peak-valley amplitude of the sinusoids is increased from 0 to 150nm. We adopt silver as bulk metal, its permittivity being taken from Palik (159). Periodic boundary conditions are set in both x- and y-directions. In y-direction this condition is not mandatory because of the presence of the *PML*. This choice is made in order to reduce to zero the last term in Eq. (6.5).

In case of mono-periodic gratings like the example considered, one is typically interested in studying surface plasmon modes whose $\mathbf{k}$-vector is parallel to the grating vector, $\mathbf{G} = \hat{k}_x(2\pi/d)$. In this case the weak form of Helmholtz's equation, Eq.(6.5), reduces to the following simplified form

$$\int_\Omega d^2\mathbf{r} \left[\lambda^2 \frac{uv}{\varepsilon_{22}} + \lambda \frac{i}{\varepsilon_{22}} \left(\frac{\partial u}{\partial x} v - u \frac{\partial v}{\partial x} \right) + \frac{\partial u}{\partial y} \frac{\partial v}{\partial y} \frac{1}{\varepsilon_{11}} + \frac{\partial u}{\partial y} \frac{\partial v}{\partial y} \frac{1}{\varepsilon_{22}} - \left(\frac{\omega}{c} \right)^2 uv\mu_{33} \right] = 0. \quad (6.17)$$

where $\lambda = k_x$, ε_{ii} and μ_{ii} are the diagonal components of the relative permittivity and permeability tensors.
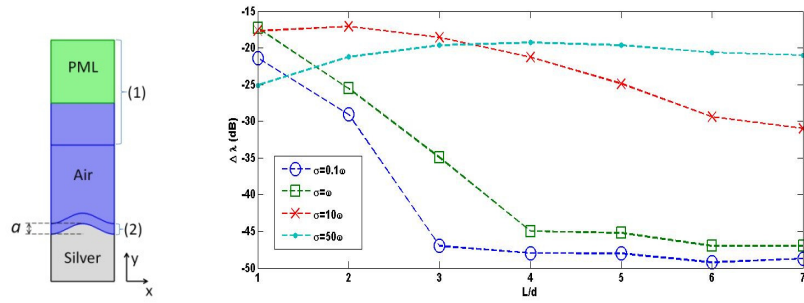
Figure 6-2. Parametric variation of tensor constants. $\Delta\lambda$ represents the variation of λ respect to the previous calculated λ value relative to the previous L/d value at several fixed σ.

The necessity of terminating the computational domain with proper boundary condition, in any case, results in the generation of undesired spurious modes after each solution stage. Most of these nonphysical modes look like guided modes within the *PML* domains or between slab and absorbing boundary. A common way to discriminate physical leaky or bound modes from *PML* modes is to employ an average field intensity based filter (145). The physical modes, even leaky modes, are expected to be those ones mostly confined in proximity of the plasmonic slab and rapidly decaying within the PML domain. We calculated the following quantity for every eigen-mode

$$\kappa = \frac{\left\langle \left|\mathbf{H}\right|^2 \right\rangle_{(1)}}{\left\langle \left|\mathbf{H}\right|^2 \right\rangle_{(2)}} \tag{6.18}$$

where $<|\mathbf{H}|^2>_{(1)}$, $<|\mathbf{H}|^2>_{(2)}$ are the averages of the $\mathbf{H}$ field norm in a region far from the grating and within a thin air layer (tens of nm) close to the metal surface respectively (see Figure 6-1). We found out that κ values ranging from 0 to 20% are typically calculated in case of physical bound or leaky eigen-modes, while higher values are found for nonphysical *PML*–related mode. We used therefore the quantity κ to filter out non-physical modes.

109

Before extracting the dispersion curves we performed a *PML* test in order to appropriately set the constants σ, *L* and *n* in the *PML* model, Eq. (6.15). In Figure 6-2 we report the variation of λ for several *PML* thicknesses and σ, keeping fixed frequency, *n* and mesh element density. As can be seen, *PML* performances improve with increasing *PML* thickness and decreasing σ. This can be explained as follows: the variation in λ is related to non-zero reflections at the interface between *PML* and air. As mentioned previously, *PML* is perfectly reflectionless only when solving the exact wave equation. Reflections keep small as long as the discretization is a good approximation of the exponentially decaying wave within the *PML*, provided the *PML* is thick enough to completely absorb the incoming wave. Two methods are possible in order to increase the accuracy of the approximation: (a) for a fixed *PML* thickness, increasing mesh element density in the *PML* or, (b), for a fixed mesh element density, turning on wave absorption more and more slowly decreasing σ parameter, while increasing PML thickness. Clearly option (b) works since, as long as the *PML* material is slowly varying, the wave decay is more diluted in space and is better resolved by the given mesh density. Of course both options (a) and (b) require increasing the number of elements within the *PML* domain. An acceptable compromise between accuracy and computational cost was found taking the PML thickness *L* equal to $4d$ and the σ value close to ω, keeping the mesh density the same as in the air domain.

With regard to the *n* parameter, experience shows (160) that a simple quadratic or cubic turn-on of the *PML* absorption usually produces negligible reflections for a *PML* only few wavelengths thick.

Once set the tensor parameters in Eq.(6.15) we performed the modal analysis of the structure in Figure 6-2. In Figure 6-3 we show a reflectance map obtained by a scattering *FEM* simulation of a grating with amplitude 75nm. This kind of maps is commonly used in literature to deduce the real part of *SPP* modes dispersions by looking at the reflectance dips (126), (161). Black lines are the real part of the *SPP* modes calculated with the modal analysis. As can be seen, the modal analysis correctly predicts the dips observed in the reflectance maps, which correspond to coupling of

impinging light to *SPP* modes. Of course the modal analysis offers more information: the dispersion curves are now complex and they extend outside of the light cone.
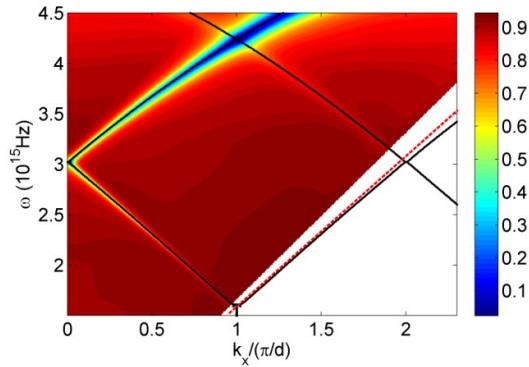

Figure 6-3. Reflectance map compared with the calculated dispersion curves (black lines). Red dashed line is the light line.
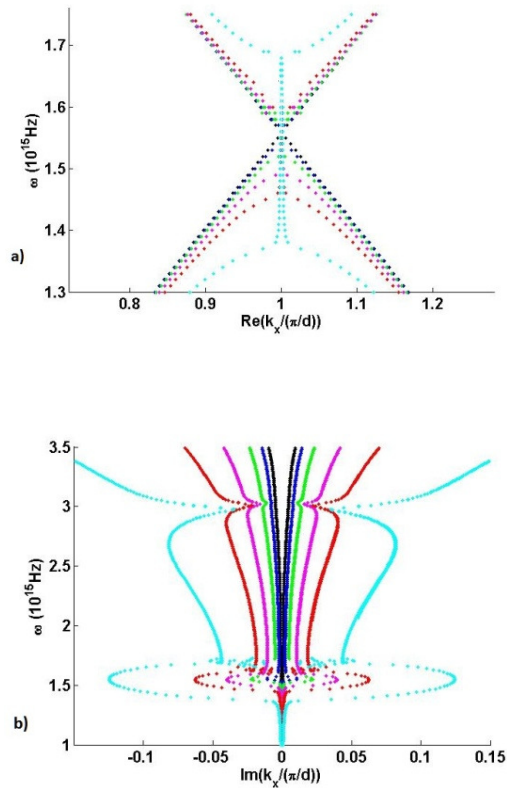

Figure 6-4. Real part a) and imaginary part b) of the modes varying the hole size, a: a=0 black, a=30nm blue, a=50nm green, a=75nm magenta, a=100nm red, a=150nm cyan.

In Figure 5a it is reported real part of mode dispersion at the edge of first Brillouin zone for increasing grating amplitudes. As well-known (126), the flat metal interface sustains a SPP wave whose dispersion is given by $k_{SPP,F} = k_0 (\varepsilon_m \varepsilon_d / (\varepsilon_m + \varepsilon_d))^{1/2}$. When a shallow periodic perturbation is introduced the mode dispersion remains close to the flat case dispersion. The only remarkable difference with respect to the flat case is seen at the edge of first Brillouin zone, where an energy gap is rapidly established with increasing grating depth (162). In general, energy gaps occur at the crossing points of the flat metal inferface SPP dispersion curves, i.e. at the edge and at the center of first Brillouin zone ($k_x = \pi / d$ and $k_x = 0$ respectively). When ω increases, starting from zero, the first crossover defines the so-called first order stop band (162), which corresponds to the coupling of two counter-propagating surface waves. As discussed in Ref. (162) for the case of lossless metal gratings, if a surface mode propagates on a corrugated surface whose grating wave vector $G = 2\pi / d$ is twice the mode wave vector, this results in the formation of a standing wave pattern. For symmetry reasons, the mode field distribution on the surface may then take only two alternative configurations, having different energies. The two standing wave patterns take different positions with respect to the peaks and troughs of the grating. The low frequency solution concentrate its energy around the grating peaks (high effective permittivity region) while the high frequency solution concentrate its energy in the troughs of the grating (low effective permittivity region). This situation is analogue to the band gap formation in case of 1D photonic crystals (3). It is worth noting in Figure 6-4a that the modal method converges to a solution also at frequencies within the band gap. In particular the band, at frequencies close to the lower gap edge, rises steeply through a continuum of states toward the upper gap edge, reaching the value $k_x = \pi / d$ only in one point. The gap edges are actually not well defined, especially for higher amplitude gratings. This behavior was already noticed in similar modal analyses performed with real frequency and complex Bloch wave vector. The frequency gap however is more evident looking at the imaginary part of the mode dispersions (Figure 6-4b). At frequencies corresponding to the energy gap the imaginary part assumes great values, reaching a maximum at the centre of the gap. The phenomenon becomes more evident

with increasing grating depths, as expected. The mode in this frequency range has a great dissipation which prevents it to propagate in the groove direction, thus it is sometimes referred as gap-like mode

For frequencies above the upper gap edge ($\omega > 1.7\text{x}10^{15}\text{Hz}$) the imaginary part of the Bloch wave vector has values much greater than for frequencies below the gap. This is because the folded plasmonic band enters the light cone and radiative copling to propagating waves in the upper air half space becomes possible. In Figure 6-5 we show the z-component of the eigen-mode magnetic field at a frequency of $\omega = 2.5\text{x}10^{15}\text{Hz}$ for grating amplitudes of 0, 30 and 100nm. In the flat case, the mode is a guided eigen-mode of the metal-dielectric interface and is perfectly confined (Figure 6-5a). As already pointed out, for small grating depths, the *SPP* wave vector is only slightly perturbed with respect to $k_{SPP,F}$. In this situation the mode remains well confined as in the flat case and the main damping is due to losses in metal (see Figure 6-5b). The mode confinement decreases with increasing the grating amplitude, and stronger leakage radiation is observed (see Figure 6-5c). It is worth noting how the leakage radiation is perfectly exponentially decaying when crossing the *PML* domain (see Figure 6-5d) with almost zero spurious back reflections.
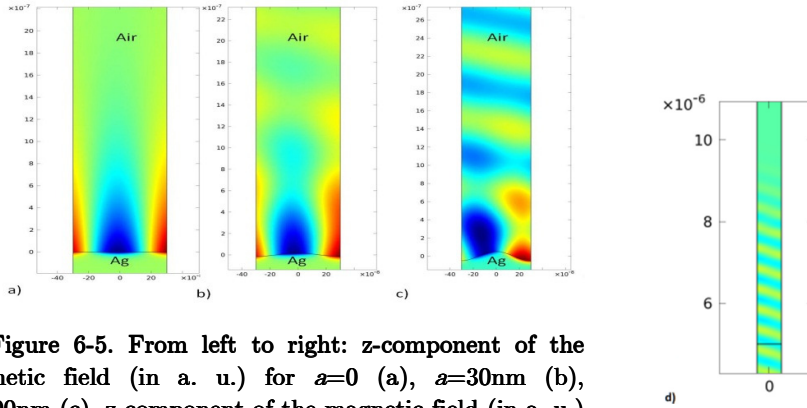

Figure 6-5. From left to right: z-component of the magnetic field (in a. u.) for *a*=0 (a), *a*=30nm (b), *a*=100nm (c), z-component of the magnetic field (in a. u.) inside the cladding region (under the black horizontal line) and the PML domain (above the black horizontal line) (d).

At $\omega \cong 3\text{x}10^{15}\text{Hz}$ a second crossover of the dispersion curves occurs (see Figure 6-3). This point has been subject of several discussions both in metallic and dielectric

113

gratings literature (162), (162), (163), (164), and still is debated [Kolomenskii] about the existence of an energy or momentum gap. An energy gap is expected in presence of grating profiles containing different harmonics (162). Since we assumed a single-harmonic grating profile, therefore, we observe consistently no band gap. Nevertheless it can be noticed a rapid decrease in the imaginary part of k_x in correspondence of this point due to a sudden decrease in the radiative losses. This phenomenology resembles the one found in case of dielectric gratings (163),(164). A detailed discussion of this point is out of the scope of the present work and we remand, for more details, to Ref. (162)-(165).

For a better understanding of the numerical improvement due to the *PML* insertion in Eq. (6.17), we show in Figure 6-6 a comparison between the modal curves calculated with and without the PML addiction (in both cases the maximum κ parameter for accepting the modes was set to 0.1). The absorbing condition avoids the discontinuous behaviour of the modal curves (clearly visible in Figure 6-6). In absence of *PML*, the fictitious periodicity in *y*-direction unavoidably restricts the allowed spectrum of possible frequencies for a given momentum k_x to a discrete set. This discretization still occurs in presence of *PMLs*, but is much more refined, tending to a continuum of states in the limit of infinite *PML* mesh resolution (which mimics perfect open boundary condition).
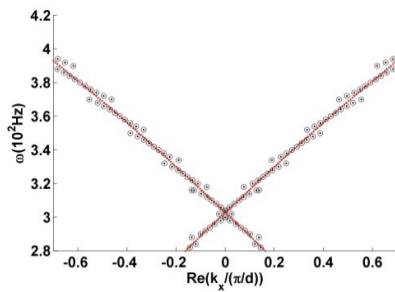

Figure 6-6. Comparison between the modal curves obtained with (red lines) and without (circles black) the PML anisotropy medium.

In order to have an independent check of the reliability of imaginary parts of mode eigenvalues, it has been considered the following *FEM* model Figure 6-7. An *SPP* is

114

launched on a flat metal-air surface at the left boundary of the model. The metal interface then continues with a sinusoidal profile. The impinging *SPP* wave is partially reflected and partially couples to the grating Bloch mode.
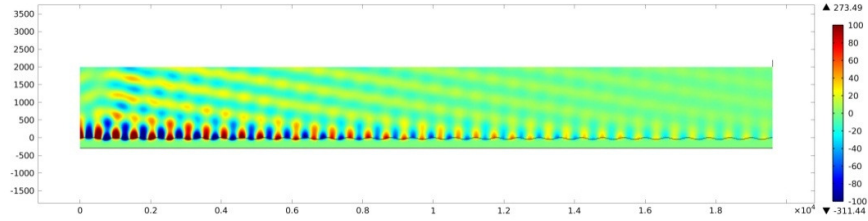

Figure 6-7. z-component of the magnetic field obtained by exciting the proper mode by mean of illumination. The attenuation constant is extracted by fitting the exponential decay of the field intensity. We plot the z-component of the magnetic field for ω=3.5x10^{15}Hz, d=600nm and a=50nm.

Once the SPP Bloch mode is correctly excited, it propagates along the grating with its own complex propagation constant. In particular, from the field profile in Figure 6-7 it's possible to extract the attenuation constant, α, by means of exponential fit and obtain therefore the imaginary part of the propagation constant $Im(\lambda)$ from $\alpha = 1/(2\,Im(\lambda))$ (126). It has been performed the calculation for different frequencies at fixed period $d = 600$nm and amplitude $a = 50$nm. Results are reported in Table 1. We see that there is a perfect match between the direct modal calculation and the indirect method based on *SPP* mode excitation.

ω (10^{15}Hz)	Im(λd/π) illumination	Im(λd/π) modal
3.0	0.0133	0.0133
3.5	0.0237	0.0236
4.0	0.0434	0.0435
4.5	0.1015	0.1004

Table 1. Comparison between the imaginary part of the modes calculated with illumination and modal analysis respectively for four different frequencies at fixed a=50nm.

As a last test for our method it has been considered the radiation pattern of the leaky waves for different frequencies at fixed period $d = 600$nm and amplitude $a =$

115

50nm. According to diffractive structure theory (165), the leaky plasmon mode will radiate via the $n = $ -1 space harmonic. From Ref. (166), (166) the angle of radiation in the limit $\text{Im}(\lambda) \ll \text{Re}(\lambda)$ is well approximated by

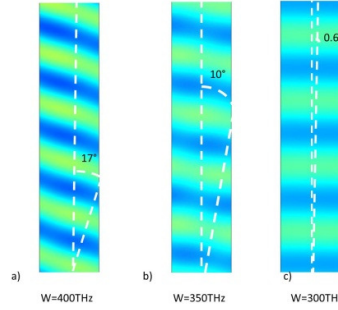$$\lambda_{-1} = k_0 \sin(\vartheta)_{-1} \tag{6.19}$$

Figure 6-8. The leaky radiation direction at three several frequencies (in a.u.)

In Fig.(9) we show the behavior of the angle of emission of the leaky radiation varying the frequency. Again we compare the predicted values by Eq. (6.19) with the simulated results. We averaged the x- and y-components of the electric field in the cladding domain according to Eq. (6.8). In Table 2 we show the comparison between the averaged polarization angle (ϑ_{Avg}) of the electric field and the predicted polarization angle (ϑ) of the leaky radiation according to Eq. (15). We find good match between the theoretic prediction and modal analysis.

ω (10^{15} Hz)	ϑ (Deg) predicted by Eq.(15)	ϑ_{Avg} (Deg) from averaged polarization
3.0	0.63°	0.91°
3.5	10.1°	11.5°
4.0	16.9°	17.8°

Table 2. Comparison between the predicted angle of emission radiation and the retrieved angle by averaged polarization.

5. 2D periodic array

In this section we perform a modal analysis of a bi-periodic plasmonic crystal slab embedded in air, see Figure 6-9. We remark here that the particular geometry chosen is completely arbitrary, since the method can handle any kind of planar periodic array of scatterers.

The test structure we choose consists of an array of squared nano-holes milled in silver metal with sizes $a_x = a_y = a$. Period and thickness are fixed to $d = 940$nm and to $h = 200$nm respectively. Two PMLs are introduced in the unit cell in order to absorb the leakage radiation propagating toward open space. Two *PMLs* are set at distance $z_0 = \pm 1470$nm from the origin (coinciding with the center of the slab) with thickness $L = 4d$, $\bar{\sigma}$ and polynomial exponent n as the previous example.
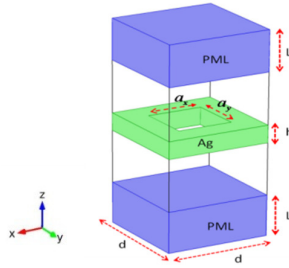
Figure 6-9. Unit cell for the 3D structure: d=600nm, L=4d

Metal films with holes in them exhibit very interesting plasmonic properties of extraordinary optical transmission which have been pointed out in several works (125). What is usually omitted in literature is the detailed visualization of both the real and imaginary dispersions of the SPP modes of the structure. This is due the strong leakage radiation damping that affects the plasmonic modes for large hole sizes, which is hardly handled by standard numerical techniques.

In order to verify the robustness and reliability of the method in presence of both low and high radiative losses, we have performed two simulations, the first for a small

hole size, $a = 250$nm, the second for a wider hole, $a = 500$nm. We focus on the modes along $\hat{\mathbf{x}}$ direction, $\mathbf{k} = \lambda \hat{k}_x$.

In Figure 6-10 we report the transmittance map obtained by *FEM* scattering simulations in case of grating with holes size of 250nm for TE (Figure 6-10a) and TM (Figure 6-10b). Black lines are the real parts of the *SPP* modes calculated with the modal analysis. It is immediately seen that they directly correlate to the transmittance maxima of the structure. This strict connection between horizontal SPP Bloch modes and extraordinary optical transmission was first pointed out by Lalanne and co-workers (170). The location of transmittance resonances approximately follows the dispersions given by the well-known grating coupling relation

$$\omega(k_x)_{m,n} = \frac{1}{n_{eff}}\sqrt{\left(Re(k_x) \pm \frac{2\pi m}{d}\right)^2 + \left(\pm \frac{2\pi n}{d}\right)^2}, \qquad (6.20)$$

where n_{eff} is the real part of effective index of the SPP mode propagationg on a flat silver-air interface (126). The white and red lines in Figure 6-10a,b denote the $(m,n) = (\pm 1,0)$ and the degenerate $(0,\pm 1)$ flat SPP dispersion curves respectively. As can be seen, the $(\pm 1,0)$ dispersion approximately identifies the transmittance resonances in TM polarization (Figure 6-10a) while the $(0,\pm 1)$ identifies resonances in TE (Figure 6-10b). With $\text{Re}(k_y)=0$ the two modes $(0,\pm 1)$ of Eq. (6.1) are degenerate (see the red curve in Figure 6-10). there are four black lines, almost horizontal, between $\omega = 1.9\text{x}10^{15}$ Hz and $2\text{x}10^{15}$Hz. Two of them are quite degenerate and can be approximated by Eq.6.1 with $(m,n)=(0, \pm 1)$. The other two curves are well separated and originate from TE illumination as is seen in Figure 6-10b. Moreover the modal analysis shows the existence of a couple of modes which are not directly associated with transmittance peaks (the narrow curves between $0 < Re(k_y) < 0.05$ and $1.7\text{x}10^{15} < \omega < 1.95\text{x}10^{15}$. These modes are a clear failure of the method in this narrow spectral region for which a more complete justification is reminded in a future work.

In Figure 6-11 we reports the corresponding map for a 500nm hole width. As can be seen, the two bands (which we will identify with blue and red curves, see Figure 6-13 and 6-17 in the following) are no longer close each other and it is evident how the anti-symmetric one (the blue one) is responsible for a much higher transmittance peak than the symmetric one (red one), which instead corresponds to a Fano-like resonance (167). It can be noted that the transmittance maxima of the anti-symmetric band for ω <1.8x10^{15Hz} do not match exactly with the calculated eigen-values. This mismatch is ascribed to the interplay between SPPs at horizontal interfaces and vertical Fabry-Perot resonances (168). We remand at the end of this subsection a last test which takes into account for this mismatch in the special case of normal incidence.

a)

119
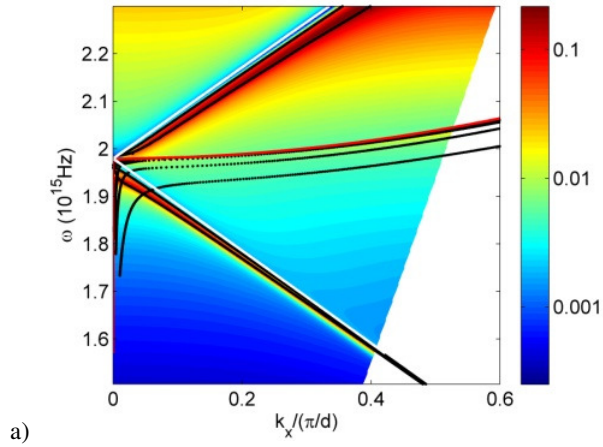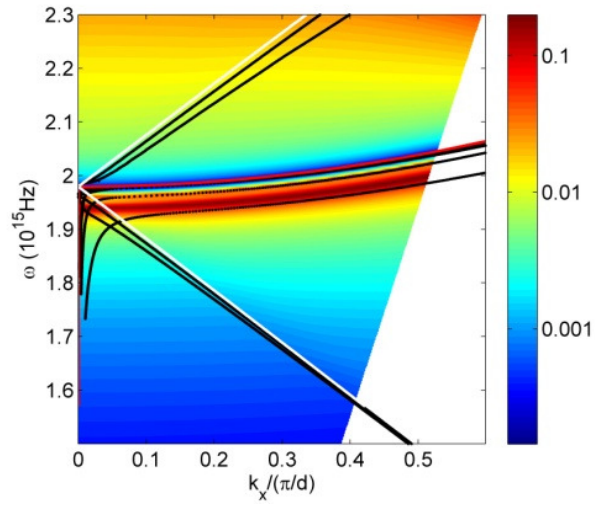
b)

Figure 6-10. Transmittance map for TM (a),TE (b) ,propagation compared with the calculated dispersion curves (black lines) and the grating dispersion curves of modes (1,0) , (white line) and the degenerate mode $(0, \pm 1)$,(red line) for a=250nm .

a)

b)
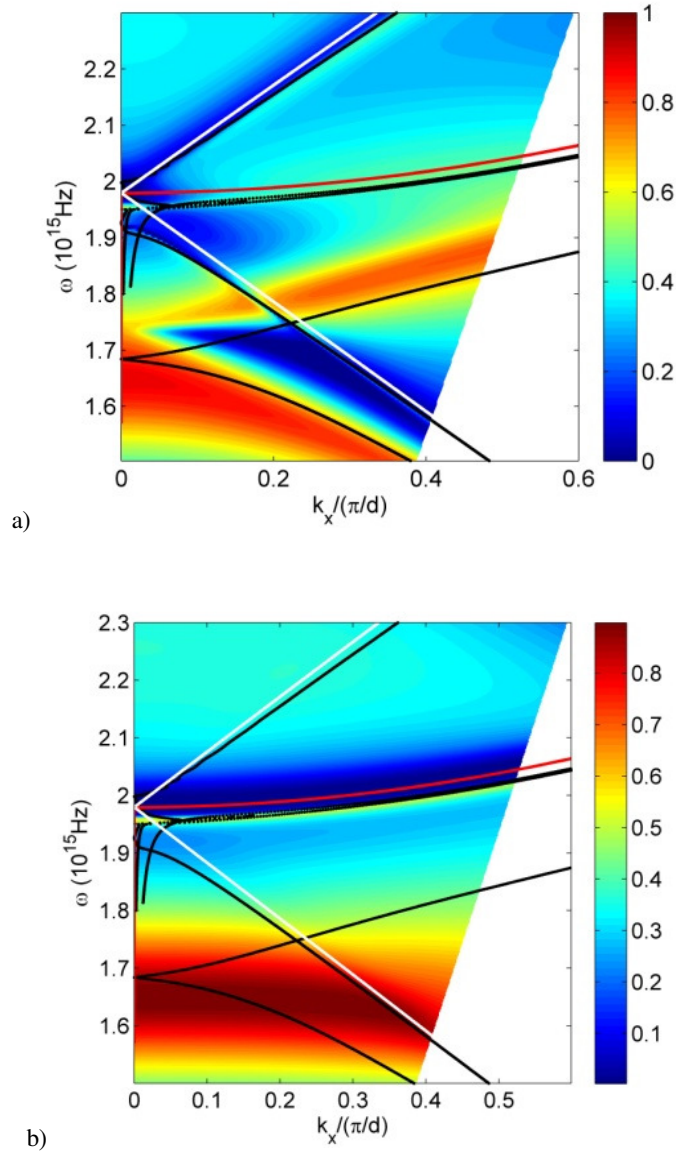
Figure 6-11. Transmittance map for TM (a),TE (b) ,propagation compared with the calculated dispersion curves (black lines) and the grating dispersion curves of modes $(\pm1,0)$, (white line) and the degenerate mode $(0,\pm1)$,(red line) for a=500nm .

In Figure 6-12a and Figure 6-12b we report the y-component of the magnetic field in x-z plane for the two modes observed at frequency of $1.7\text{x}10^{15}$Hz with a=250nm. They turn out to be an anti-symmetric and symmetric mode respectively. Their excitation is a well know phenomenon, extensively discussed in literature (169), and is associated with extraordinary optical transmission (170). Figure 6-12c shows the norm of the

121

magnetic field for the anti-symmetric mode. As expected, for small hole sizes the modes are well confined close to the metal slab. Figure 6-12d and Figure 6-12e show the same field simulation as in Figure 6-12a and Figure 6-12b respectively but with a larger hole size, a=500nm. We see that the mode confinement decreases with a larger hole size and stronger leakage radiation is observed in the cladding regions. Once again we note that the presence of PMLs allows to properly reconstructing the modes field profile even in presence of strong leakage radiation as can be seen in Figure 6-12c,f which show an almost uniform norm of the field in the cladding region.
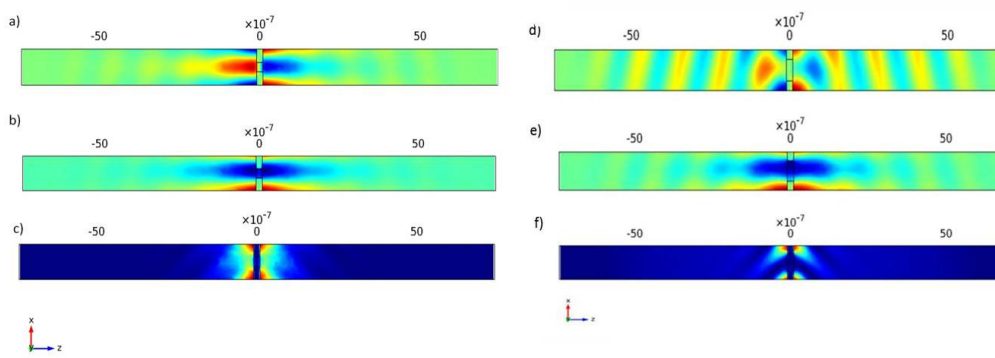
Figure 6-12. y-component of the magnetic field (a. u.) at a=250nm (left side) and a=500 (right side) and frequency of $1.6x10^{15}$Hz. (a, b) anti-symmetric mode, (d, e) symmetric mode, (c, f) norm of the field in (a, d)

Finally we calculate the complete band structure within the first Brillouin along the Γ-X direction for both cases at a=250nm and a=500 nm respectively. The coloured bands in Figure 6-13a refer to the symmetric (red) and anti-symmetric (blue).We see that for both cases the anti-symmetric band is always lower in frequency with respect to the symmetric one. This is a typical feature for the anti-symmetric modes to minimize the energy of the structure (171). In Figure 6-13 we show the real and imaginary parts of the modes for the configuration with a=250nm. Both plots show two small frequency gaps at frequencies close to $1x10^{15}$Hz and $1.9x10^{15}$Hz respectively. The first one takes place at the first edge of the Brillouin zone and can be attributed to a similar mechanism just discussed for the previous example where the metallic peaks and

the air troughs can be associated to the cut metallic wires and to the air holes of the Fishnet structure along the mode direction respectively.
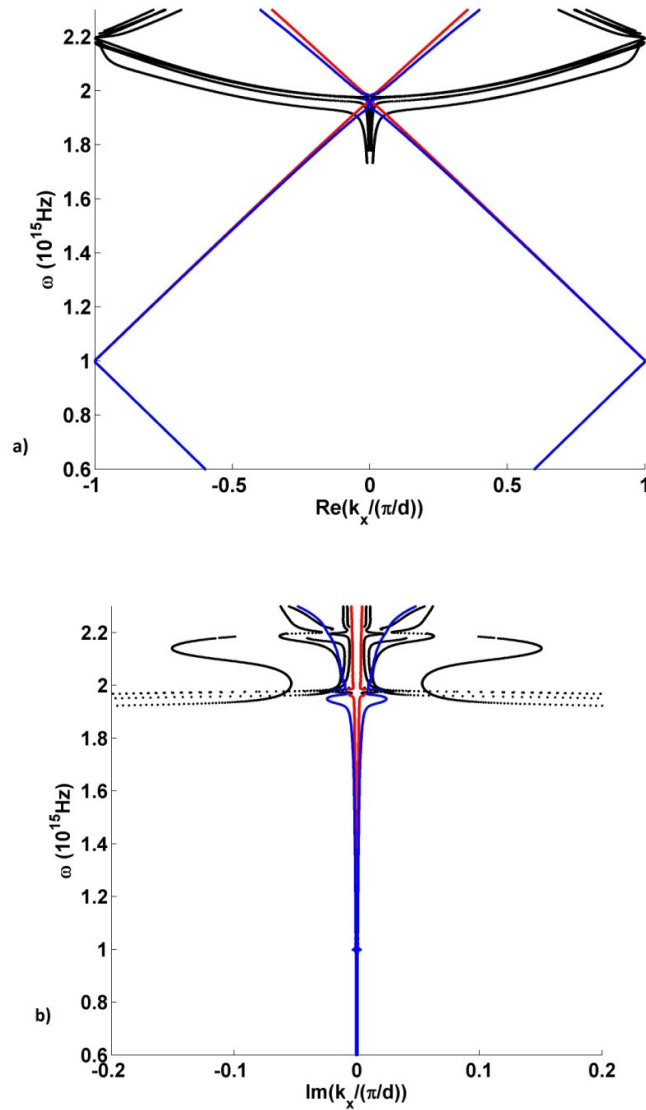
Figure 6-13. Real part a) and imaginary part b) of the modes of the 3D structure at a=250nm. Blue and red points represent the anti-symmetric and symmetric field modes respectively.

In Figure 6-14 we show the real and imaginary part of the modes for a=500nm. It shows the similar features of the case in Figure 6-13 with two larger frequency gaps at frequencies close to 1×10^{15}Hz and 1.9×10^{15}Hz. The energy gap size depends on the hole

size at fixed period and transversal size of the unit cell. The variation of the hole size can modulate the field distribution for the two configuration respect to the centre of the metal cut wires and the centre of the air holes thus increasing the energy gap.
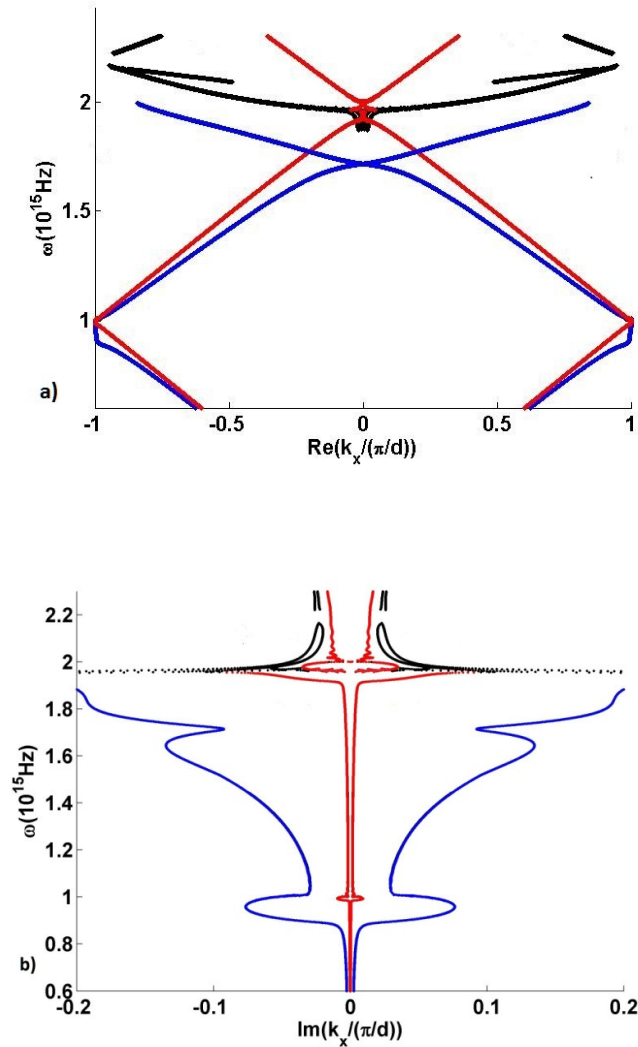
Figure 6-14. Like in figure 13 with a=500nm.

In the last figure (Figure 6-15) we have retrieved (82) the effective permittivity of the metallic slab with a=500nm. As just pointed out by Moreno, Vidal (169) the symmetric and anti-symmetric modes at normal incidence correspond to two resonances: the first one appears close to λ_0=d and is associated with the excitation of

the surface EM mode while the second one emerges at around the cut-off frequency of the fundamental TE mode $\omega_c^{Ag} \simeq 1.68 \times 10^2 Hz$ (see Figure 6-15, blue line) which corresponds Fabry-Pe'rot resonance and is well predicted by our modal analysis (seeFigure 6-11a). Figure 6-15 shows that the cut-off frequency increases when the hole size decreases: the symmetric-anti-symmetric mode separation increases when the hole size increases. This can be also seen if we compare Figure 6-10 with Figure 6-11 for two different size holes.
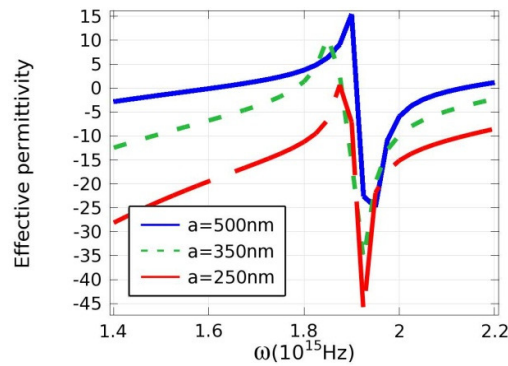
Figure 6-15. Effective permittivity of the hole array .

6.3   Conclusion

In conclusion we have presented a full-vectorial Finite Elements based numerical method for the modal analysis of photonic crystal slabs in presence of dispersive loss materials. The method relies on the reformulation of Helmholtz eigenvalue equation in weak form, including in the unit cell Perfectly Matched Layers in order to simulate open boundaries. The formulation yields a quadratic eigenvalue equation system that may be straightforwardly implemented in commercial, generic Finite-Element packages. This latter fact in particular enables easy complex calculation of arbitrarily complex geometries of photonic crystal slabs, in particular the important class of plasmonic

nanostructures. Moreover, an important advantage associated with solving the quadratic eigenvalue problems in $\boldsymbol{k}$, is that it naturally allows retrieving both real and imaginary part of Bloch wave vectors, which is of particular interest in analysis of plasmonic nanostructures. On the other hand, PML implementation allows to properly handling leaky modes, characteristic feature of photonic crystal slabs, enabling the reconstruction of the correct radiative eigen-mode profile. Results obtained with modal analysis were corroborated by means of comparison with scattering simulations, and good agreement was found between the methods.

7 Complex dispersion curves for Fishnet metamaterials

The modal method presented in the last section has been implemented in order to calculate the dispersion curves for a bulk (full periodic) metamaterial Fishnet. The geometric features are the same reported in Figure 4-1. An infinite number of functional layer are considered in the z-direction (full periodicity) relative to a real bulk metamaterial. Also the permittivity of metal and dielectric separator are the same reported in section 4.1.

7.1 Negative Index Plasmonic Fishnet

The negative index mode reported in section (4.1) propagates in the z-direction. Therefore, the method is applied to the specific case of $\mathbf{k}_0 = 0$ and $\mathbf{k}_n = \hat{\mathbf{z}}$. The resulting dispersion curves are plotted in Figure 7-7-1 for the 600nm$<\lambda<$1000nm wavelength range.
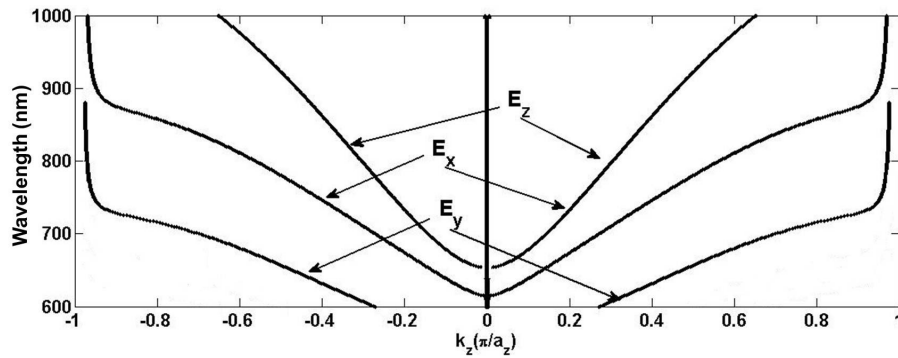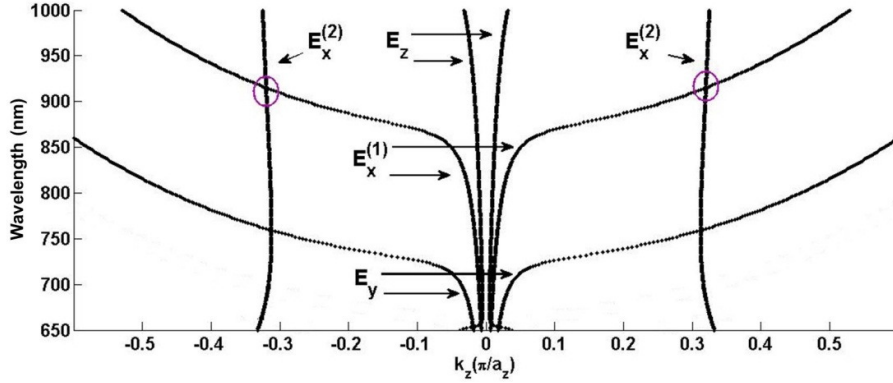
Figure 7-7-1: Real (Top) and imaginary (Bottom) parts of $k_z(\omega)$ for several eigen-modes of the Fishnet metamaterial shown in Figure 4-1. In addition to the transverse mode electrically polarized in the $\hat{x}$ direction labelled $\mathbf{E_x}$ which was identified in Figure 4-5, we see two other transverse modes electrically polarized in the $\hat{y}$ direction labeled $\mathbf{E_y}$, and a longitudinal mode electrically polarized in the $\hat{z}$ direction labeled $\mathbf{E_z}$.

Four eigen-modes that have the smallest values of $\text{Im}(k_z)$ and therefore the longest propagation lengths. The negative index mode found in Figure 4-5 is labeled E_x to indicate that it is transversely polarized with the electric field pointing in the x-direction (see Figure 7-7-2a,b). Moreover Figure 7-7-2b shows the characteristic anti-symmetric electric configuration as shown in Figure 3-8a and discussed in Section (3). It can be seen that it is a negative index mode because (according to the convention where fields are Bloch periodic with the exponential factor $\exp[i(\omega t - \mathbf{k} \cdot \mathbf{x})]$) a negative index mode should have a wavenumber whose real and imaginary parts have the same sign. In Figure 7-7-1, that describes the E_x mode for wavelength from 600nm to 1000nm. In addition, two other negative index modes are observed. Of these two modes, the one labeled E_y is transversely polarized with the electric field pointing in the y-direction and the mode labeled E_z is longitudinally polarized with the electric field pointing in the z-direction (shown in Figure 7-7-2c).

a)

b)

c)
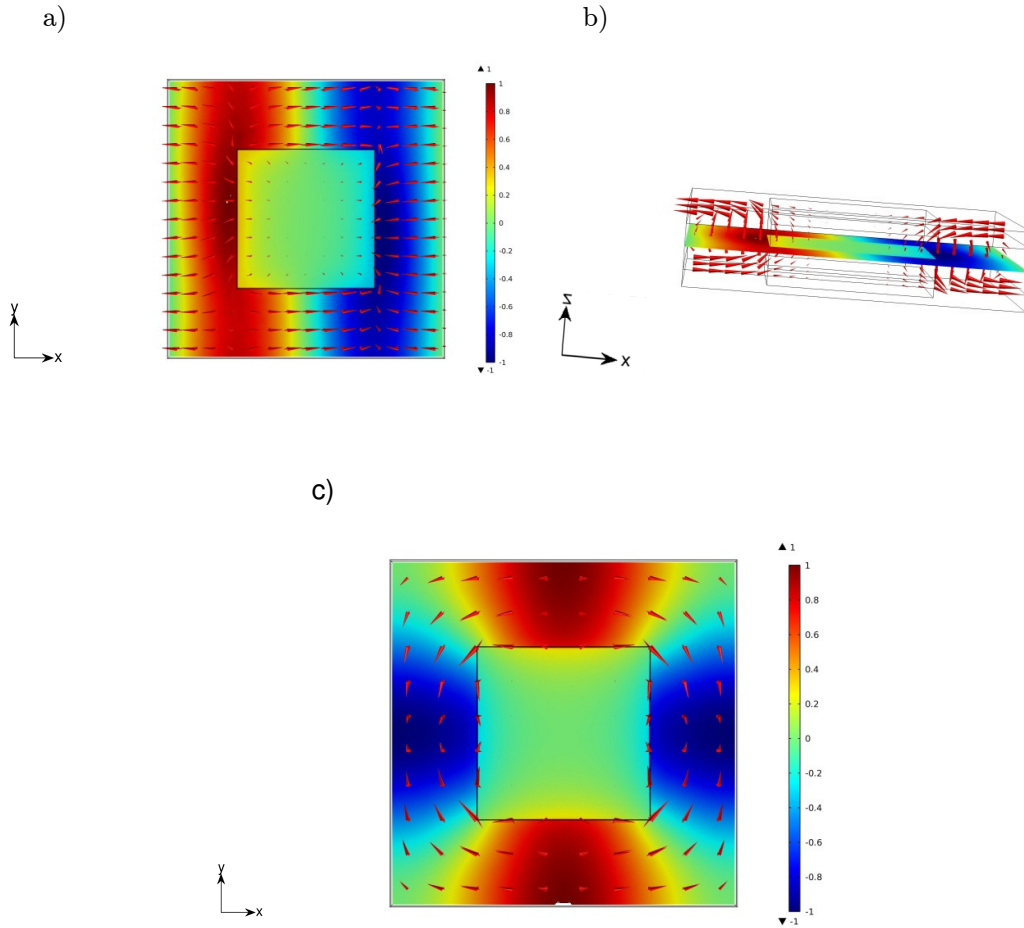
Figure 7-7-2. Field profiles for the transverse E_x mode (a) ,(b) and the longitudinal E_z mode (c) on a cross-section laying on the x-y plane in the middle of the MgF2 layer. Arrows represent the electric field and color represents the E_z field. For all field profiles the wavelength is 855 nm

From Figure 7-7-1b it is also clear the reason for which a discontinuity exist around 900 nm as shown in Figure 4-5 for the case of 5-functional layered structure. In fact a second order mode labelled $E_x^{(2)}$ is responsible for the discontinuity having a longer propagation constant than $E_x^{(1)}$ up to 900nm and thus dominating on the spectral transmission. A similar result in a different spectral region and geometric configuration has just been proved (122) with a *RCW* approach deriving from a transmission and reflection calculation, while the *FEM* modal method gives it directly and with lower computational cost.

129

The figure of merit (*FOM*) is often defined (section (3)) as the ratio between the real and imaginary parts of the index of refraction. For eigen-modes of the Fishnet crystal with real ω and a complex **k** pointing in the z-direction this is equivalent to the ratio between the real and imaginary parts of k_z or $\text{FOM} \equiv \text{Re}(k_z)/\text{Im}(k_z)$. Without knowledge of the complex wavenumber of an eigen-mode of a metamaterial, the figure of merit must be calculated indirectly. For example, in Re. (115) the *FOM* is estimated numerically from simulated transmission through a Fishnet sample. With knowledge of the complex wavenumbers of the crystal eigen-modes, it is possible to calculate the FOM directly. The *FOM* for each of the three eigen-modes identified in Figure 7-7-1 is plotted in Figure 7-7-3. A positive *FOM* corresponds to the real and imaginary parts of k_z having the same sign, therefore indicating a negative index Eigen-mode. We see again that all three modes are in fact negative index modes in a fairly broad 600nm$<\lambda$ <1000nm range.
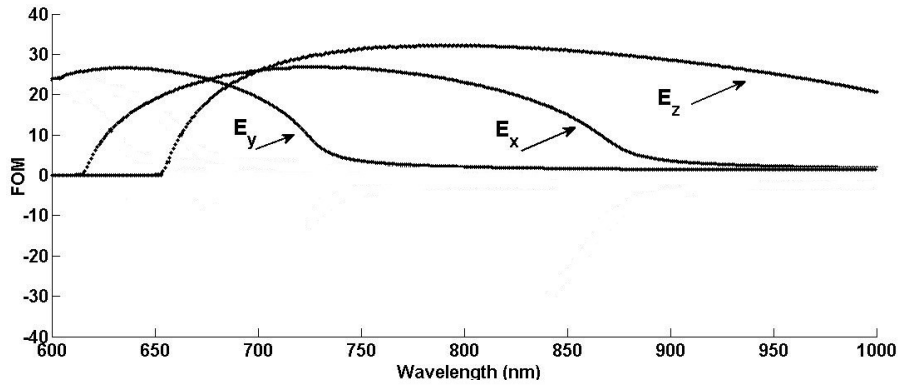
Figure 7-7-3 The FOM for the three Fishnet eigen-modes identified in Figure 7-7-1

Moreover another application of this modal method is the calculation of isofrequency $\omega(\text{k}) = const$ contours in metamaterial crystals. The conventional approach is also highly laborious for plasmonic Fishnets because of the strong frequency dependence of the dielectric permittivities of metals. Other semi-analytic techniques used for analyzing wave propagation in highly symmetric PEC-based Fishnets (172) do not apply to

plasmonic Fishnets of interest. Moreover the *FEM* method provides information about propagation lengths which are important in lossy metamaterials such as the Fishnet. Figure 7-7-4 shows an iso-frequency diagram calculated using the FEM modal method. A single isofrequency contour was obtain by fixing the real frequency ω, setting $\mathbf{k}_0 = k_y \hat{\mathbf{y}}$ and $\mathbf{k}_n = \hat{\mathbf{z}}$, and then scanning k_y from $-\pi /p_y$ to π /p_y.

a)   b)
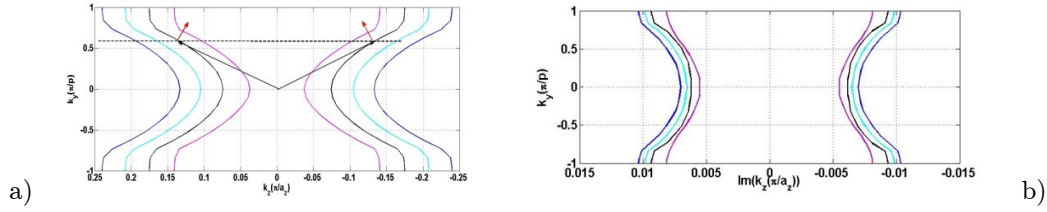
Figure 7-7-4. (a)Iso-frequency contours for the E_x polarized eigen-mode of the Fishnet crystal plotted with respect to Re(k_z) and k_y. The black arrows indicate the direction of the phase velocity and the red arrows indicate the direction of the group velocity at a wavelength of 820nm and k_y =w/$c$sin(π/6).(b) Iso-frequency contours for the imaginary part of k_y. The E_x eigen-modes are represented with colors: (magenta) 620nm, (black) 630 nm, (cyan) 640 nm, (blue) 650nm.

The eigenvalue in this simulation is a complex valued k_z. This procedure was repeated for several values of wavelength from 620nm to 650nm. The resulting eigen-modes can be excited by a plane wave incident on an interface between vacuum and the Fishnet crystal parallel with the x-y plane if the wave-vector of the incident wave is confined to the y-z plane. Because the y-component of the incident wave-vector is real valued, the y-component of the wave excited in the Fishnet crystal must also be real-valued.

$k_y = \sin\theta (\omega /c)$ where θ is the incidence angle with respect to the normal z. The eigenmode excited in the Fishnet crystal decays in the z-direction as indicated by the imaginary part of k_z plotted in Figure 7-7-4b. The iso-frequency contours in Figure 7-7-4 are hyperbolic in appearance. For $k_y =(\omega /c)\sin(\pi /6)$ and a wavelength of 630nm the iso-frequency diagram shows two eigen-modes with the correct value of k_y and equal and opposite values of k_z. The correct mode is found by calculating the group velocity $v_g \equiv \partial\omega / \partial\text{Re}(\mathbf{k})$ which is by definition normal to the iso-frequency

131

contours. In the absence of anomalous dispersion the group velocity indicates the direction of energy flow in the crystal . Choosing the correct solution requires us to choose the solution that has energy flowing in the positive z-direction (i.e. away from the interface). This selects the solution with a negative $\mathrm{Re}(k_z)$. This is a negative index mode in the sense that in the z-direction the phase velocity and group velocity have opposite signs.

7.2   Negative refraction test

In order to prove the physical negative refraction of a *NIM* we performed a direct test by simulating the refraction of a plane wave normally incident against a wedge endowed with negative effective refraction index. The same parameters used for the multi-layered Fishnet in Chapter 4 has been choosen.
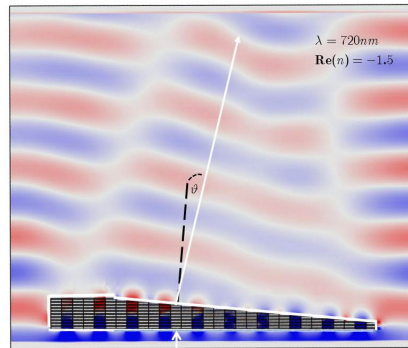
Figure 7-5. Negative (right) refraction from a wedge of aperture $\alpha = 5.5°$ .The   dashed black line represents the normal to the wedge while the white solid line represents the wave path for a normal incident wave refracting at negative angle from the wedge. The colour represent the electric field polarized in *x*-direction.

The wedge consist of 21 layers (at its maximum height) scaled down to 5 layers (at its minimum height). The wedge aperture is $\alpha = 5.5°$. The effective refraction index for a N=10 functional layers structure at 720nm was first calculated , where the valued retrieved for the refractive index is *Re(n)*= -1.5, see Figure 7-6. Note that the 5-functional layers structure in Figure 4-5 overwrites well to the 10-functional layers structure refractive index showed in Figure 7-6 proving that just for few layers (at least 7 layers) the asymptotic bulk value is well reached. The predicted angle of refraction is calculated by Snell's law, $n = \sin(\vartheta) / \sin(\alpha)$. For *Re(n)*=-1.5 it is $-\vartheta \approx 8°$ which describes the simulated out-going wave direction at negative angle. Moreover from the extraction of the scattered electric field polarization (retrieved with COMSOL) the field components (*x*- and *z*- components respectively) have been averaged in order to find the average polarization which gives us a value of 9.2° comparable with the previous calculated of 8°. The little mismatch can be due to the finiteness of the prism size and to edge diffractions.
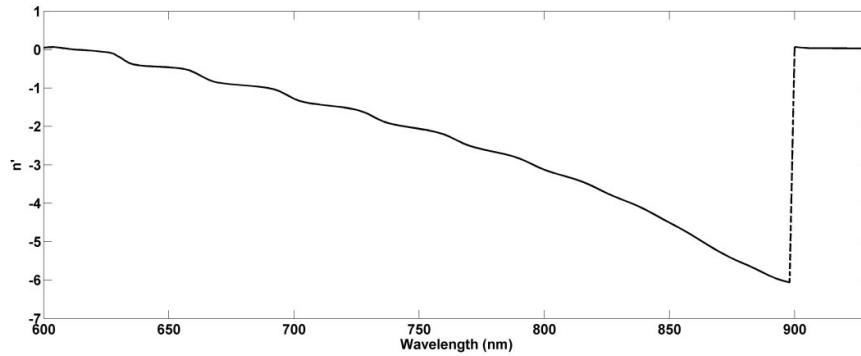
Figure 7-6. Retrieved effective refractive index for a *N*=10 functional layer structure.

7.3   Conclusion

The application of the FEM modal method to the Fishnet metamaterial clearly show that the bulk-structure is strongly dispersive.   Three negative-index modes of the Fishnet structure and hyperbolic iso-frequency surfaces have been computed for the least-damped transverse mode. The method represent a powerful tool because it directly allows the extraction of the imaginary part of the refractive index and consequently its FOM and the possibility to distinguish between the dominant modes inside the metamaterial.

8   Conclusion

The aim of this doctoral thesis has been to study the propagation of electromagnetic waves in periodic structures, namely in *Fishnet* metamaterial. These new class of materials possesses uncommon properties in nature and one could say that metamaterials have formed a new research direction in recent years. It has been investigated on the origin and the manipulation of the negative refractive index both in a double-layered structure and a bulk multi-layered system. The refractive index of a metamaterial fishnet in the long wavelength regime is an effective parameter of the system. However, the current homogeneous methods for the extraction of the effective fishnet parameters are not sufficient to understand all the complex properties of the structure. The main contribute of the thesis is a clear presentation of a powerful modal method in the Finite Element environment. This method allows the comprehension of the Fishnet modes from a microscopically point of view. It enables the possibility to calculate all the complex Bloch modes (real and imaginary part) and the complex isofrequency contours, being both a crucial point when dissipation is present in metamaterials.   This method amply discussed in (148) has been extended to embrace a wide class of plamonic and photonic crystal slabs.   The introductory part of the thesis gives a brief historical overview of metamaterial research. The main research directions in this area are outlined, together with a list of crucial papers published in each subject field in recent years. In Chapter 2 we reported the general tools for the extraction of the effective parameters for isotropic and bianistropic metamaterials at normal incidence and at large wavelength regime ($\lambda \gg d$). The choice of multi-branch in the real part of the effective refractive index requires much attention and some artifacts can be produced around the resonance wavelength (resonant − anti-resonant behavior between permittivity and permeability) due to the intrinsic periodicity of the structure. In Chapter 3 the Fishnet structure is built by crossed metallic wires separated by a dielectric spacer. The connection of the wires forms a slab pair. The slab behaves as a

resonant magnetic-moment element generated by opposed currents between the double interface metal-dielectric forming a magnetic dipole loop. While negative permittivity is easily obtained by using the most common metals, achieving negative permeability is requires more efforts. The presence of wide slabs in the Fishnet structure allows a large filling factor (F) and thus a strong magnetic response. Moreover the connection with continuous wires pushes the lower resonant electric mode of the structure much above the magnetic resonance regime, leading to a perfect overlapping between negative permeability and negative permittivity at the magnetic resonance. For this reason the Fishnet structure seems to be a prominent candidate for achieving *LH* metamaterials. We have reported a design and a parametrical analysis of a Fishnet in the optical spectral range. In particular the dependence of both the magnetic and the electric resonance on the geometric features of the Fishnet is investigated. We found that a sharp electric resonance is down-shifted by 200 nm related to weakening of the magnetic resonance. For appropriately designed squared hole-array structures, the frequency of the magnetic resonance coincides with a region of negative effective permittivity and a negative index of refraction is seen in the simulations. We use the *LC* circuit description proposed for comparing the simulated results with the analytic predictions and to reduce the time needed to design practical applications using the proposed line. Hence we have a clear understanding of the parametric space over which it is possible to optimize the Fishnet *NIM* and the related applications. In Chapter 4 we studied how the effective optical parameters change as the number of layers increases. The number of layers required to reach the bulk 3D regime strongly depends on the coupling between adjacent layers, and hence on the interlayer spacing. If the distance between adjacent functional layers is small, the coupling is strong, the convergence of the optical properties is slow, and at least four functional layers are required. The behavior converges, but not to that of the monolayer case. In contrast, for larger distances, the coupling is weak and the retrieved optical parameters for several functional layers are very similar to that of the monolayer case (173). The retrieved effective parameters remain the same when increasing the number of layers, which means that the bulk metamaterial limit has been reached. The minimum number of

layers required for the metamaterial to qualify as 'bulk' depends on both the structure under investigation and the choice of a_z. Moreover we employed a modal analysis in order to make evidence of the evanescent internal and external *SPPs* modes of the multi-layered structure based on the approximation between the multi-layered Fishnet metamaterial and the multi-layered flat system (equaling the external momentum of the incident light to the $\mathbf{k}(\omega)$ dispersion curve of a multi-layered flat system). We made evidence of SPPs modes for N= 1-,2-,3-,4- functional layers system noticing that the 1-layer resonances split into N in the multilayer configuration. In Chapter 5 we showed how the Focused-ion beam lithography can be used to prepare prototypes of simple and effective metamaterial structures well known as "fish-net". The prepared samples were characterized by means of spectroscopic ellipsometry in terms of transmittance and reflectance measurements. Numerical simulation of the structure (the transmittance (T) and reflectance (R)) are in good qualitative agreement with optical measurements in a wide range of wavelengths although a shift in the position of the peak was observed. A wavelength band of single-negative operation is expected where the sample exhibits NIM behavior in the infrared at 1200 nm. It has been showed how bi-anisotropy can sensibly affect the sample. The analytic method presented in Chapter 2 has been employed for the extraction of the bianisotropic effective parameters in order to study their behavior for a 1- and 3- functional layered system. We showed that the magnitude of negative refractive index in *NIMs* depends on the sidewall-angle, that is, the minimum value of $Re(n_{eff})$ increases as the *SWA* increases as result of the blue-shifted resonance peaks of both $Re(\mu_{eff})$ and $Re(\varepsilon_{eff})$. In Chapter 6 we have presented a full-vectorial Finite Elements based numerical method for the modal analysis of 2D and 3D palsmonic/photnonic crystal in presence of dispersive losses materials. The introduction of *PMLs* in the weak formulation of the Helmholtz eigenvalue equation allows the calculation of the complex Bloch dispersion curves also for plasmonic/photonic crystal slab. The method directly solves a quadratic eigenvalue problem in $\mathbf{k}$ and it naturally allows retrieving both real and imaginary part

of Bloch wave vectors, which is of particular interest in analysis of plasmonic nanostructures.

Moreover the modal method allows the study of leaky modes radiation thus enabling not only the calculation of the real and imaginary part of the leaky modes but also the reconstruction of the correct radiative eigen-mode profile. Another powerful application of the modal method consists in the calculation of the iso-frequency (complex) contour for any periodic structure, in particular a metamaterial Fishnet (Chapter 7). Several indirect tests based on the direct illumination and scattering formulation have been performed confirming the reliability of the method which at our knowledge is one of the most advanced in terms of computational time, precision and richness of physical information.

9   Bibliography

1. *"The electrodynamics of substances with simultaneously negative values of ε and μ".* V. G. Veselago. 4, s.l. : Soviet Physics Uspekhi, 1968, Vol. 10, pp. 509–514.

2. *"Unusual waveguide characteristics associated with the apparent negative permeability obtainable in ferrites.* GHB, Thompson. s.l. : Nature, 1995, Vol. 175, pp. 1135–1136.

3. J. D. Joannopoulos, S. G. Johnson, R. D. Meade, and J. N. Winn. *Photonic Crystals:Molding the Flow of Light.* Second edition. s.l. : Princeton Univ. Press, 2008.

4. *"Metamaterials in electromagnetics (invited review),".* A. Sihvola. 1, s.l. : Metamaterials, 2007, Vol. 1, pp. 2-11.

5. *"On the three different denotations of handedness in wavematerial interaction".* A. Sihvola and I. Lindell. Pisa : URSI International Symposium on Electromagnetic Theory, 2004, pp. 84-86.

6. *Electromagnetic waves in chiral and bi-isotropic media.* I. V. Lindell, A. Sihvola, S. A. Tretyakov, and A. J. Viitanen. Boston & London : Artech House, 1994.

7. *"On group-velocity".* Lamb, H. 1, s.l. : Proc. London Math. Soc.,, 1994, pp. 473–479.

8. A. Schuster. *"An Introduction to the Theory of Optics".* London : Edward Arnold, 1904. pp. 607–608.

9. *"Growth of a wave-group when the group velocity is negative".* Pocklington, H. C. s.l. : Nature, 2005, Vol. 71, pp. 607–608.

10. *Lectures on some problems of the theory of oscillations.* L. I. Mandelshtam. Moscow : Complete Collection of Works, 1944, Vol. 5.

11. *"The energy of electromagnetic waves in dispersive media".* Sivukhin, D. V. s.l. : Opticheskaia Spektroskopia, 1957, Vol. 3, pp. 308-312.

12. *"Magnetism from conductors and enhanced nonlinear phenomena".* J. B. Pendry, A. J. Holden, D. J. Robbins, and R. J. Stewart. 11, s.l. : IEEE Trans. Microwave Theory Tech, 1999, Vol. 47, pp. 2075–2084.

13. *"Composite medium with simultaneously negative permeability and permittivity".* D. R. Smith, W. J. Padilla, D. C. Vier, S. C. Nemat-Nasser, and S. Schultz,. 18, s.l. : Phys. Rev. Lett, May 2000, Vol. 84, pp. 4184–4187.

14. *"Negative refraction makes a perfect lens".* Pendry, J. B. 18, s.l. : Phys. Rev. Lett, October 2000, Vol. 85, pp. 3966–3969.

15. *"Negative refractive index in left-handed materials".* Kroll, D. R. Smith and N. 14, s.l. : Phys. Rev.Lett., Oct. 2000, Vol. 84, pp. 2933–2936.

16. *"Direct calculation of permeability and permittivity for a left-handed material".* D. R. Smith, D. C. Vier, N. Kroll, and S. Schultz. 14, s.l. : Appl. Phys. Lett, Oct. 2000, Vol. 77, pp. 2246–2248.

17. *"Experimental verification of a negative index of refraction".* R. A. Shelby, D. R. Smith, and S. Schultz,. s.l. : Science, April 2001, Vol. 292, pp. 7–79.

18. *"Analogues of an ionized medium: Applications to the ionosphere".* Bracewell, R. N. s.l. : Wireless Eng.,, December 1954, Vol. 31, pp. 320-326,.

19. *"Plasma simulation by artificial dielectrics and parallel-plate media,".* W. Rotman. 1, 1962 : IRE Trans. Antennas Propag., January, Vols. vol. AP-10, pp. 82-85.

20. *"Extremely low frequency plasmons in metallic mesostructures,".* J. B. Pendry, A. J. Holden, W. J. Stewart, and I. Youngs. 25, s.l. : Phys. Rev. Lett, June 1996, Vol. 76, pp. 4773-4776.

21. *"3D wire mesh photonic crystal".* D. F. Sievenpiper, M. E. Sickmiller, and E. Yablonovitch. 14, s.l. : Phys. Rev. Lett., April 1996, Vol. 76, pp. 2480-2483,.

22. *"Magnetism from conductors and enhanced nonlinear phenomena,".* J. B. Pendry, A. J. Holden, D. J. Robbins, and W. J. Stewart. 11, s.l. : IEEE Trans. Microwave Theory Tech., November 1999, Vol. 47, pp. 2075-2084,.

23. *"Metal lens antennas,".* Kock, W. E. s.l. : Proceedings, IRE and Waves and Electrons, November 1946, pp. 828-836.

24. *"Calculation and measurement of bianisotropy in a split ring resonator metamaterial,".* D. R. Smith, J. Gollub, J. J. Mock, W. J. Padilla, and D. Schurig. s.l. : J. Appl. Phys., 2006, Vol. 100, pp. 024 507(1–9).

25. *"Electrically small isotropic three dimensional magnetic resonators for metamaterial design,".* J. D. Baena, L. Jelˌınek, R. Marquˌes, and J. Zehentner. s.l. : Appl. Phys. Lett., 2006, Vol. 88, pp. 134 108(1–3).

26. *"Refining the perfect lens,".* Ramakrishna, J. B. Pendry and S. A. s.l. : Physica B, 2003, Vol. 338, pp. 329–332.

27. *"Limitations on sub-diffraction imaging with a negative refractive index slab,".* D. R. Smith, D. Schurig, M. Rosenbluth, S. Schultz, S. A. Ramakrishna, and J. B. Pendry. s.l. : Appl. Phys.Lett., 2003, Vol. 82, pp. 1506–1508.

28. *"Spherical perfect lens: Solutions of Maxwells equations for spherical geometry,".* Pendry, S. A. Ramakrishna and J. B. s.l. : Phys. Rev. B, 2004, Vol. 69, pp. 115 115(1–7).

29. *"Overcoming the diffraction limit with a planar lefthanded transmission-line lens,".* Eleftheriades, A. Grbic and G. V. 11, s.l. : Phys. Rev. Lett., March 2004, Vol. 92, pp. 117 403(1–4).

30. *"Near-perfect imaging in a focusing system based on a left-handed-material plate,".* Kissel, A. N. Lagarkov and V. N. 7, s.l. : Phys. Rev. Lett., Feb. 2004, Vol. 92, pp. 077 401(1–4).

31. *"Focusing by planoconcave lens using negative refraction,".* P. Vodo, P. V. Parimi, W. T. Lu, and S. Sridhar. s.l. : Appl. Phys. Lett., 2005, Vol. 86, pp. 201 108(1–3).

32. *"Subwavelength resolution with a negative-index metamaterial siperlens".* K. Aydin, I. Bulu, and E. Ozbay. s.l. : Appl. Phys. Lett., 2007, Vol. 90, pp. 254 102(1–3).

33. *"Negative index lens aberrations,".* Smith, D. Schurig and D. R. s.l. : Phys. Rev. E, 2004, Vol. 70, pp. 065 601(1–4).

34. *"Three-dimensional superresolution in metamaterial slab lenses: Experiment and theory,".* F. Mesa, M. J. Freire, R. Marquˌes, and J. D. Baena. s.l. : Phys. Rev. B, 2005, Vol. 72.

35. *"Theory of three-dimensional subdiffraction imaging,"*. R. Marqujes, M. J. Freire, and J. D. Baena. s.l. : Appl. Phys. Lett., 2006, Vol. 89, pp. 211 113(1–3).

36. *"Perturbation on the perfect lens: the near-perfect lens,"*. O. E. French, K. I. Hopcraft, and E. Jakeman. s.l. : New Journal of Phys., 2006, Vol. 8, p. 271.

37. *"Terahertz magnetic response from artificial materials,"*. T. J. Yen, W. J. Padilla, N. Fang, D. C. Vier, D. R. Smith, J. B. Pendry, D. N. Basov,and X. Zhang. s.l. : Science, 2004, Vol. 303, pp. 1494–1496.

38. *"Magnetic response of metamaterials at 100 terahertz,"*. S. Linden, C. Enkrich, M. Wegener, J. Zhou, T. Koschny, and C. M. Soukoulis. s.l. : Science, 2004, Vol. 306, pp. 1351–1353.

39. *"Regenerating evanescent waves from a silver superlsne"*. N. Fang, Z. Liu, T.-J. Yen, and X. Zhang,. 7, s.l. : Optics Express, April 2003, Vol. 11, pp. 682–687.

40. *"Subwavelength imaging at infrared frequencies using an array of metallic nanorods,"*. M. G. Silveirinha, P. A. Belov, and C. R. Simovski,. s.l. : Phys. Rev. B, 2007, Vol. 75, pp. 035 108(1–12).

41. *"Subdiffraction-limited optical imaging with a silver superlens,"*. N. Fang, H. Lee, C. Sun, and X. Zhang. s.l. : Science, 2005, Vol. 308, pp. 534–537.

42. *"Controlling electromagnetic fields,"*. J. B. Pendry, D. Schurig, and D. R. Smith. s.l. : Science, 2006, Vol. 312, pp. 1780–1782.

43. *"Calculation of material properties and ray tracing in transformation media,"*. D. Schurig, J. B. Pendry, and D. R. Smith. [ed.] 9794–9804. 21, s.l. : Optics Express, Oct. 2006, Vol. 14.

44. *"Notes on conformal invisibility devices,"*. Leonhardt, U. 118, s.l. : New Journal of Phys.,, 2006, Vol. 8.

45. *"Metamaterial electromagnetic cloak at microwave frequencies,"*. D. Schurig, J. J. Mock, B. J. Justice, S. A. Cummer, J. B. Pendry, A. F. Starr, and D. R.Smith. s.l. : Science, 2006, Vol. 314.

46. *"Role of bianisotropy in negative permeability and left-handed metamaterials,"*. R. Marqujes, F. Medina, and R. Rafii-El-Idrissi. s.l. : Phys. Rev. B, 2005, Vol. 65, pp. 144 440(1–6),.

47. *"A chiral route to negative refraction,"*. Pendry, J. B. s.l. : Science, November 2004, Vol. 306, pp. pp. 1353–1355.

48. *"Generalized constitutive relations for metamaterials based on the quasi-static lorentz theory,"*. A. Ishimaru, S.-W. Lee, Y. Kuga, and V. Jandhyala. 10, s.l. : IEEE Trans. Antennas Propagat., October 2003, Vol. 51.

49. *"Plane waves with negative phase velocity in isotropic chiral mediums,"*. Mackay, T. G. 2, s.l. : Microwave and Opt. Techn. Lett., April 2005, Vol. 45, pp. 120–121.

50. *"Backward-wave regime and negative refraction in chiral composites,"*. S. A. Tretyakov, A. Sihvola, and L. Jylhϒa. s.l. : Photonics and Nanostructures, 2005, Vol. 3, pp. 107–115.

51. *"Negative refractions in uniaxially anisotropic chiral media,"*. Cui, Q. Cheng and T. J. s.l. : Phys. Rev. B, 2006, Vol. 73, pp. 113 104(1–4).

141

52. *"Negative refraction in gyrotropic media,"*. V. M. Agranovich, Y. N. Gartstein, and A. A. Zakhidov. s.l. : Phys. Rev. B, 2006, Vol. 73, pp. 045 114(1–12).

53. *"Tunable split-ring resonators for nonlinear negative-index metamaterials,"*. I. V. Shadrivov, S. K. Morrison, and Y. S. Kivshar. 20, s.l. : Optics Express, 2006, Vol. 14, pp. 9344–9349.

54. *"Tunable metamaterial transmission lines based on varactor-loaded split-ring resonators,"*. I. Gil, J. Bonache, J. Garcɪ̣a-Garcɪ̣a, and F. Martɪ̣n. 6, s.l. : IEEE Trans. Microwave Theory Tech., 2006, Vol. 55, pp. 2665–2674.

55. A. A. Zharov, I. V. Shadrivov, and Y. S. Kivshar,. s.l. : Phys. Rev. Lett., 2003, Vol. 91.

56. *"Electronically controlled phase shifters based on right/left-handed transmission lines,"*. O. G. Vendik, I. B. Vendik, D. V. Kholodnyak, S. P. Zubko, and E. V. Serebryakova. Paris, France : Proc. of the 35th European Microwave Conference, October 2005, pp. 909–912.

57. *"Design and measurement of a smart tunable periodic material,"*. L. Mercier, M. Thɪ̣evenot, A. Crunteanu, B. Jecko, J. C. Orlienyes, C. Champeaux,A. Caterinot, and P. Blondy,. Long beach, California : IEEE MTT-S International Microwave Symposium Digest, 2005.

58. *"Liquid-crystal photonic-band-gap materials: The tunable electromagnetic vacuum,"*. John, K. Busch and S. s.l. : Phys. Rev. Lett., 1999, Vol. 83, pp. 967–970.

59. *"Tunable refraction effects in two-dimensional photonic crystals utilizing liquid crystals,"*. Yoshino, H. Takeda and K. s.l. : Phys. Rev. E, 2003, Vol. 76, pp. 056 607(1–5).

60. *"Tunable Fishnet metamaterials infiltrated by liquid crystal,"*. Alexander Minovich, Dragomir N. Neshev, David A. Powell, Ilya V. Shadrivov. s.l. : Appl. Physic Tett., 2010, Vol. 96.

61. *"Optical negative-index metamaterials,"*. Shalaev, V. M. s.l. : Nature Photonics, 2007, Vol. 1, pp. 41–48.

62. *"Terahertz magnetic response from artificial materials,"*. T. J. Yen, W. J. Padilla, N. Fang, D. C. Vier, D. R. Smith, J. B. Pendry, D. N. Basov,and X. Zhang. s.l. : Science, 2004, Vol. 303, pp. 1494–1496.

63. *"Magnetic response of metamaterials at 100 terahertz,"*. S. Linden, C. Enkrich, M. Wegener, J. Zhou, T. Koschny, and C. M. Soukoulis. s.l. : Science, 2004, Vol. 306, pp. 1351–1353.

64. *"Midinfrared resonant magnetic nanostructures exhibiting a negative permeability,"*. S. Zhang, W. Fan, N. C. Panoiu, K. J. Malloy, R. M. Osgood, and S. R. J. Brueck. s.l. : Phys.Rev. Lett., 2005, Vol. 94, pp. 037 402(1–4).

65. *"Negative index of refraction in optical metamaterials,"*. V. M. Shalaev, W. Cai, U. K. Chettiar, H.-K. Yuan, A. K. Sarychev, V. P. Drachev, and A. V. Kildishev. s.l. : Optics Lett., 2005, Vol. 30, pp. 3356–3358.

66. *"Cut-twire pairs and plate pairs as magnetic atoms for optical metamaterials."*. Dolling, G., Enkrich, C., Wegener, M., Zhou, J. F. & Soukoulis, C. M. s.l. : Opt. Lett., 2005, pp. 3198–3200.

67. *"Simultaneous negative phase and group velocity of light in a metamaterial."*. Dolling, G., Enrich, C., Wegener, M., Soukoulis, C. M. & Linden, S. s.l. : Science, 2006, Vol. 312, pp. 892–894.

68. *"Negative-index metamaterial at 780 nm wavelength,"*. Dolling, G., Wegener, M., Soukoulis, C. M. & Linden, S. s.l. : Opt. Lett., 2007, Vol. 32, pp. 53–55.

69. *"Dual-band negative index metamaterial: Double negative at 813 nm and single negative at 772 nm,"*. Chettiar, U. K. et al. s.l. : Opt. Lett., 2007, Vol. 32, pp. 1671–1673.

70. *"A. Double-negative polarization-independent Fishnet metamaterial in the visible spectrum,"*. Garcia-Meca, C., Ortuno, R., Rodriguez-Fortuno, F. J., Marti, J. & Martinez. s.l. : Opt. Lett., 2009, Vol. 34, pp. 1603–1605.

71. *"Yellow-light negative-index metamaterials,"*. Xiao, S. M., Chettiar, U. K., Kildishev, A. V., Drachev, V. P. & Shalaev, V. M. s.l. : Opt. Lett., 2009, Vol. 34, pp. 3478–3480 .

72. *"Low-loss multilayered metamaterial exhibiting a negative index of visible of refraction at visible wavelengths,"*. Garcia-Meca, C. et al. s.l. : Phys. Rev. Lett., 2011, Vol. 067402.

73. *"Past achievements and future challenges in the development of three-dimensional photonic metamaterials,"*. Costas M. Soukoulis, and Martin Wegener. s.l. : Nature, July 17, 2011, Vol. 154.

74. *"Resonant and antiresonant frequency dependence of the effective parameters of metamaterials,"*. T. Koschny, P. Markos,*D. R. Smith,and C. M. Soukoulis. s.l. : Physical Review E, 2003, Vol. 68.

75. *1992.* D, Bergman D J and Stroud. 147, s.l. : Solid State Phys, Vol. 46.

76. D, Stroud. 3368, s.l. : Phys. Rev., 1975, Vol. 12.

77. O, Hunderi. 3419, s.l. : Phys. Rev. B, 1973, Vol. 7.

78. W, Milton G. *The Theory of Composites.* s.l. : Cambridge University Press, 2002.

79. *"Determination of effective permittivity and permeability of metamaterials,"*. D. R. Smith and S. Schultz, P. Markos and C. M. Soukoulis. 195104, s.l. : Phys. Rev. B, April 19, 2002, Vol. 65.

80. *"Impact of inherent periodic structure on effective medium,"*. ThP. Markoš, E. N. Economou, D. R. Smith, D. C. Vier,and C. M. Soukoulis. 245105, s.l. : Phys. Rev. B, 2005, Vol. 71.

81. *"Robust method to retrieve the constitutive effective parameters of metamaterials,"*. Xudong Chen, Tomasz M. Grzegorczyk, Bae-Ian Wu, Joe Pacheco, Jr., and Jin Au Kong. 016608, s.l. : Phys. Rev. B, 2004, Vol. 70.

82. *"Electromagnetic parameter retrieval from inhomogeneous metamaterials,"*. D. R. Smith, D. C. Vier,Th. Koschnyand C. M. Soukoulis. 036617, s.l. : Phys. Rev. E, 2005, Vol. 71.

83. *Negative Refractive Index in Optics of Metal-Dielectric composites.* A. V. Kildishev, W. Cai, U. K. Chettiar, H.-K. Yuan, A. K. Sarychev*, V. P. Drachev, and V. M. Shalaev. s.l. : J. Opt. Soc. Am. B, 2006, Vol. 23, pp. 423-433.

84. *"Bianisotropic Photonic Metamaterials,"*. Christine ɟ Eliane Kriegler, Michael Stefan Rill, Stefan Linden, and Martin Wegener. 2, s.l. : IEEE JOURNAL OF SELECTED TOPICS IN QUANTUM ELECTRONICS,, April 2010, Vol. 16.

85. *"Determination of the effective constitutive parameters of bianisotropic metamaterials,"*. Zhaofeng Li, Koray Aydin, and Ekmel Ozbay. 026610, s.l. : Phys. Rev. E, 2009, Vol. 79.

86. @, COMSOL Multiphysics. www.comsol.com. [Online] 4.2.

87. Jin, J. *The Finite Element Method in Electromagnetics.* second edition. s.l. : John Wiley & Sons, Inc., New York, 2002.

88. Zimmerman, W. B. J. *Process Modelling and Simulation with Finite Element Methods.* s.l. : World Scientific, Singapore, 2004.

89. Ferrari, P. P. Silvester and R. L. *"Finite elements for electrical engineers,".* 3rd edition. s.l. : Cambridge University Press, Cambridge, 1996.

90. Kong, J. A. *Electromagnetic Wave Theory.* s.l. : EMW, Cambridge,MA, 2008.

91. *"A negative permeability material at red light,".* Hsiao-Kuan Yuan, Uday K. Chettiar, Wenshan Cai, Alexander V. Kildishev,Alexandra Boltasseva*, Vladimir P. Drachev, and Vladimir M. Shalaev. 3, s.l. : Optics Express, 2007, Vol. 15, pp. 1076-1083.

92. Wenshan Cai, Uday K. Chettiar, Hsiao-Kuan Yuan, Vashista C. de Silva,Alexander V. Kildishev, Vladimir P. Drachev, and Vladimir M. Shalaev. 6, s.l. : OPTICS EXPRESS, 2007, Vol. 15.

93. *Effective Medium Theory of Left-Handed Materials.* Kafesaki, T. Koschny and M. 10, s.l. : Phys. Rev. Lett., 2004, Vol. 93, pp. 107402(1-4).

94. *"Design-related losses of double-Fishnet,".* G. Dolling, M.Wegener, C. M. Soukoulis, and S. Linden. 18, s.l. : Optic express, 2008, Vol. 15, p. 155102.

95. *A PERIODIC POROUSNANOSTRUCTURED LEFT-HANDED MATERIAL SLAB AT OPTICALFREQENCIES.* Wu, P.-Y. Chen and S.-C. 1, s.l. : microwave and optical technology letters, 2008, Vol. 50.

96. *Optical Constants of Noble Metals.* Christy, P.B. Johnson and R.W. 12, s.l. : Phys. Rev. B, 1972, Vol. 6.

97. *Metallic photonic crystals at optical wavelengths.* I. El-Kady, M. M. Sigalas, R. Biswas, K. M. Ho, and C. M. Soukoulis. 23, s.l. : Phys. Rev. B, 2000, Vol. 62, pp. 299-302.

98. A. Christ, T. Zentgraf, S. G. Tikhodeev, N. A. Gippius, O. J. F. Martin, J. Kuhl, and H. Giessen. s.l. : Phys. Status Solidi B, 2006, Vol. 243, p. 2344.

99. *Localized surface-plasmon resonances and negative refractive index in nanostructured electromagnetic metamaterials.* J. Parsons, E. Hendry, J. R. Sambles, and W. L. Barnes. s.l. : Phys. Rev. B, Vol. 80, pp. 245117-.

100. *"Left-handed metamaterials: The Fishnet structure and its variation.".* M. Kafesaki, I. Tsiapa, N. Katsarakis,Th. Koschny,C. M. Soukoulis,and E. N. Economou. 23, s.l. : Phys. Rev. B, 2007, Vol. 75, pp. 235114-(1-9).

101. M. Soukoulis, M. Kafesaki, and E. N. Economou,. 1941, s.l. : Adv. Mater., 2006, Vol. 18.

102. *"Parametric investigation and analysis of Fishnet metamaterials in the microwave regime,".* N.-H. Shen, G. Kenanakis, M. Kafesaki, N. Katsarakis, E. N. Economou,and C. M. Soukoulis. 12, s.l. : Opt. Soc. of Am. B, 2009, Vol. 26, pp. 61-67.

103. *"Magnetic response of nanoscale left-handed metamaterials,".* R. S. Penciu, M. Kafesaki, Th. Koschny, E. N. Economou,and C. M. Soukoulis. 23, s.l. : Phys. Rev. B, 2010, Vol. 81, pp. 235111-(1-11) .

104. *Unifying approach to left-handed material design.* Jiangfeng Zhou, Eleftherios N. Economon,Thomas Koschny and Costas M. Soukoulis. 24, s.l. : Opt. Lett., 2006, Vol. 31, pp. 3620-3622.

105. *"Numerical simulations of terahertz double-negative metamaterial with isotropic-like Fishnet structure,".* P. Ding, E.J. Liang, W.Q. Hu, L. Zhang, Q. Zhou Q.Z. Xue. 2, s.l. : Photonics and Nanostructures- Fundamental and application, 2009, Vol. 7, pp. 92-100.

106. *"Saturation of the Magnetic Response of Split-Ring Resonators at Optical Frequencies,".* 22, s.l. : Phys. Rev. Lett., 2005, Vol. 95, pp. 223902-(1-4).

107. Bruce W. Wessels. s.l. : Annu. Rev. Mater, 2007, Vol. 37, pp. 659-679.

108. M. Maaza, O. Nemraoui, C. Sella,A.C. Beye and B. Baruch-Barak. 1, s.l. : Optics Communications, 2005, Vol. 254, pp. 188-195.

109. *"Magnetic activity at infrared frequencies in structured metallic photonic crystals,".* R. A. Shelby, D. R. Smith, and S. Schultz. s.l. : J. Phys. Condens. Matter, 2002, Vol. 14, pp. 6383-6394.

110. *"Numerical investigation of negative refractive index metamaterials at infrared and optical frequencies,".* Osgood, N.-C. Panoiu and R. M. s.l. : Opt. Commun., 2003, pp. 331-337.

111. *"Magnetic response of split-ring resonators in the far infrared frequency regime,".* N. Katsarakis, G. Konstantinidis, A. Kostopoulos, R. S. Penciu, T. F. Gundogdu, Th Koschny, M. Kafesaki,E. N. Economou and C. M. Soukoulis. s.l. : Opt. Lett., 2005, Vol. 30, pp. 1348-1350.

112. *"Demonstration of Near-Infrared Negative-Index Metamaterials,".* S. Zhang, W. Fan, N. C. Panoiu, K. J. Malloy. s.l. : Phys. Rev. Lett., 2005, Vol. 95.

113. *"Effective parameters of resonant negative refractive index metamaterials: Interpretation and validity,".* D. Seetharamdoo, R. Sauleau, K. Mahdjoubi and A. Tarot. s.l. : J. Appl. Phys., 2005, Vol. 98, p. 063505.

114. *"Three-dimensional photonic metamaterials at optical frequencies,".* NA LIU, HONGCANG GUO, LIWEI FU, STEFAN KAISER, HEINZ SCHWEIZER AND HARALD GIESSEN. s.l. : Nature, 2008, Vol. 7.

115. *"Three-dimensional optical metamaterial with a negative refractive index,".* Jason Valentine, Shuang Zhang, Thomas Zentgra, Erick Ulin-Avila, Dentcho A. Genov, Guy Bartal and Xiang Zhang. s.l. : Nature, 2008, Vol. 455.

116. *"Transition from thin-film to bulk properties of metamaterials,".* Carsten Rockstuhl, † Thomas Paul, and Falk Lederer, Thomas Pertsch,Thomas Zentgraf,* Todd P. Meyrath, and Harald Giessen. 3, s.l. : Phys. Rev. B, 2008, Vol. 77, pp. 035126-(1-9).

117. *"Plasmonic Building Blocks for Magnetic Molecules in Three-Dimensional Optical Metamaterials,".* Na Liu, Liwei Fu, Stefan Kaiser, Heinz Schweizer, and Harald Giessen. 20, s.l. : Adv. Mater., Vol. 2008, pp. 3859–3865.

118. H. Liu, D. A. Genov, D. M. Wu, Y. M. Liu, Z. W. Liu, C. Sun, S. N.Zhu, X. Zhang. 76, s.l. : Phys. Rev., 2007, Vol. B, p. 073101.

119. N. Liu, H. C. Guo, L. W. Fu, S. Kaiser, H. Schweizer, H. Giessen, Nat. s.l. : Nat.Mater., 2007, Vol. 19, p. 3628.

120. P. Atkins, J. D. Paula. Physical Chemistry. 8th edition. Oxford : Oxford University Press, 2006.

121. P. Nordlander, C. Oubre, E. Prodan, K. Li, M. I. Stockman. s.l. : Nano Lett., 2004, Vol. 4, p. 899.

122. *"Optical negative-index bulk metamaterials consisting of 2D perforated metal-dielectric stacks,".* Shuang Zhang, Wenjun Fan, N. C. Panoiu,K. J. Malloy,R. M. Osgood,and S. R. J. Brueck. 15, s.l. : Opt. Expr., Vol. 14, p. 6779.

123. Ritchie, 1R. H. 874, s.l. : Phys. Rev., 1957, Vol. 106.

124. T. W. Ebbesen, H. J. Lezec, H. F. Ghaemi, T. Thio, and P. A.Wolf. 667, s.l. : Nature, 1998, Vol. 391.

125. *Light passing through subwavelength apertures.* F. J. Garcia-Vidal, L. Martin-Moreno,T. W. Ebbesen,L. Kuipers. s.l. : Rev. Of Mod. Phys., 2010, Vol. 82.

126. Raether, H. *Surface Plasmons on Smooth and Rough Surfaces and on gratings.* s.l. : Springer Tracts in Modern Physics, 1988. Vol. 111.

127. *"Surface Plasmon in thin films,".* Economu, E.N. 2, s.l. : Phys. Rev. , 1969, Vol. 182.

128. *"Role of surface plasmon polaritons on optical transmission through double layer metallic hole arrays,".* R. Ortuño, C. García-Meca, F. J. Rodríguez-Fortuño, J. Martí, and Alejandro Martínez. 7, s.l. : Phys. Rev. B, Vol. 79, pp. 075425-(1-10).

129. L. Martín-Moreno, F. J. García-Vidal, H. J. Lezec, K. M. Pellerin,T. Thio, J. B. Pendry, and T. W. Ebbesen. s.l. : Phys. Rev. Lett., 2011, Vol. 86, p. 1114.

130. *"Double-negative polarization-independent Fishnet metamaterial in the visible spectrum,".* C. García-Meca, * R. Ortuño, F. J. Rodríguez-Fortuño, J. Martí, and A. Martínez. 10, s.l. : Opt. Lett., 2009, Vol. 34.

131. 14. C. Enrich, 1M. Wegener,S. Linden,2S. Burger,L. Zschiedrich,F. Schmidt,J. F. Zhou,Th.Koschny, and C. M. Soukoulis,. s.l. : Phys. Rev. Lett., 2005, Vol. 95, p. 203901.

132. Uday K. Chettiar, Alexander V. Kildishev, Hsiao-Kuan Yuan, Wenshan Cai, Shumin Xiao,Vladimir P. Drachev, and Vladimir M. Shalaev. 12, s.l. : Optic letters, 2007, Vol. 32.

133. . S. Zhang, W. Fan, N. C. Panoiu, K. J. Malloy, R. M. Osgood, and S. R. J. Brueck. s.l. : Phys. Rev. Lett., 2005, Vol. 95, p. 137404 .

134. *"Comparison of negative refractive index materials with circular, elliptical and rectangular holes,".* Brueck, Z. Ku and S. R. J. s.l. : Opt. Express, 2007, Vol. 15, pp. 4515-4522.

135. *"Realization of three-functional-layer negative-index photonic metamaterial,".* G. Doling, M. Wegener and S. Linden. s.l. : Opt. Lett., 2007, Vol. 32, pp. 551-553.

136. *"Optical metamaterials at near and mid-IR range fabricated by nanoimprint lithography,".* W. Wu, E. Kim, E. Ponizovskaya, Y. Liu, Z. Yu , N. Fang, Y. R. Shen, A. M. Bratkovsky, W. Tong, C. Sun,X. Zhang , S. Y. Wang and R. S. Williams. s.l. : Appl. Phys.A, 2007, Vol. 87, pp. 143-150.

137. *"An efficient way to reduce losses of left-handed metamaterials,".* J. Zhou, T. Koschny and C. M. Soukoulis. s.l. : Opt. Express., 2008, Vol. 16, pp. 11147-11152.

138. *"Bi-anisotropy of multiple-layer Fishnet negative index metamaterials due to angled sidewalls,".* Zahyun Ku, Jingyu Zhang, and S. R. J. Brueck. 8, s.l. : Opt. Express., 2009, Vol. 17.

139. *"Plasmonics for improved photovoltaics,".* Polman, 3. H. A. Atwater and A. s.l. : Nat. Mater., 2010, Vol. 9, pp. 205-213.

140. *"Nano-optics of surface plasmon polaritons,".* 4. A. V. Zayats, I. I. Smolyanov, A. A. Maradudin. s.l. : Phys. Rep., 2005, Vol. 408.

141. Sakoda, 11. K. *Optical Properties of Photonic Crystal.* s.l. : (New York: Springer, 2001), 2001.

142. *"Algorithms for the nonlinear eigenvalue problem,".* Ruhe, 12. A. s.l. : SIAM J. Numer. Anal. , 1973, Vol. 10, pp. 674-689.

143. *"Tunneling in photonic band structures," .* Yu, 13. T. Suzuki and P. L. s.l. : J. Opt. Soc. Am. B, 1995, Vol. 12, p. 804.

144. *"Behavior of light at photonic crystal interfaces,".* E. Istrate, A. A. Green, and E. H. Sargent. s.l. : Phys. Rev. B, 2005, Vol. 71, p. 195122.

145. *"Revised plane wave expansion method for dispersive material and its application to band structure calculation of photonic crystal slabs,".* S. Shi, C. Chen and D. Prather. s.l. : Appl. Phys. Lett., 2005, Vol. 86, p. 043104.

146. *"Aplication of finite element methods to photonic crystal modelling,".* B. P. Hiett, B. D. H., S. J. Cox, J. M. Generowicz, M. Molinari, and K. S. Thomas. s.l. : IEE Proc - Sci. Meas. Technol, 2002, Vol. 149, pp. 293-296.

147. *"The complex bloch bands of a 2D plasmonic crystal displaying isotropic negative refraction,".* M. Davanco, Y. Urzhumov, and G. Shvets. s.l. : Opt. Express, 2007, Vol. 15, pp. 9681–9691.

148. *"Complex k band diagrams of 3D metamaterials/photonic crystals,".* C. Fietz, Y. Urzhumov, and G. Shvets. 20, s.l. : Opt. Express,, 2011, Vol. 19, pp. 19027-19041.

149. Stakgold, I. *Boundary Value Problem of Mathematical Physics,".* s.l. : New York: Macmillan, 1968. Vol. 2.

150. *"The quadratic eigenvalue problem,".* Meerbergen, F. Tisseur and K. s.l. : SIAM Review, 2001, Vol. 43, pp. 235–286.

151. *"Biosensing with plasmonic nanosensors,".* J. N. Anker, W. P. Hall, O. Lyandres, N. C. Shah, J Zhao and R. P. Van Duyne. s.l. : Nat. Mater., 2008, Vol. 7, pp. 442-453.

152. *"Plasmonics for improved photovoltaics,".* Polman, H. A. Atwater and A. s.l. : Nat. Mater., 2010, Vol. 9, pp. 205-213.

153. M. L. Brongersma, P. G. Kik. *Surface Plasmon Nanophotonics.* s.l. : Springer, 2007.

154. *"Holey metal films: From extraordinary transmission to negative-index behavior,".* A. Mary, Sergio G. Rodrigo, L. Martin-Moreno, and F. J. Garcia-Vidal. [ed.] 80. s.l. : Phys. Rev. B, 2009, p. 165431.

155. K. Sakoda. *Optical Properties of Photonic Crystals.* Berlin : Springer-Verlag, 2001.

156. *"Electric and magnetic properties of sub-wavelength plasmonic crystals,".* Urxhumov, Gennady Shvets and Yaroslav A. s.l. : J.Opt. A: Pure Appl. Opt., 2005, Vol. 7, pp. S23-S311.

157. *"A perfectly matched anisotropic absorber for use as an abosrbing boundary condition,".* Sacks, Z. S., Kingsland, D. M., Lee, R. and Lee, Jin-Fa. 12, s.l. : IEEE Transactions on Antennas and Propagation, 1995, Vol. 43, pp. 1460-1463.

158. *"An Anisotropic Perfectly Matched Layer-Absorbing Medium for the Truncation of FDTD Lattices,".* Stephen D., Gedney. 12, s.l. : Transactions on Antennas and Propagation, 1996, Vol. 44, pp. 1630-1639.

159. Palik, Edward D. *"Handbook of optical constants of solids,".* s.l. : Academic Press.

160. *Accurate determination of quality factor of axisymmetric resonators byperfectly mathed layer.* Kirk, M.Imran and Andrew G. s.l. : arXiv:1101.1984v2, 2011.

161. *"Physical origin of photonic energy gaps in the propagation of surface plasmons on gratings,".* W.L.Barnes, T.W. Preist, S.C. Kitson, and J.R. Sambles. 9, s.l. : Physical Review B, 1996, Vol. 54.

162. *"Corrugated dielectric Waveguides: A numerical Study of the Second-Order Stop bands,".* M.Neviere, P.Vincent and. s.l. : Appl. Phys., 1979, Vol. 20, pp. 345-351.

163. *"Optical properties of deep lamellar grating: a coupled Bloch-mode insight,".* P. Lalanne, J.P.Hugonin and P. Chavel. 6, s.l. : Journal of Lightwave technology, 2006, Vol. 24, pp. 2442-2449.

164. *"Band gaps and leaky-wave effect in resonant photonic-crystal waveguide,"*. Magnusson, Y.Ding and R. 2, s.l. : Opt. Express, Vol. 15, pp. 608-694.

165. *"Beaming of light at broadside through a subwavelength hole: Leaky wave model and open stopband effect,"*. D.R. Jackson, A.A. Oliner T. Zhao and J.T. Williams. 40, s.l. : RADIO SCIENCE, 2005, Vol. 12.

166. *"The role of leaky plasmon waves in the directive beaming of light through a subwavelength aperture,"*. D. R. Jackson, 1J. Chen, R. Qiang, F. Capolino, and A. A. Oliner. 26, s.l. : Optics Express, 2008, Vol. 16, pp. 21271-21281.

167. *"Extraordinary Transmission of metal films with array of subwavelength holes,"*. James V. Coe, Joseph M. Heer, Shannon Teeters-KKennedy, Hong Tian and Kenneth R. Rodriguez. s.l. : Annu. Rev. Phys. Chem, 2008, Vol. 59, pp. 179-202.

168. *"Mimicking Surface Plasmons with Structured Surfaces,"*. J. B. Pendry1, L. Martín-Moreno and F. J. Garcia-Vidal. 5685, s.l. : Science, 2004, Vol. 305, pp. 847-848.

169. *"Theory of extraordinary optical transmission through subwavelength hole arrays,"*. L. Martin-Moreno, F.J. Garcia, H.J. Lezec and T.W. Ebbesen. s.l. : Physical review letters, 2001, Vol. 6, pp. 114-117.

170. *"Microscopic theory of the extraordinary optical transmission,"*. Haitao Liu, Philippe Lalanne. s.l. : Nature, 2008, Vol. 452, pp. 728-731.

171. Stefan A. Maier, *"Plasmonics. Foundamentals and applications.* s.l. : Springer New York.

172. *"Fishnet metamaterials - rules for refraction and limits of homogenization,"*. L. Jelinek, R. Marques, and J. Machac. s.l. : Opt. Express, 2010, Vol. 18, pp. 17940–17949.

173. *"Negative refractive index response of weakly and strongly coupled optical metamaterials,"*. Jiangfeng Zhou, Thomas Koschny, Maria Kafesaki, and Costas M. Soukoulis. s.l. : Phys. Rev. B, 2009, Vol. 80, p. 035109.